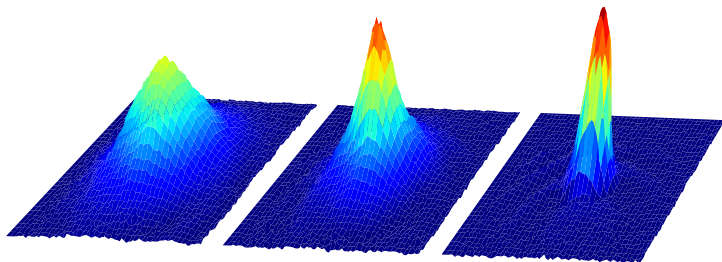


# A Single Apparatus for the Production of Ultracold Fermionic Lithium and Cold Bosonic Caesium Gases

by Asaf Paris-Mandoki



Thesis submitted to The University of Nottingham  
for the degree of Doctor of Philosophy, May 2015



## Abstract

Ultracold mixture experiments hold the promise of providing new insights into many-body quantum systems as well ultracold chemistry and few-body phenomena. The work presented in this thesis dealt with the construction of a new apparatus for the production and study of ultracold gases of fermionic lithium-6 and bosonic caesium-133. These isotopes offer a wide tunability in their interaction strength, both in inter-species and intra-species collisions, through magnetic Feshbach resonances. Additionally, the widely different resonance frequencies of lithium and caesium enables independent control of each of the species.

With this apparatus, Bose-Einstein condensates (BEC) containing  $10^4$  lithium Feshbach molecules are routinely produced. The cooling system for caesium has been developed in parallel and important steps towards producing ultracold caesium gases have been made. An optical dipole trap has been loaded with  $2 \times 10^6$  caesium atoms and evaporative cooling towards quantum degeneracy can now be pursued.

Laser, vacuum, magnetic and control systems have been developed for the implementation of this experiment. Light produced with this laser system was used to laser cool atoms, create conservative dipole traps as well as to provide means of imaging atomic clouds. Additionally, a system to produce strong magnetic fields of up to 1400 G has been established in order to exploit the wide tunability in the atomic interactions. Software that was developed for the computerised control system facilitated the coordination of all the components involved in the experimental sequence. Measurements and calculations that showcase the functionality of relevant parts of the setup are presented in this thesis.

In this experiment, lithium and caesium atoms are obtained from a novel type of Zeeman slower [1] and are loaded into a magneto-optical trap (MOT). The system is capable of doing this independently for each of the atomic species as well as sequentially. After the MOT has been loaded with atoms, they are transferred into a conservative far-of-resonance optical dipole trap. By adjusting the interactions between atoms and lowering the depth of the dipole trap, efficient evaporative cooling of lithium was carried out from which a molecular BEC was obtained. Time-of-flight measurements were used to characterise the condensate and study its expansion dynamics.

# Contents

<b>1</b>	<b>Introduction</b>	<b>3</b>
<b>2</b>	<b>Theoretical Background</b>	<b>7</b>
2.1	Atomic Structure . . . . .	7
2.2	Interaction with Static Magnetic Fields . . . . .	10
2.3	Interaction of Atoms with Light . . . . .	15
2.4	Scattering Theory . . . . .	18
2.5	Feshbach Resonances . . . . .	20
<b>3</b>	<b>Atom Cooling, Trapping and Imaging</b>	<b>25</b>
3.1	Zeeman Slower . . . . .	25
3.2	Magneto-Optical Trap . . . . .	26
3.2.1	Laser Cooling Limits . . . . .	28
3.3	Dipole Trap . . . . .	30
3.4	Evaporative Cooling . . . . .	31
3.5	Imaging . . . . .	33
3.5.1	Measuring the Temperature . . . . .	35
<b>4</b>	<b>Experimental Apparatus</b>	<b>39</b>
4.1	Laser System . . . . .	39
4.1.1	Frequency Stabilisation . . . . .	40
4.1.2	Lithium Laser Setup . . . . .	45
4.1.3	Caesium Laser Setup . . . . .	47
4.1.4	Dipole Trap Lasers . . . . .	48
4.2	Vacuum System . . . . .	49
4.3	Magnetic Fields . . . . .	52
4.3.1	Quadrupole Coils . . . . .	52
4.3.2	Feshbach Coils . . . . .	53
4.4	Atom Source . . . . .	58
4.5	Magneto Optical Trap . . . . .	60
4.6	Dipole Trap . . . . .	62
4.6.1	Power Stabilisation . . . . .	68
4.7	Total Trapping Potential . . . . .	70
4.8	Imaging . . . . .	72
4.8.1	High Field Imaging for Lithium . . . . .	75

4.9	Control System . . . . .	77
4.10	Apparatus Outlook . . . . .	79
4.10.1	Magnetic Field Curvature Compensation . . . . .	79
4.10.2	Nufern Amplifier Trap . . . . .	80
4.10.3	Improving the Loading of the Dipole Trap . . . . .	80
<b>5</b>	<b>Experimental Scheme</b>	<b>82</b>
5.1	Zeeman Slower and MOT Loading . . . . .	83
5.2	MOT Cooling and Transfer Into Dipole Trap . . . . .	88
5.2.1	Compression and Optical Molasses . . . . .	88
5.2.2	State Preparation . . . . .	90
5.3	Evaporative Cooling of Lithium . . . . .	94
5.3.1	Scattering Cross-Section . . . . .	94
5.3.2	Plain Evaporation . . . . .	96
5.3.3	Forced Evaporation . . . . .	99
5.3.4	Feshbach Molecules . . . . .	101
5.4	Bose-Einstein Condensation . . . . .	103
5.4.1	Final Stage of Evaporation . . . . .	103
5.4.2	In-trap Density . . . . .	105
5.4.3	Expansion . . . . .	107
5.4.4	Condensate Properties . . . . .	109
<b>6</b>	<b>Conclusions and Outlook</b>	<b>116</b>
	<b>Bibliography</b>	<b>119</b>

## CHAPTER 1

# Introduction

“... experimentalists can actually make spherical cows.”

Galitski and Spielman [2]

*Hói*, *hoí* and *aibai* are the words the Pirahã, a hunter-gatherer tribe from the Amazon, use for counting. These words mean “one”, “two” and “many” and make up the entirety of their counting system [3]. Not unlike the Pirahã, our physical understanding progresses in this same mindset. Quantum mechanics development was, at first, a quest to understand one-particle systems (*hói*). Later, the nature of interactions were uncovered (*hoí*). At present, the study of many-body quantum mechanics is at center stage (*aibai*).

The simplest non-trivial system that can be studied with quantum mechanics is a two-level system. Such a system is represented by a 2-dimensional vector. When considering a system consisting of  $n$  particles, the state must be represented by a  $2^n$ -dimensional vector. Thus, the complexity of simulating a quantum system grows exponentially with the number of particles, making it intractable for as low as  $n = 40$  particles. Owing to this complexity, Richard Feynman suggested using controllable quantum systems to study these phenomena, which grow in complexity themselves in the same way [4].

Ultracold atoms have turned out to be an exceptionally good system for this purpose, both as an analogous realisation of other systems as well as interesting systems in their own right. As atoms are cooled (slowed) down, their de Broglie wavelength becomes larger and consequently their wave-functions overlap. This causes interference of the probability amplitudes and hence, a quantum-mechanical description is required.

The power of using ultracold atoms, both bosons and fermions, to study

many-body quantum mechanics lies in their versatility. The methods used are a bottom-up approach for understanding a complex quantum system. Different potentials and property-modifying mechanisms are added around the atoms to produce the sought-after physical system. For example, the strength of the interaction between the atoms can be modified using an external magnetic field close to a Feshbach resonance (see Section 2.5).

The potentials to which the atoms can be subjected range from simple harmonic potentials to arbitrarily shaped ones which can be modified in real time [5]. Very tight trapping can be engineered so that the dynamics of the system is confined to two [6, 7] and one dimension [8, 9]. Additionally, using overlapping laser beams it is possible to produce periodic potentials as a result of light interference [10, 11]. These optical lattices resemble a crystalline structure with no defects.

Adding to the list of techniques that can be used to realise physical systems with ultracold atoms, are synthetic magnetic fields. Neutral atoms are not susceptible to the Lorentz force and thus, phenomena that arise from it, such as the fractional quantum Hall effect, may seem out of reach. However, synthetic magnetic fields have been created using laser fields that have been arranged to produce a spatially-varying coupling between internal atomic states [12, 13].

A unique advantage of using ultracold atoms is the capability to probe them. Using optical imaging (see Section 3.5) their spatial distribution can be directly measured. Further, atoms in optical lattices can be imaged individually [14, 15]. All this versatility has been exploited with great success since the first quantum gases of bosons [16, 17] and fermions [18] were created.

Insight into quantum phase transitions, induced by quantum rather than thermal fluctuations, was gained when studying bosons in optical lattices. By varying the depth of the lattice wells, the relative weights of tunelling and on-site interaction were varied realising the superfluid to Mott insulator transition [11].

Questions of the relation between superfluidity, cooper pairing and Bose-Einstein condensation were addressed when condensates of paired fermions were observed [19–21]. In this system, which has been reproduced for this thesis, changing the interaction strength between the atoms allows experimentalists to explore the crossover between the Bose-Einstein condensate and degenerate Fermi gas regimes. Superfluidity had been suspected to occur throughout the crossover and was confirmed by the observation of quantised vortices [22].

Other prominent lines of research address questions of magnetism. Widely tunable classical magnetism simulators have been created using ultracold atoms [23].

Also, quantum spin systems have been realised with a site-occupation-to-spin mapping where a path to magnetic domain formation has been demonstrated [24]. Spin-orbit coupling links a particle's spin to its motional degrees of freedom. This mechanism is the basis for a wide array of many-body quantum phenomena such as topological insulators, the spin-Hall effect and Majorana fermions to name a few [2]. One type of spin-orbit coupling has been realised with ultracold atomic systems, opening the door to studying these systems with unprecedented control [25].

The work presented in this thesis deals with the construction of a new apparatus for the production and study of ultracold gases of bosonic caesium-133 and fermionic lithium-6. With this system, a new set of tools is added to the already vastly versatile set. Having two different atomic species allows for independent control of each of them. Additionally, the large mass ratio between them opens the door to new regions in the parameter space. Lithium and caesium have a wide tunability in their interaction strength, both in inter-species and intra-species collisions [26–29]. This mechanism can be used to produce LiCs vibrationally-excited molecules that can be subsequently transferred to their ground state. The resulting molecule has a permanent electric dipole moment of 5.5 D which is the largest of all possible alkali-metal combinations [30].

Independent control between the species can be used to delve into impurity physics. A general class of problems can be described in these terms [31]. Furthermore, exploiting the tunability provided by Feshbach resonances, a gas with only inter-species (LiCs) interactions may be produced [28].

The large caesium-to-lithium mass ratio presents an opportunity to study few-body physics such as Efimov states [32]. These are a predicted series of three-body states that appear while varying the scattering length. The scale of the separation between these states is theorised to be universal and only dependent on the mass ratio. With homonuclear trimers only a couple of states can be measured whereas with the lithium-caesium combination, more states within this series can be observed and the universality of the scaling tested [33, 34].

The dipole-dipole interaction, exhibited by ground-state LiCs molecules, is long-ranged and anisotropic. This means that the contact interaction, normally used to describe ultracold interactions between neutral atoms, is no longer sufficient. For instance, if placed in an optical lattice, interactions between atoms in different lattice sites are possible. This creates the possibility of creating a scalable quantum computer with long coherence times [35].

This dissertation documents work that was carried out in collaboration with the members of the ultracold mixtures lab from October 2010 until October 2014. When the author joined the group, preliminary vacuum and laser systems were in place and a magneto-optical trap for lithium had been demonstrated. As a result of this thesis, the first BEC in Nottingham was created; this is also the only molecular BEC in the United Kingdom. Additionally, the constructed apparatus is also capable of cooling and trapping bosonic caesium. A technical paper about an innovative dual-species cold-atom source, conceived during the design and construction of this experiment, was published [1].

This newly built apparatus can already be used to explore quantum gases throughout the BEC-BCS crossover, including the strongly interacting regime. With its additional capability to produce cold samples of caesium, LiCs Feshbach molecules and impurity physics can soon be studied. As part of this lab, two other theses have been produced by Dr. Sonali Warriar [36] and Dr. Matthew D. Jones [37] which contain details about the experiment which are not covered here.

This being an experimental thesis, it was possible to provide measurements which illustrate the concepts discussed. The contained chapters are structured as follows:

- **Chapter 2** contains a brief description of important physical concepts about atoms and their interactions used throughout this work.
- **Chapter 3** describes the principles behind the techniques used for cooling, trapping and imaging atoms.
- **Chapter 4** presents an overview of the implementation of this experiment including technical details and practical considerations of the apparatus.
- **Chapter 5** discusses the experimental sequence carried out and the results obtained with it.
- **Chapter 6** summarises this thesis and presents an outlook of experiments to be carried out with the apparatus in the near future.

## CHAPTER 2

# Theoretical Background

In this chapter the basic concepts necessary to understand the building blocks of this experiment are presented. The atomic structure and the mechanisms from which it arises are first described. It is then followed by a discussion of the effect that static magnetic fields have on this structure. Then, important results regarding the interaction between atoms and light are shown. Finally, the scattering between pairs of atoms and the possibility of controlling it via Feshbach resonances is considered. All of the aforementioned processes are the basis for the techniques used for trapping, cooling and manipulating atomic clouds.

## 2.1 Atomic Structure

Laser cooling was first observed in 1978 with  $\text{Mg}^+$  ions [38] and the techniques were later further developed for alkali atoms [39, 40]. What these atoms have in common is that they possess a single valence electron together with a core of electrons that form closed shells. In this section the structure of this kind of atoms, with a special attention to lithium and caesium, is discussed.

The total angular momentum of a closed shell of electrons is zero and thus, results in a spherically symmetric distribution which requires a high energy to disturb. In comparison, the outermost electron has the lowest excitation energy and therefore, its energy levels are the most relevant. Furthermore, it is this electron, in conjunction with the nucleus, which determines the magnetic moment of the atom and its interaction with light.

The gross structure of the energy levels of the valence electron can be well approximated using an hydrogen-like non-relativistic model. Here, the core electrons and nucleus add up to create an effective central potential. The Hamiltonian for

this model is given by

$$H_0 = \frac{\mathbf{p}^2}{2m_e} + V_{\text{eff}}(r),$$

where  $\mathbf{p}$  is the momentum of the valence electron,  $m_e$  its mass and  $V_{\text{eff}}$  the effective central potential. The solutions will have the familiar form, similar to the Hydrogen atom, given by the product of a radial and an angular function. This solutions can be expressed as

$$|n \ell m_\ell\rangle,$$

where  $n$ ,  $\ell$  and  $m_\ell$  are the principal, azimuthal and magnetic quantum numbers respectively. The energies of these states only depend on the principal quantum number, i.e. the different  $\ell$  levels are degenerate. However, this is far from sufficient for describing the level structure in the necessary detail used throughout this work. For instance, the largest atomic transition that is utilised in the experiment is a transition between two different  $\ell$  states which this coarse model doesn't describe.

A relativistic framework is required to understand the origin of the energy splitting between states with different values of  $\ell$ . In such a situation, additional quantum numbers for the spin  $\mathbf{S}$  naturally arise and the weakly relativistic Hamiltonian is given by [41]

$$H = m_e c^2 + \underbrace{\frac{\mathbf{p}^2}{2m_e} + V_{\text{eff}}(r)}_{H_0} - \frac{\mathbf{p}^4}{8m_e^3 c^2} + \frac{1}{2m_e^2 c^2} \frac{1}{r} \frac{dV_{\text{eff}}}{dr}(r) \mathbf{L} \cdot \mathbf{S} + \frac{\hbar^2}{8m_e^2 c^2} \Delta V_{\text{eff}}(r) + \dots$$

The additional terms of the Hamiltonian are smaller than  $H_0$  by a factor in the order of  $\alpha^2 = 1/137^2$ , with  $\alpha$  being the fine-structure constant [41]. The term proportional to  $\mathbf{L} \cdot \mathbf{S}$  is noteworthy because it removes the degeneracy between different  $\ell$  states. It arises from the interaction of the electron's magnetic moment associated to its spin, with the magnetic field created by its orbit. The level structure that results from this term is called the *fine structure*.

The eigenvalues of the fine-structure operator are best expressed in the basis spanned by the electron's total angular momentum operator  $\mathbf{J} = \mathbf{L} + \mathbf{S}$ . The eigenstates  $|n \ell m_\ell s m_s\rangle$  are then written as linear combinations of  $|n \ell s j m_j\rangle$ .

The fine-structure operator written as

$$A_{\text{fs}} \frac{\mathbf{L} \cdot \mathbf{S}}{\hbar^2} = \frac{A_{\text{fs}}}{2\hbar^2} (\mathbf{J}^2 - \mathbf{L}^2 - \mathbf{S}^2)$$

is already diagonal in this basis. The eigenvalues can be readily obtained by applying this operator, from which it is clear that different  $\ell$  states result in different eigenvalues.

A further degree of refinement is achieved when considering the interaction of the magnetic moments of the electron and nucleus. This effect is in the order of 2000 times weaker than that of the fine structure [41]. Using the nuclear angular momentum operator  $\mathbf{I}$  and an atomic species-dependent, hyperfine splitting constant  $A_{\text{hfs}}$  the interaction Hamiltonian can be written as

$$H_{\text{hfs}} = A_{\text{hfs}} \frac{\mathbf{I} \cdot \mathbf{J}}{\hbar^2},$$

as long as  $j$  remains a good quantum number. This will usually be the case because the magnetic fields attainable in the laboratory can only produce energy-level shifts much smaller than the fine-structure splitting. The eigenvalues can again be found in terms of the total angular momentum operator  $\mathbf{F} = \mathbf{I} + \mathbf{J}$ . The atomic eigenstates can be written in the form

$$|n \ell s j i f m_f\rangle.$$

The energy eigenvalues will depend on all indices with the exception of  $m_f$ . An anisotropy such as an external magnetic field is necessary to break the  $m_f$  degeneracy. The resulting level structures for lithium and caesium are shown in Figure 2.1.

The typical linewidth for the transitions shown in Figure 2.1 are  $\sim 5$  MHz. Such transitions can be precisely addressed with external-cavity diode lasers used in the experiment, the linewidth of which is below 1 MHz. The exception to this are the  $D_2$  transitions of lithium where the different levels are separated less than the linewidth, and the total effective linewidth is much broader. This has consequences, for the cooling mechanisms, which are discussed in Subsection 3.2.1.

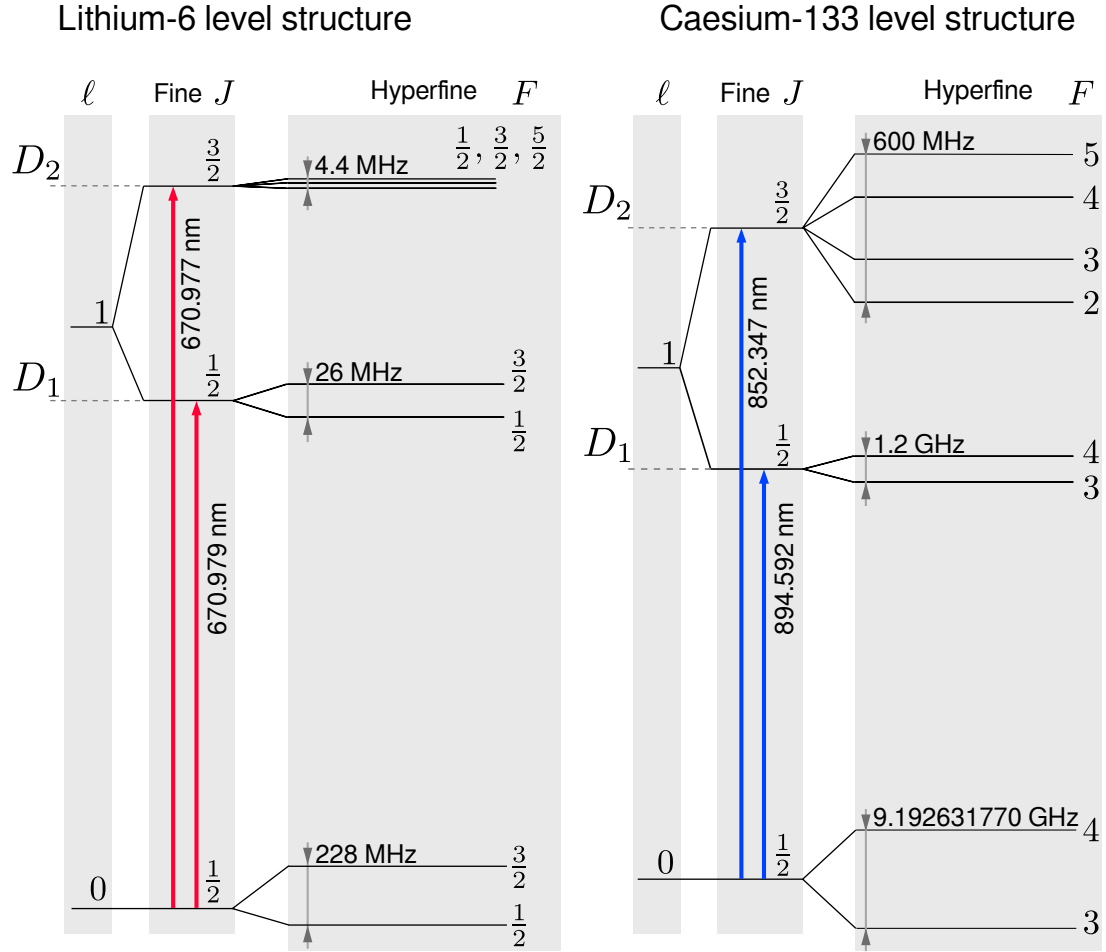


**Figure 2.1:** Atomic energy structure for lithium and caesium including fine and hyperfine structure. The separation between the levels is not to scale. The linewidth of the excited states is  $\sim 5$  MHz, therefore all the  $D_2$  states of lithium overlap. Data for lithium was obtained from [42] and for caesium from [43].

## 2.2 Interaction with Static Magnetic Fields

Static magnetic fields are a frequently used tool for manipulating the atoms. They are applied to affect the level structure and therefore, understanding the effect that magnetic fields have on atoms is essential.

A magnetic field ( $\mathbf{B}$ ), external to the atom, will interact with its nuclear ( $\boldsymbol{\mu}_I$ ), orbital ( $\boldsymbol{\mu}_L$ ) and electronic ( $\boldsymbol{\mu}_S$ ) magnetic moments. The interaction Hamiltonian is

$$H_Z = -\mathbf{B} \cdot (\boldsymbol{\mu}_L + \boldsymbol{\mu}_S + \boldsymbol{\mu}_I).$$

Usually the term with  $\boldsymbol{\mu}_I$  can be neglected since it is  $\sim 2000$  times smaller than

the remaining two terms [43].

The eigenvectors of  $H_Z$  are of the form  $|n \ell m_\ell s m_s i m_i\rangle$ . However, this does not describe the full physical picture because the Zeeman and hyperfine Hamiltonians may have a comparable magnitude which will cause the eigenstates to intermingle. To accurately determine the structure, the magnetic Hamiltonian to consider is

$$H_{\text{mag}} = \frac{A_{\text{hfs}}}{\hbar^2} \mathbf{I} \cdot \mathbf{J} - \mathbf{B} \cdot (\boldsymbol{\mu}_L + \boldsymbol{\mu}_S) = \frac{A_{\text{hfs}}}{\hbar^2} \mathbf{I} \cdot \mathbf{J} - \frac{\mu_B B}{\hbar} (g_S S_z + g_L L_z),$$

where  $\mu_B$  is Bohr's Magneton and,  $g_S$  and  $g_L$  are the corresponding gyromagnetic ratios. This Hamiltonian may be diagonalised analytically in the subspace of  $\ell = 0$ . Additionally, good approximations may be obtained for extreme regimes where either the hyperfine or the Zeeman term dominate. However, for this work it is of interest to obtain solutions for the entire range of magnetic fields for its applications to high-field imaging of lithium (see Subsection 4.8.1) and to the design of a Zeeman slower (see Section 3.1). A method for numerically finding the levels is therefore outlined.

The method consists in writing the matrix representation of the Hamiltonian in the  $|\ell s j m_j i m_i\rangle$  basis which can then be numerically diagonalised. First, the hyperfine term of the Hamiltonian is rewritten with

$$\mathbf{I} \cdot \mathbf{J} = I_z J_z + \frac{1}{2} [I_+ J_- + I_- J_+]$$

so that it can be directly applied to this basis. Off-diagonal terms result from  $I_\pm J_\mp$ .

Applying the  $L_z$  or  $S_z$  operators to the  $|\ell s j m_j i m_i\rangle$  basis is not as straightforward. It is done by first writing them as a linear combination of  $|\ell m_\ell s m_s i m_i\rangle$  vectors using their completeness relation. Written as such, the application of  $L_z$  or  $S_z$  is immediate. The result, after applying  $L_z$ , is

$$L_z |\ell s j m_j\rangle = \sum_{m_\ell, m_s} m_\ell |\ell m_\ell s m_s\rangle \langle \ell m_\ell s m_s | \ell s j m_j\rangle,$$

in which the  $|i m_i\rangle$  ket has been omitted for conciseness. The  $\langle \ell m_\ell s m_s | \ell s j m_j\rangle$  term is a Clebsch-Gordan coefficient. Evaluating the matrix element for  $L_z$ ,

another Clebsch-Gordan coefficient appears

$$\langle \ell s j' m'_j | L_z | \ell s j m_j \rangle = \sum_{m_\ell, m_s} m_\ell \langle \ell s j' m'_j | \ell m_\ell s m_s \rangle \langle \ell m_\ell s m_s | \ell s j m_j \rangle.$$

The matrix elements for  $S_z$  are calculated in the same way.

Bringing all the pieces together, the matrix representation of the Hamiltonian is obtained. This can then be numerically diagonalised for different values of the magnetic field. The energy levels are obtained relative to the fine structure energies. This calculation has been carried out for the range of magnetic fields that can be produced in the experiment. The results for lithium are shown in figures 2.2 and 2.3, and for caesium in figures 2.4 and 2.5.

For fields above 200 G, both the ground and excited states of lithium are in the high field regime. This fact facilitates the implementation of high field imaging (see Section 4.8.1) as the transitions at this point are closed and, therefore, no additional re-pumping laser is needed.

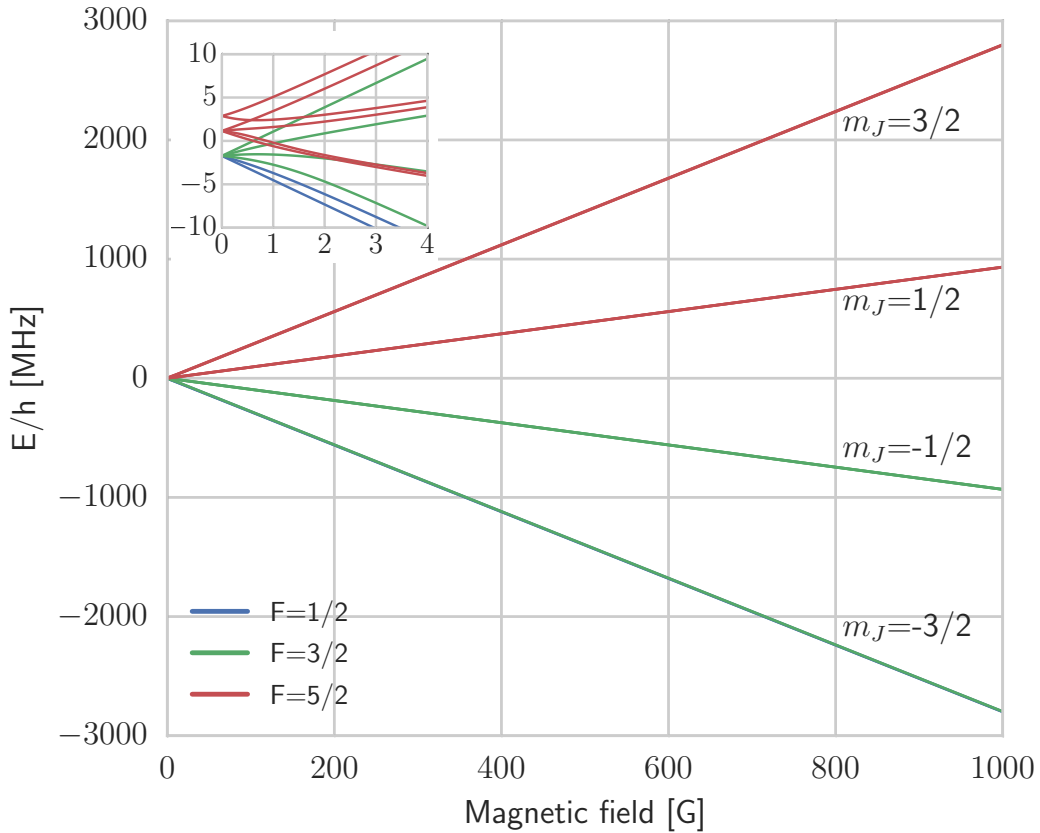


**Figure 2.2:** Calculated Breit-Rabi diagram of the lithium-6  $^2P_{3/2}$  manifold. Inset shows a detailed view at low field. The high-field regime is reached already at a few G.

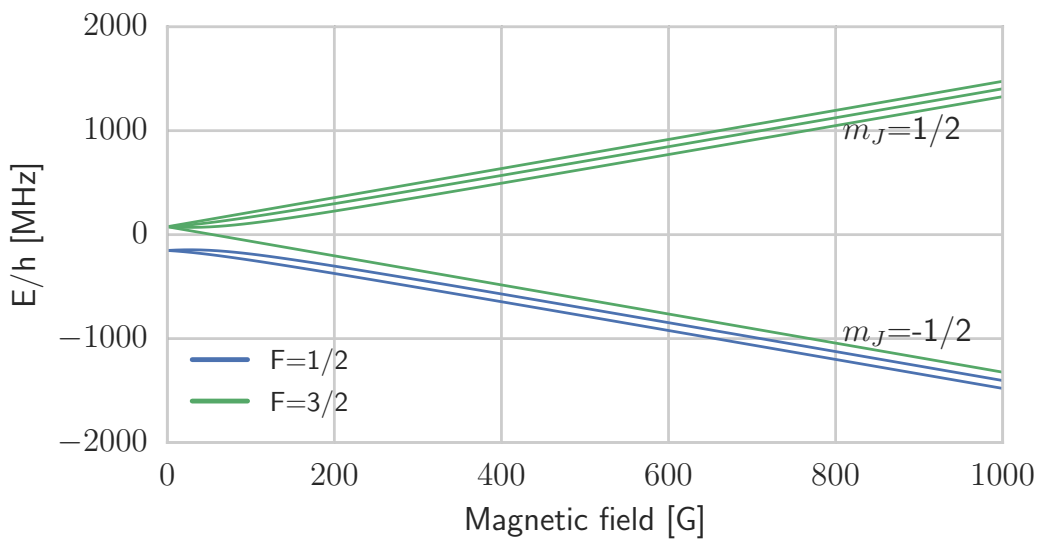


**Figure 2.3:** Calculated Breit-Rabi diagram of the lithium-6  $^2S_{1/2}$  manifold. It can be seen by the curvature of the levels that above 200 G the high-field regime is reached.

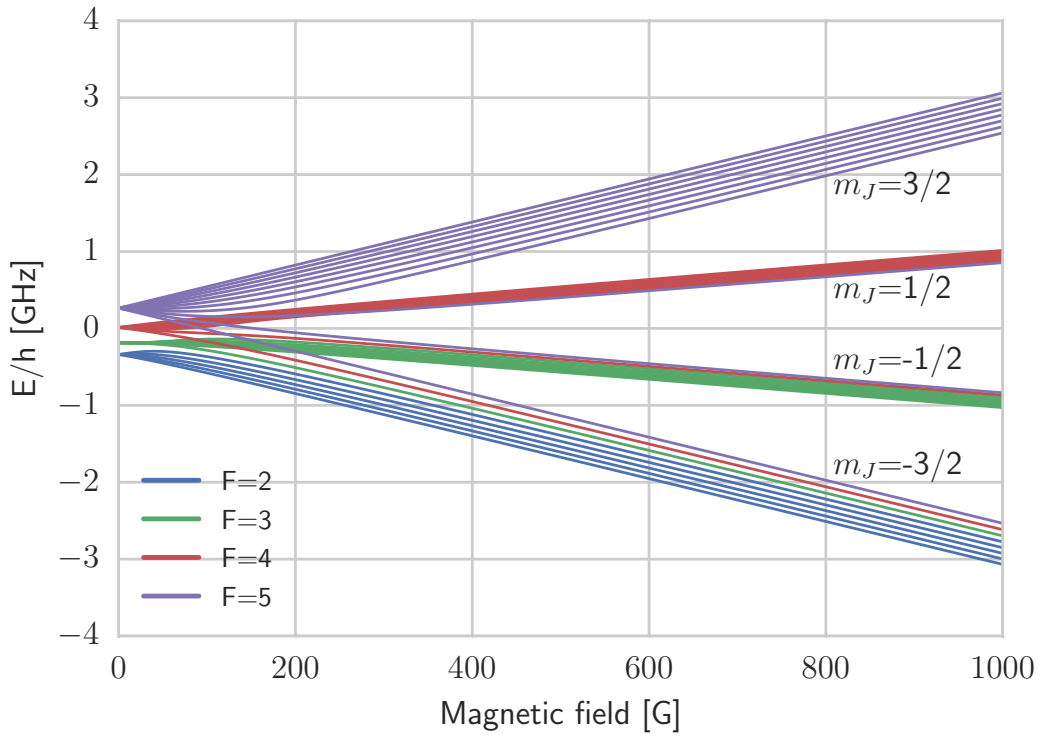


**Figure 2.4:** Calculated Breit-Rabi diagram of the caesium-133  $^2P_{3/2}$  manifold. It can be seen by the curvature of the levels that above 250 G the high-field regime is reached.

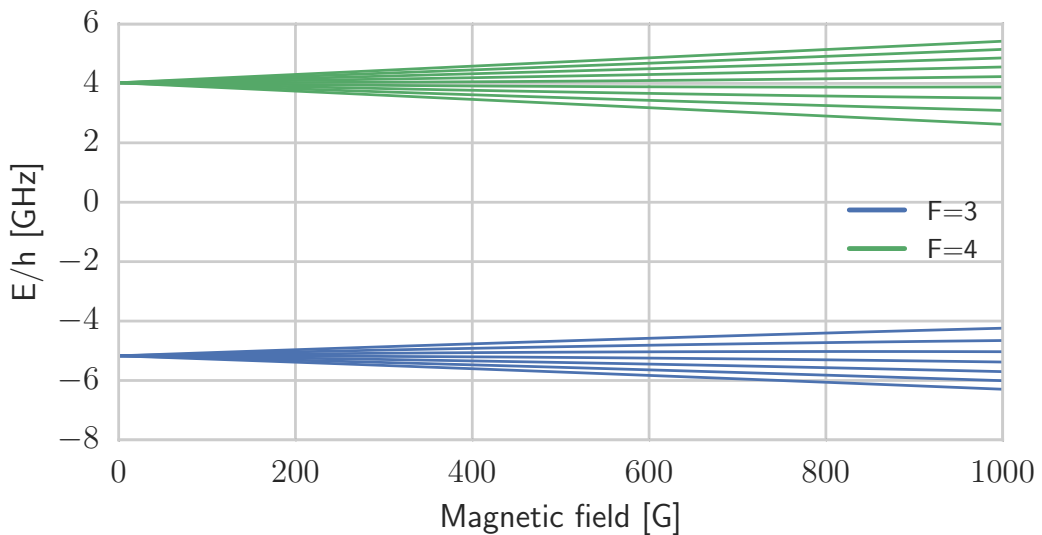


**Figure 2.5:** Calculated Breit-Rabi diagram of the caesium-133  $^2S_{1/2}$  manifold. The hyperfine term in the Hamiltonian is dominant throughout the entire range and the external magnetic field could be treated as a perturbation.

## 2.3 Interaction of Atoms with Light

The interaction between atoms and light is a fundamental process that affects the internal state of the atoms as well as external degrees of freedom by exerting forces upon them. These processes form the basis of laser cooling and trapping, which has a central role throughout this work.

As was discussed in the previous sections, atoms have a complex internal structure. However, in many situations, the light's frequency is much closer to a given transition than to the rest and therefore, their effect can be neglected. Additionally, optical pumping may drive atoms into a stationary state which effectively has the dynamics of a two-level atom. In this section, relevant results that arise from a semi-classical two-level-atom model are discussed based on [44] and [45].

The Hamiltonian for an atom with levels  $|g\rangle$  and  $|e\rangle$ , separated by an energy  $\hbar\omega_0$ , interacting with a classical electric field  $\mathbf{E} = \hat{\epsilon} (E_0^+ e^{-i\omega t} + E_0^- e^{+i\omega t})$  in the dipole approximation is given by

$$H = H_A + H_{AF} = \hbar\omega_0 |e\rangle \langle e| - \mathbf{d} \cdot \mathbf{E},$$

where  $\mathbf{d} = -e\mathbf{r}$  is the electric dipole moment which we can write in terms of its positive and negative rotating components  $\mathbf{d} = \mathbf{d}^+ + \mathbf{d}^-$ . The detuning between the driving field and the atomic resonance frequency is defined as  $\delta = \omega - \omega_0$ .

Assuming that the frequency of the driving field is close to the atomic transition, which has already been partly assumed when simplifying the atom to a two-level system, the rotating-wave approximation can be made. In this approximation, fast oscillating terms of the interaction Hamiltonian are averaged out. This approximation is valid as long as we are only interested in “slow” signals with a frequency below optical frequencies. After defining the Rabi frequency as

$$\Omega = -\frac{1}{\hbar} 2 \langle g | \hat{\epsilon} \cdot \mathbf{d} | e \rangle E_0^+,$$

the rotating-frame Hamiltonian can be stated as

$$\tilde{H} = -\hbar\Delta |e\rangle \langle e| + \frac{\hbar}{2} [\Omega^* \sigma + \Omega \sigma^\dagger].$$

The lowering operator  $\sigma = |g\rangle \langle e|$  and its conjugate have been used.

The time evolution of the density operator

$$\rho = \rho_{ee} |e\rangle\langle e| + \rho_{ge} |g\rangle\langle e| + \rho_{eg} |e\rangle\langle g| + \rho_{gg} |g\rangle\langle g|$$

is governed by

$$\partial_t \tilde{\rho} = -\frac{i}{\hbar} [\tilde{H}, \tilde{\rho}], \quad (2.1)$$

where the tilde ( $\sim$ ) indicates it is in the rotating frame. However, given that the treatment of the electric field is classical, this Hamiltonian does not account for the coupling that the excited state has with a continuum of states of the field. This coupling is responsible for spontaneous emission. Nonetheless, the behaviour of this process is well reproduced by including decay terms into the time evolution equations. For a decay rate of the excited state  $\Gamma$ , the steady state solutions to Equation 2.1 take the form

$$\tilde{\rho}_{ee} = \rho_{ee} = \frac{|\Omega|^2/\Gamma^2}{1 + (2\delta/\Gamma)^2 + 2|\Omega|^2/\Gamma^2},$$

and

$$\tilde{\rho}_{eg} = -\frac{i\Omega}{2(\Gamma/2 - i\delta)(1+s)} = -\frac{i\Omega}{\Gamma} \frac{1 + 2i\delta/\Gamma}{1 + (2\delta/\Gamma)^2 + 2|\Omega|^2/\Gamma^2}.$$

The dipole moment, induced by the applied electric field, can be written as

$$\mathbf{d}^+ = \alpha \mathbf{E}^+,$$

where the atomic polarisability  $\alpha$  is a complex proportionality constant. This quantity is useful for summarising the atom-field interactions. For the two-level atom, the polarisability takes the form

$$\alpha = i \frac{c\epsilon_0\hbar\Gamma}{2I_{\text{sat}}} \frac{1 + i2\delta/\Gamma}{1 + (2\delta/\Gamma)^2 + I/I_{\text{sat}}}, \quad (2.2)$$

using that the saturation intensity  $I_{\text{sat}}$  is defined by  $I/I_{\text{sat}} = 2\Omega^2/\Gamma^2$ . From this, the scattering rate at which absorption-emission processes take place can be obtained

$$R_{\text{sc}} = \Gamma \rho_{ee} = \frac{1}{\hbar\epsilon_0 c} \text{Im}\{\alpha\} I = \frac{\Gamma}{2} \frac{I/I_{\text{sat}}}{1 + (2\delta/\Gamma)^2 + I/I_{\text{sat}}}. \quad (2.3)$$

To calculate the mechanical effect that light has on the atom, the spatial dependence of the electric field's amplitude must be taken into consideration. The

time derivative of the momentum operator is found to be

$$\mathbf{F} = \partial_t p = \frac{i}{\hbar} [H, p] = -\nabla H_{\text{AF}} = -\frac{\hbar}{2} [\nabla \Omega^*(r) \sigma + \nabla \Omega(r) \sigma^\dagger],$$

Defining  $\Omega = |\Omega(r)|e^{i\phi(r)}$ , the expectation value of the force, time-averaged over an optical period, is

$$\langle \mathbf{F} \rangle = \text{Tr} [\mathbf{F} \rho] = 2\rho_{ee}\hbar\Gamma \left[ -\frac{\delta}{\Gamma} \frac{\nabla|\Omega|}{|\Omega|} + \frac{1}{2} \nabla\phi \right] = \langle \mathbf{F}_{\text{dip}} \rangle + \langle \mathbf{F}_{\text{rad}} \rangle,$$

where the spatial dependence of  $|\Omega|$  and  $\phi$  has been omitted for compactness. The term proportional to  $\nabla|\Omega|$  corresponds to the dipole force, while the one proportional to  $\nabla\phi$  is the radiation-pressure force. Depending on the value of  $\delta$ , either  $\langle \mathbf{F}_{\text{dip}} \rangle$  or  $\langle \mathbf{F}_{\text{rad}} \rangle$  will be dominant. When  $\delta \gg \Gamma$ , the dipole force term is most important. Conversely, for  $\delta \sim \Gamma$ , the radiation-pressure term dominates.

The radiation pressure force has the form

$$\langle \mathbf{F}_{\text{rad}} \rangle = R_{\text{sc}}\hbar\nabla\phi = \frac{\Gamma}{2} \frac{I/I_{\text{sat}}}{1 + (2\delta/\Gamma)^2 + I/I_{\text{sat}}} \hbar\nabla\phi. \quad (2.4)$$

The vector  $\nabla\phi$  points in the direction of travel of the wave-front. For a plane wave  $\phi = \mathbf{k} \cdot \mathbf{r}$  and therefore,  $\nabla\phi = \mathbf{k}$ . This force is the resulting average effect of multiple absorption and emission events, each of which provides a change of momentum  $\hbar\mathbf{k}$ . Since the spontaneous emission events occur in a random direction they average out, leaving only the absorption contribution to the average force.

The detuning indicated in the previous equations is the difference between the atom's resonance frequency and the frequency of the driving field. However, this is dependent on the frame of reference due to the Doppler shift. In the case where  $\delta \sim \Gamma$ , this shift will have a significant effect. This velocity dependence of the radiation-pressure force plays a crucial role in laser-cooling (see Section 3.2).

In contrast, when  $\delta \gg \Gamma$ , not only the radiation term is negligible but also the velocity dependence of the force. In this case, the dipole force is conservative and therefore can be derived from a potential. In this regime, the dipole potential takes the form

$$V_{\text{dip}}(r) = -\frac{1}{2\epsilon_0 c} \text{Re} \{ \alpha \} I(r) \approx \frac{\hbar|\Omega|^2}{4\delta} = \frac{\hbar\Gamma^2}{8\delta} \frac{I(r)}{I_{\text{sat}}}. \quad (2.5)$$

However, if the light is far detuned from the transition, the two-level-atom

model may not be accurate and other energy levels should be considered. If the detuning is large compared to the separation between the levels, considering the levels as a single one will suffice. Nonetheless, when these are comparable, each level must be accounted for separately.

In the experiment presented in this work, a potential is created using a 1070 nm laser (see Section 4.6). The detuning of this light from the  $D_2$  transition of caesium is comparable to the separation between the  $D_1$  and  $D_2$  lines. To accurately calculate the polarisability, both transitions should be accounted for. The hyperfine splitting in lithium-6 is much smaller than the detuning from this optical trap so both manifolds may be considered as a single level. The details discussed in this section will be important for the calculation of the dipole trapping potential discussed in sections 3.3 and 4.6.

## 2.4 Scattering Theory

So far, only properties of single, isolated atoms have been discussed. In this section, the interaction between pairs of atoms is described based on [46]. This description is of particular importance because the quantities that parametrise this process are relevant in the description of macroscopic ensembles of atoms.

The collision between two particles is best described in the center-of-mass reference frame. Then, it can be understood as the collision of a particle with wave vector  $\mathbf{k}$  and a scattering centre at the origin. Far from the scattering centre, the wave function can be written as

$$\psi_k(\mathbf{r}) \sim e^{i\mathbf{k} \cdot \mathbf{r}} + f_k(\hat{\mathbf{r}}) \frac{e^{ikr}}{r}.$$

That is, an incoming plane wave which is scattered into an outgoing spherical wave with an angular distribution defined by the scattering amplitude  $f_k(\hat{\mathbf{r}})$ . This amplitude can be calculated using Schrödinger's equation and is particularly relevant because it can be directly related to the scattering cross-section which is an experimentally measurable quantity. The scattering amplitude and differential cross-section are related by

$$\frac{d\sigma}{d\Omega}(\hat{\mathbf{r}}) = |f_k(\hat{\mathbf{r}})|^2.$$

However, this result is only true for distinguishable particles. For bosons or

fermions, the scattering amplitude must have the corresponding symmetry. Therefore, the differential scattering amplitudes in each case are

$$\frac{d\sigma_{\text{boson}}}{d\Omega}(\hat{\mathbf{r}}) = |f_k(\hat{\mathbf{r}}) + f_k(-\hat{\mathbf{r}})|^2 \quad \text{and} \quad \frac{d\sigma_{\text{fermion}}}{d\Omega}(\hat{\mathbf{r}}) = |f_k(\hat{\mathbf{r}}) - f_k(-\hat{\mathbf{r}})|^2. \quad (2.6)$$

For a central scattering potential (only dependent on the magnitude of the relative coordinate) the angular ( $Y$ ) and radial ( $R$ ) parts of the Schrödinger equation can be separately solved. In this manner, the general solution has the form

$$\psi_k(\mathbf{r}) = \sum_{\ell=0}^{\infty} \sum_{m=-\ell}^{\ell} c_{\ell m}(k) Y_{\ell m}(\theta, \phi) R_{\ell}(r). \quad (2.7)$$

The angular solutions are spherical harmonics  $Y_{\ell m}(\theta, \phi)$ . The radial solutions obey a 1D-Schrödinger-like equation

$$\left[ -\frac{\hbar^2}{2m_r} \frac{d^2}{dr^2} + \frac{\hbar^2}{2m_r} \frac{\ell(\ell+1)}{r^2} + V(r) \right] r R_{\ell}(r) = E r R_{\ell}(r),$$

which has a centrifugal term. An effective potential which includes this term,

$$V_{\text{eff}}(r) = \frac{\hbar^2}{2m_r} \frac{\ell(\ell+1)}{r^2} + V(r), \quad (2.8)$$

may be considered. The long range part of  $V(r)$  arises from the van der Waals potential which has the form  $-C_6/r^6$ . However, at this range the centrifugal term, proportional to  $r^{-2}$ , will dominate over the faster-decaying  $r^{-6}$  term. Hence, in the effective potential there is a barrier as a result of the centrifugal contribution, the height of which grows quadratically with  $\ell$ .

According to Equation 2.7, the solution from which the scattering amplitude is to be obtained is built out of terms with different values of  $\ell$ . However, for there to be a contribution of angular momentum  $\ell$ , the kinetic energy of the incoming particle must overcome the corresponding centrifugal barrier. In the limit where the kinetic energy is below the  $\ell = 1$  barrier, only the  $\ell = 0$ , known as the s-wave contribution is relevant to the scattering amplitude. In this case, the scattering amplitude reduces to

$$f_k(\hat{\mathbf{r}}) = -\frac{a}{1 + iak}, \quad (2.9)$$

where the scattering length  $a$  is a real number that summarises the effect of the scattering potential. The exact value of  $a$  is different for each type of colliding

partners and it is often possible to control it using external magnetic fields (see Section 2.5). The total s-wave scattering cross-section for distinguishable particles is then

$$\sigma = \int \frac{d\sigma}{d\Omega} d\Omega = \frac{4\pi a^2}{1 + a^2 k^2}. \quad (2.10)$$

Given that the scattering amplitude in Equation 2.9 does not depend on  $\hat{\mathbf{r}}$ , the scattering cross-section for identical fermions is zero. Generally, fermions can only collide at higher kinetic energies.

The height of the centrifugal barrier for  $\ell = 1$  is 8 mK for lithium and 35  $\mu$ K for caesium. Due to the symmetry requirements of the wave-function, the  $\ell = 1$  contribution will only be relevant for caesium if the particles are distinguishable, i.e. in different internal states. Otherwise, the next relevant contribution is the one with  $\ell = 2$ . These values are calculated based on Equation 2.8 using van der Waals  $C_6$  coefficients from [47].

## 2.5 Feshbach Resonances

Feshbach resonances are an invaluable tool for controlling the collisional properties of an ultracold gas using a magnetic field. In this section, the cause and characteristics of these resonances are discussed.

Given an interaction potential between two atoms, a scattering length may be calculated. The scattering length would then be enough to fully characterise an s-wave collision between them. However, in this treatment, several aspects of the collision have been neglected. A more accurate description includes both the internal structure of the atoms as well as different interaction potentials that depend on their internal state. Using external magnetic fields, the internal structure and, therefore, the related potentials can be altered. Fortunately, the result of accounting for these effects provides a handle with which the scattering length may be easily controlled. This feature is known as a Feshbach resonance [48, 49].

In a real system, the interaction between two atoms, at short distances, is predominantly determined by the valence electrons. In the Born-Oppenheimer approximation, the interaction potential between the two nuclei is determined as a result of the electronic state [41]. Their wave functions must be anti-symmetric with respect to the exchange of labels and therefore, must have one of the following forms:

$$\psi_S(\mathbf{r}_1, \mathbf{r}_2)\chi_A(s_1, s_2) \text{ or } \psi_A(\mathbf{r}_1, \mathbf{r}_2)\chi_S(s_1, s_2),$$

where  $\psi$  denotes the spatial part of the wave-function and  $\chi$  the spin part. The  $A$  and  $S$  labels indicate whether the function is symmetric ( $S$ ) or anti-symmetric ( $A$ ). The symmetric spin function corresponds to the triplet while the anti-symmetric is the singlet state. The Born-Oppenheimer potentials resulting from  $\psi_S$  and  $\psi_A$  are different. Therefore, a different potential will affect the atoms depending on the spin state. In general, if two atoms approach a collision in the ground state, only one of these potentials will be energetically accessible. Thus, the potential that is accessible is referred to as the open-channel potential while the one which is out of reach is the closed-channel potential [49].

The energy difference between the two potentials may be controlled by means of the Zeeman effect. The singlet state has a total magnetic quantum number  $M_S = 0$ . On the other hand, the triplet has three possible values, namely  $M_S = -1, 0, 1$ . Therefore, using a magnetic field, the states with non-zero  $M_S$  of the triplet can be shifted relative to the singlet state which is not affected by the magnetic field.

An additional relevant term in the Hamiltonian is the hyperfine term, which for both atoms has the form [50]

$$H_{\text{hfs}} = \frac{A_{\text{hfs}}}{\hbar^2} [\mathbf{S}_1 \cdot \mathbf{I}_1 + \mathbf{S}_2 \cdot \mathbf{I}_2] = \frac{A_{\text{hfs}}}{2\hbar^2} [(\mathbf{S}_1 + \mathbf{S}_2) \cdot (\mathbf{I}_1 + \mathbf{I}_2) + (\mathbf{S}_1 - \mathbf{S}_2) \cdot (\mathbf{I}_1 - \mathbf{I}_2)].$$

The first term inside the square bracket does not change the total spin  $\mathbf{S} = \mathbf{S}_1 + \mathbf{S}_2$ . On the other hand, the second term couples the singlet and triplet spin states. This coupling provides a mechanism through which the scattering properties of the open channel may be altered by the presence of a closed channel energy level.

A simple model using box potentials as shown in Figure 2.6 provides insight into this mechanism [48]. A two-state atom ( $|o\rangle$  and  $|c\rangle$ ), which is affected by different potentials depending on the internal state, is required. The  $|o\rangle$  and  $|c\rangle$  states are affected by the open and closed channel potentials  $V_o(r)$  and  $V_c(r)$  respectively. The separation between the energy continuum and the nearest eigenstate of the closed-channel potential is  $E_c$  when there is no magnetic field. An external magnetic field  $B$  can be used to shift this separation by  $\mu B$  with  $\mu = \mu_o - \mu_c$  being the relative magnetic moment between the open and closed channels. A coupling  $\Omega > 0$  between the open and closed channels is necessary for the model to exhibit Feshbach resonances. The resulting Schrödinger equation in the centre of mass reference frame is

$$E |\psi\rangle = \left( -\frac{\hbar^2}{2m_r} \nabla^2 + \hat{V}(r) \right) |\psi\rangle,$$

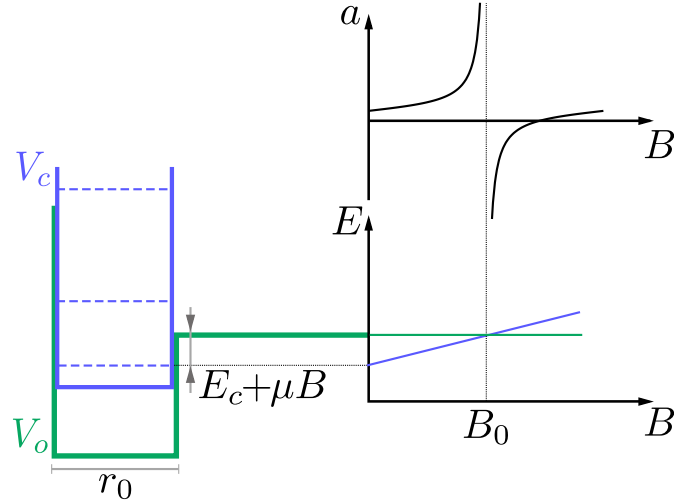


**Figure 2.6:** Simple model for Feshbach resonance. Two box potentials, an open ( $V_o$ ) and a closed one ( $V_c$ ), can be shifted relative to each other using a magnetic field  $B$  as a result of their relative magnetic moment  $\mu$ . When the energy of the bound state of the closed potential intersects the open channel continuum a Feshbach resonance occurs. As a consequence, the scattering length  $a$  can be controlled.

where  $m_r$  is the reduced mass and

$$\hat{V}(r) = \begin{cases} \begin{pmatrix} V_o & \Omega \\ \Omega & V_c(B) \end{pmatrix} & \text{for } r < r_0 \\ \begin{pmatrix} 0 & 0 \\ 0 & \infty \end{pmatrix} & \text{for } r > r_0 \end{cases}$$

is the potential energy operator.

The eigenfunctions of this system can be found analytically [48] and the resulting scattering length calculated. In the limit where  $\Omega \ll V_o, V_c$  the scattering length as a function of magnetic field can be written as

$$a = a_{\text{bg}} \left( 1 - \frac{\Delta_B}{B - B_0} \right).$$

The background scattering length  $a_{\text{bg}}$  is the scattering length that results from the open-channel potential. The position of the resonance is  $B_0 = -E_c/\mu - B_\Omega$  and the resonance width  $\Delta_B = B_\Omega \left( 1 - \frac{r_0}{a_{\text{bg}}} \right)$ . Finally, the parameter  $B_\Omega$ , a characteristic

field that quantifies the strength of the coupling, is proportional to  $\Omega^2$ .

Close to a Feshbach resonance a molecule can form on the side where it is energetically favourable. In Figure 2.6, this corresponds to the region in the left of  $B_0$ . The spatial wave-function of these molecules extends to a large size in the order of  $a$  and their binding energy the vicinity of the resonance is

$$E_b = \frac{\hbar^2}{2m_r a^2}.$$

In contrast to the model presented here, real atomic potentials have several bound states and more possible scattering channels. The full behaviour of the scattering length as a function of magnetic field is shown in Figure 2.7 for lithium and Figure 2.8 for caesium. The inter-species Feshbach resonances between lithium-6 and caesium-133 have also been measured [28, 29].

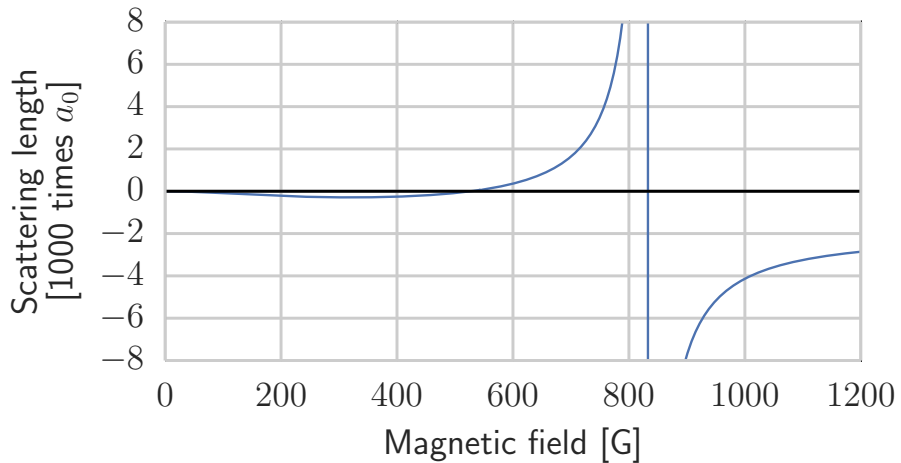


**Figure 2.7:** Lithium scattering length for a collision between the two lowest energy states. Data from [26].

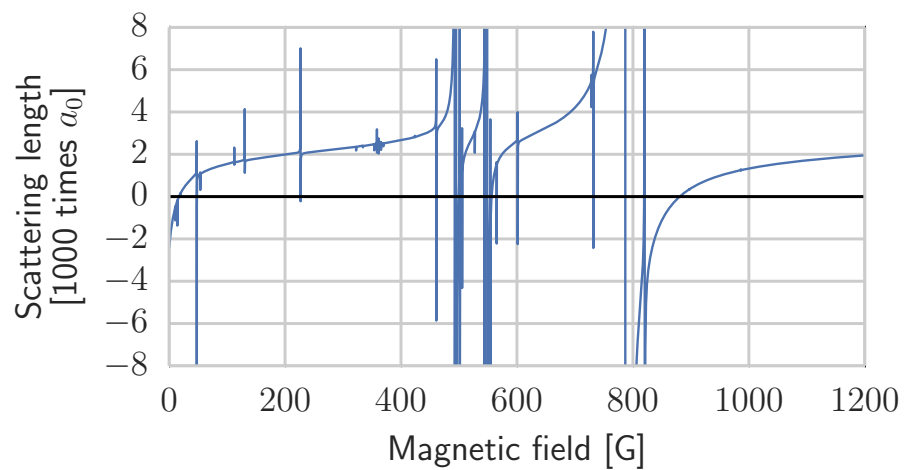


**Figure 2.8:** Caesium scattering length for a collision between the two lowest energy states. Data from [27].

## CHAPTER 3

# Atom Cooling, Trapping and Imaging

The field of ultracold atoms started with the advent of laser cooling [38–40] which allowed experimentalists to achieve temperatures well below 1 mK . This, however, was not sufficient to reach the necessary phase-space density required to observe quantum degeneracy [51]. Therefore, other cooling methods were required. Evaporative cooling was developed [52, 53] and successfully used to produce the first quantum degenerate gases [16, 17]. In this work a similar path has been followed and the principles of the relevant techniques are described in this chapter.

### 3.1 Zeeman Slower

The path of an atom through the experiment begins when a stream of atoms is produced by collimating the output of an effusive oven. In order to provide a high flux of trappable atoms for the magneto-optical trap (MOT) stage that follows, atoms from the atomic beam are slowed down to the MOT’s capture velocity.

To slow down the atoms in the atomic beam, resonant light is shone onto them to produce a radiation pressure force opposite to their direction of travel. However, as an atom slows down, the Doppler shift of the incoming light will change and it will no longer be resonant with the atom. The clever idea behind the Zeeman slower [39] is to use a magnetic field to compensate for the change in Doppler shift as the atoms slow down and, thus, achieve constant deceleration.

The effective laser detuning  $\delta'$  including the Doppler and magnetic shifts is

$$\delta' = \delta - \frac{\mu B}{\hbar} + kv, \quad (3.1)$$

where  $\mu$  is the magnetic moment of the transition,  $B$  the magnetic field,  $\delta$  is the detuning from the transition of an atom in the lab frame,  $v$  is the velocity of the atoms and  $k$  the wave number of the light. For the Zeeman slower to compensate the Doppler shift, by shifting the energy levels using a magnetic field, the effective detuning must satisfy  $\delta' = 0$ .

For a constant deceleration  $-a_0$  in direction  $z$ , the velocity of the atoms will satisfy the following relation:

$$v(z) = \sqrt{v_0^2 - 2a_0 z}, \quad (3.2)$$

with  $v_0$  the initial velocity of the atoms. Thus, combining equations 3.1 and 3.2, the desired profile for the magnetic field is

$$B(z) = \frac{\hbar}{\mu} \left( \delta + k \sqrt{v_0^2 - 2a_0 z} \right).$$

The value of  $a_0$  is determined by the on-resonance radiation pressure force (see Section 2.3)

$$ma_0 = F_{\text{scat}} = \frac{\Gamma}{2} \frac{I/I_{\text{sat}}}{1 + I/I_{\text{sat}}} \hbar k.$$

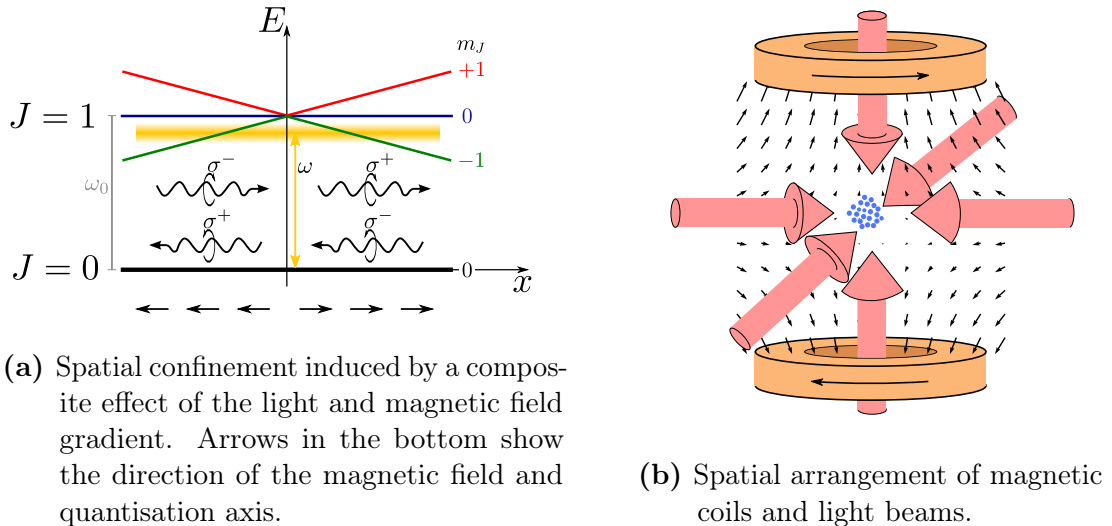
For the purpose of designing a Zeeman slower, the magnetic field profile should be chosen in such a way that the deceleration necessary to follow that profile is guaranteed to be achieved. This will depend on the power of the light used together with the atomic structure.

## 3.2 Magneto-Optical Trap

Atoms leaving the Zeeman slower are captured by a magneto-optical trap (MOT) [54]. This trap provides the means to simultaneously trap and cool neutral atoms. Typically in a MOT, temperatures below 1 mK are achieved [55].

As the name suggests, this technique uses a combination of light and magnetic fields. Light provides a dissipative force that causes atoms to slow down while a magnetic field gradient tailors this force so that it also provides spatial confinement.

When a pair of close-to-resonance, counter-propagating laser beams having wave-number  $k$  are overlapped with an atom with velocity  $v$ , a so-called “molasses”

**Figure 3.1:** Magneto-optical trap.

force is exerted on it. This force can be calculated using Equation 2.4, resulting in

$$\begin{aligned}
 F_{\text{mol}}(\delta) &= F_{\text{rad}}(\delta - kv) - F_{\text{rad}}(\delta + kv) \\
 &\approx F_{\text{rad}}(\delta) - kv \frac{dF_{\text{rad}}}{d\delta}(\delta) - F_{\text{rad}}(\delta) - kv \frac{dF_{\text{rad}}}{d\delta}(\delta) \\
 &= -2k \underbrace{\frac{dF_{\text{rad}}}{d\delta}(\delta)}_{\gamma(\delta)} v = -\gamma(\delta)v.
 \end{aligned} \tag{3.3}$$

Here, an assumption of  $kv \ll \Gamma$  has been made when calculating the Taylor expansion of the radiation pressure force and a detuning-dependent function  $\gamma$  has been defined. The resulting force on the atom is an effective viscous friction with a detuning-dependent damping coefficient  $\gamma(\delta)$ . As long as  $\delta < 0$ , this constant will be positive and therefore, result in cooling.

Whilst the force from Equation 3.3 is responsible for the cooling, it does not provide the means for trapping the atoms. The spatial confinement is induced by a composite effect of the light and a magnetic field gradient. This is illustrated in Figure 3.1a for a simplified atom with a  $J = 0 \rightarrow J = 1$  transition. A magnetic field gradient along the  $x$  axis produces a spatially-varying energy shift of the different magnetic sub-levels. For this figure the quantisation axis is chosen to be aligned with the local magnetic field. Therefore, the Zeeman-shifted magnetic sub-state  $m_J = 1$  ( $m_J = -1$ ) is always above (below) the other excited states. Also, after  $\sigma^+$  polarised light crosses the zero of the magnetic field, it turns into  $\sigma^-$  and vice versa. For the MOT, the polarisation of the light is arranged such

that  $\sigma^+$  light always travels away from the magnetic zero while  $\sigma^-$  travels towards it.

When a ground state atom moves away from the centre of the trap, the magnetic field will cause the  $|J = 0, m_J = 0\rangle \rightarrow |J = 1, m_J = -1\rangle$  transition to become resonant. However, only  $\sigma^-$  polarised light can drive this transition. Therefore, as long as  $\omega < \omega_0$ , it is always pushed inwards.

The total force affecting the atoms in the MOT can be obtained through a similar argument as the one from Equation 3.3 as follows

$$\begin{aligned} F_{\text{MOT}}(\delta) &= F_{\text{rad}}(\delta - kv - \beta x) - F_{\text{rad}}(\delta + kv + \beta x) \\ &\approx -2(kv + \beta z) \frac{dF_{\text{rad}}}{d\delta}(\delta) = -\gamma v - \frac{\gamma\beta}{k}x, \end{aligned}$$

where  $\beta = (\mu/\hbar) \frac{dB}{dx}$  and  $\mu$  is the magnetic moment of the transition.

Figure 3.1b shows the full arrangement necessary to produce a MOT in 3D space. Magnetic coils carry current in opposite directions to create a quadrupole field which has a gradient along each axis. Three pairs of counter-propagating light beams are aligned to give confinement and cooling for all spatial degrees of freedom.

### 3.2.1 Laser Cooling Limits

The MOT's working principle is based on the radiation pressure force which is a time-averaged effective force resulting from many absorption-emission events. If an atom at its centre is slow enough, absorption from any of the beams is equally likely. Also, heating occurs both from absorption and emission as a result of photon recoil. To quantify the heating due to these processes, an atom moving along one dimension within two opposing light beams is considered [45, 55]. In this situation, the radiation pressure force of the two beams cancels out while the fluctuations, in contrast, are cumulative. An atom with momentum  $\mathbf{p}$  and kinetic energy  $\frac{p^2}{2m}$  can absorb a photon with momentum  $\hbar\mathbf{k}$ . The kinetic energy of the atom after absorption is

$$E = \frac{|\mathbf{p} \pm \hbar\mathbf{k}|^2}{2m} = \frac{p^2}{2m} + \frac{\hbar^2 k^2}{2m} \pm 2\frac{p\hbar k}{2m},$$

where the sign depends on whether a photon from the right or left beam has been absorbed. On average, the kinetic energy of the atom increases by one recoil

energy  $E_r = \frac{\hbar^2 k^2}{2m}$  in each absorption process. Likewise, when the atom decays and emits the photon, it gets a recoil kick that, on average, increases the energy again by  $E_r$ . Due to both processes, the kinetic energy of the atom increases by  $2E_r$ . The rate of absorption-emission events is given by Equation 2.3 written here as  $R_{\text{sc}} = \Gamma \rho_{ee}$  for a single beam of light. If the intensity is much smaller than the saturation intensity, then the scattering rate for both beams is  $2R_{\text{sc}}$ . Therefore, the rate at which the atoms get heated up is

$$\frac{dE_{\text{heat}}}{dt} = (2R_{\text{sc}})(2E_r).$$

The rate at which the kinetic energy changes as a result of an applied force is  $\frac{dE}{dt} = F \cdot v$ . In particular, for the cooling force from Equation 3.3

$$\frac{dE_{\text{cool}}}{dt} = -\gamma v^2.$$

A steady state is reached when heating and cooling compensate each other and this sets the temperature limit achievable by Doppler cooling. The equilibrium velocity is determined by

$$\frac{dE_{\text{total}}}{dt} = \frac{dE_{\text{cool}}}{dt} + \frac{dE_{\text{heat}}}{dt} = 0 \quad \Rightarrow \quad v_{eq}^2 = \frac{4E_r R_{\text{sc}}}{\gamma}.$$

Using that  $\gamma = 2\hbar k^2 \frac{-2\delta}{\delta^2 + \Gamma^2/4} R_{\text{sc}}$ , the equilibrium temperature  $T$  is

$$k_B T = mv_{eq}^2 = \frac{\hbar \Gamma}{4} \left( \frac{2|\delta|}{\Gamma} + \frac{\Gamma}{2|\delta|} \right).$$

The absolute minimum of temperature achievable by Doppler cooling  $T_D$  is called the Doppler temperature. It is reached when  $\delta = -\Gamma/2$  and is given by

$$T_D = \frac{\hbar \Gamma}{2k_B}. \quad (3.4)$$

The Doppler temperatures corresponding to lithium-6 and caesium-133 are  $T_D^{\text{Li}} = 141 \mu\text{K}$  and  $T_D^{\text{Cs}} = 126 \mu\text{K}$  respectively.

A significantly lower temperature can be achieved with caesium due to another cooling mechanism which does not rely on spontaneous emission and therefore, is not Doppler-limited. This cooling mechanism requires counter-propagating circularly polarised light as with the MOT with the difference that the magnetic

field gradient should be switched off, and is referred to as  $\sigma^+ - \sigma^-$  cooling [56, 57]. The counter-propagating, circularly polarised light creates a linearly polarised wave that has an oscillation axis that rotates along the propagation direction forming a helix. This arrangement produces a motion-induced imbalance of population among the hyperfine states. Which, in turn, results in an enhanced absorption of light from the beam that propagates in the direction opposite to the motion. Thus, an effective friction force emerges from this process that results in lowering the temperature of the atoms. For this mechanism to work, the detuning must be large compared to the excited state's linewidth so that the separation between the dressed state levels is larger than their corresponding linewidth. In this experiment, temperatures as low as  $16\text{ }\mu\text{K}$  are obtained with caesium at this stage of an experimental run.

For lithium, the excited  ${}^2P_{3/2}$  levels overlap (see Figure 2.1), which prevents sub-Doppler cooling mechanisms from working [58]. Moreover, this overlap results in a broader effective linewidth for the cooling transition which further restricts the lowest achievable temperature through laser cooling which, on this experiment, was  $600\text{ }\mu\text{K}$ .

### 3.3 Dipole Trap

To overcome the phase-space density limitations of the MOT, resulting from the coarse nature of the momentum changes during absorption-emission processes, a conservative trap is necessary. In such a trap, evaporative cooling (see Section 3.4) can be implemented which does not suffer from this limitation.

The dipole potential from Equation 2.5, reproduced here

$$V_{\text{dip}}(r) = \frac{\hbar\Gamma^2}{8\delta} \frac{I(r)}{I_{\text{sat}}}, \quad (3.5)$$

is used to produce a conservative trap. However, simplifying the atom-light interaction to this potential is only valid when the detuning is high and, thus, the scattering rate

$$R_{\text{sc}} = \frac{\Gamma}{2} \frac{I/I_{\text{sat}}}{1 + (2\delta/\Gamma)^2 + I/I_{\text{sat}}}$$

is small compared to the duration of the experiment.

It is evident from Equation 3.5 that if  $\delta < 0$ , atoms will be attracted to regions of high intensity and vice versa. For red-detuned ( $\delta < 0$ ) light, a trap can be

created by concentrating the light in a focus or by crossing multiple beams. In such traps, when the harmonic approximation can be made, the trap frequency  $\omega_{\text{tr}}$  will depend on the total light power  $P$  with a relation  $\omega_{\text{tr}} \propto \sqrt{P}$ .

### 3.4 Evaporative Cooling

In most experiments with ultracold atoms, evaporative cooling is the final stage necessary to reach quantum degeneracy<sup>1</sup>. The basic idea behind it is to allow a few particles to acquire a significant fraction of the energy and then selectively remove them from the ensemble. For this process to lead to a degenerate quantum gas, the removal of energy should be faster than the loss of atoms. Thus, it is necessary to understand the rate and scaling factors of this process.

In a potential with a finite depth, atoms would not strictly equilibrate to a thermal distribution since, in equilibrium, there would be no atoms in the trap. However, if the average energy per particle is much lower than the trap depth  $U_0$  then, inter-atomic collisions shuffle the energy among them leading to a quasi-thermal distribution [60].

For an atom to leave the trap, it requires an energy greater than  $U_0$ , namely

$$U_0 + \epsilon k_B T$$

where the zero of energy is defined to be at the bottom of the trap and  $0 \leq \epsilon \leq 0$  is the fraction of thermal energy carried away by the atom. The probability for this to happen is given by the tail of the thermal distribution that extends beyond the trap depth. Defining the truncation parameter  $\eta = U_0/k_B T$ , the atom-loss rate is [60, 61]

$$\dot{N} = -N n_0 \sigma \bar{v} \eta e^{-\eta},$$

where  $n_0$  is the density,  $\sigma$  the atom-atom scattering cross-section and  $\bar{v}$  the mean relative velocity of the atoms in the trap. This equation relates the evaporation rate with the scattering cross-section which, by means of a Feshbach resonance (see Section 2.5), can be used to optimise the evaporation process.

The rate of change of the total energy of the trapped gas is found to be

$$\dot{E} = \dot{N} (U_0 + \epsilon k_B T), \quad (3.6)$$

---

<sup>1</sup>A strontium BEC has been created exclusively using laser cooling [59].

where the fraction of energy carried out can be found to be  $\epsilon = \frac{\eta-5}{\eta-4}$  for the case of a harmonic trap with energy-independent scattering cross-section[60].

As evaporation progresses, the temperature decreases and, since  $\dot{N} \propto e^{-\eta}$ , the evaporation rate decreases as well and eventually reaches stagnation. It is therefore desirable to follow the decrease in temperature with a decrease in trap depth so that evaporation can continue. For this purpose, a time dependent potential is considered [62]

$$U(x, t) = -U(t)g(x),$$

where  $U(t)$  contains the temporal dependence and  $g(x)$  describes the trap shape ( $g(0) = 1$ ). In this case, Equation 3.6 is no longer valid because the change in the potential would also affect the total energy. Using the virial theorem, a relation between the total energy  $E$  and the average potential energy  $\langle U \rangle$  is found for a harmonic trap

$$\langle U \rangle = \frac{E}{2}.$$

If the potential decreases at a rate  $\dot{U}$ , the relative decrease is  $\dot{U}/U$ . The change in energy due to this is then  $\frac{\dot{U}}{U} \frac{E}{2}$ . Therefore, including this term into Equation 3.6, the total rate of change of the energy of the gas is

$$\dot{E} = \dot{N}(U_0 + \epsilon k_B T) + \frac{\dot{U}}{U} \frac{E}{2}. \quad (3.7)$$

For a fixed value of  $\eta$ , the solution to Equation 3.7 is

$$\frac{N}{N_i} = \left( \frac{U}{U_i} \right)^{\frac{3}{2(\eta+\epsilon-3)}}, \quad (3.8)$$

where  $N_i$  and  $U_i$  are the initial number of atoms and trap depth respectively. However, the most relevant quantity is the phase-space density (PSD) which, for a harmonic trap, is  $\rho = N \left( \frac{\hbar\omega}{k_B T} \right)^3$ . The scaling of this quantity can be calculated by substitution in Equation 3.8 resulting in

$$\frac{\rho}{\rho_i} = \left( \frac{U_i}{U} \right)^{\frac{3(\eta+\epsilon-4)}{2(\eta+\epsilon-3)}} = \left( \frac{N_i}{N} \right)^{\eta+\epsilon-4}.$$

As long as  $\eta + \epsilon > 4$ , a decrease in atom number would lead to increase in PSD. For example, with a truncation parameter  $\eta = 7$  and an initial PSD of 0.0004,

a decrease in trap depth by a factor of 800 would result in a decrease in atom number by a factor of 8.5 and a PSD of 1. In the experiment, with an initial PSD of 0.0004, a decrease in trap depth by a factor of  $10^3$  results in a decrease in atom number by a factor of 10 and a PSD close to 1.

The treatment thus far has neglected two important features, namely, the increase in evaporation rate due to the energy dependence of the scattering cross-section and the loss of atoms caused by collisions with the background gas. With a cross-section that does not depend on energy, the runaway evaporation regime, where the collision rate increases as evaporation progresses, cannot be achieved with optical traps [61]. In contrast, in the unitarity limit where  $\sigma = 4\pi/k^2$ , the cross-section increases as the evaporation process decreases the average kinetic energy in the trap. In this case runaway evaporation can be achieved [63].

If atomic losses were not present, the most efficient evaporative cooling would consist in maintaining the trap depth high compared to the average energy per particle, and waiting a long enough time until a single atom attains all of the energy of the ensemble and carries it away when leaving the trap. However, this may not be practical since a “long enough time” may be longer than the age of the universe. Furthermore, this method is not realistic, since atomic losses limit the maximum time the atoms may remain in the trap.

Atomic losses, caused by collisions with the background gas, can be considered by including a loss rate  $\Gamma_{bg}$  and making the replacement  $\dot{N} = \dot{N}_{evap} - \Gamma_{bg}N$  in the previous equations, where  $\dot{N}_{evap}$  is the atom loss rate caused only by evaporation. It can be shown that the scaling laws for the number and phase-space density versus trap-depth are reduced by a factor  $\exp(-\Gamma_{bg}t)$ , where  $t$  is the time over which the trap is lowered [62].

## 3.5 Imaging

Optical imaging is the most important tool for examining the atomic cloud. This makes it possible to state-selectively measure the density profile of the cloud. Additionally, by analysing the time dependence of the cloud’s density during free fall, the temperature can be determined as described in Subsection 3.5.1.

When probing an atomic cloud with light [64], the effect that atoms have on the light can be described by the complex index of refraction  $n_{ref} = n_r + in_i$ . The real part  $n_r$  contains information about the phase shift of the light caused by the atoms while the imaginary part  $n_i$  accounts light absorption. The amplitude of

an electric field propagating through a medium characterised by  $n_{\text{ref}}$  is

$$\mathbf{E}(z, t) = \text{Re} \{ \mathbf{E}_0 e^{i(kz - \omega t)} \} = \text{Re} \{ \mathbf{E}_0 e^{i(k_0 z(n_r + i n_i) - \omega t)} \} = e^{-k_0 n_i z} \text{Re} \{ \mathbf{E}_0 e^{i(k_0 z n_r - \omega t)} \},$$

where  $k_0$  and  $k$  are its wave numbers in vacuum and through the medium respectively. An intensity absorption coefficient  $a$  may be defined as  $a = 2k_0 n_i$  such that the intensity through the medium satisfies

$$\frac{dI}{dz} = -aI. \quad (3.9)$$

In this work, imaging is carried out exploiting the imaginary part of  $n_{\text{ref}}$  by measuring the amount of absorbed light to quantify the density profile. The real part could also be used by performing phase contrast imaging; this can provide a way to measure the cloud's properties non-destructively [65]. The index of refraction will depend on the density of the atomic cloud, the frequency of the probe light as well as the internal state of the atoms. Understanding this relation is essential for extracting the sought-after information from the images.

The refractive index is determined by the medium's relative permittivity  $\epsilon_r$  and permeability  $\mu_r$  by  $n_{\text{ref}} = \sqrt{\epsilon_r \mu_r}$ . For the case of an atomic cloud,  $\mu_r$  is very close to one at optical frequencies and therefore  $n_{\text{ref}} \approx \sqrt{\epsilon_r} = \sqrt{1 + \chi_e}$  with  $\chi_e$  being the electric susceptibility. The polarisation density  $\mathbf{P}$  defines the susceptibility by  $\mathbf{P}^+ = \epsilon_0 \chi_e \mathbf{E}^+$  and the superscript + indicates that it is the positive-rotating component. On the other hand,  $\mathbf{P}$  is related to the electric dipole moment of the atoms that constitute the medium through the number density  $n$  by the relation  $\mathbf{P} = n\mathbf{d}$ . Finally, the dependence of the dipole moment on the electric field of the probe is contained in the polarisability  $\alpha$ , which was calculated before and is given by Equation 2.2 reproduced here

$$\alpha = i \frac{c \epsilon_0 \hbar \Gamma}{2 I_{\text{sat}}} \frac{1 + i 2 \delta / \Gamma}{1 + (2 \delta / \Gamma)^2 + I / I_{\text{sat}}}.$$

For a rarefied gas,  $|\chi_e| \ll 1$  so that

$$n_{\text{ref}} = \sqrt{1 + \chi_e} \approx 1 + \chi_e / 2 = 1 + n\alpha / 2\epsilon_0.$$

The absorption coefficient is then

$$a = 2k_0 \text{Im}\{1 + n\alpha/2\epsilon_0\} = \frac{n\hbar\omega_0\Gamma}{2I_{\text{sat}}} \frac{1}{1 + (2\delta/\Gamma)^2 + I/I_{\text{sat}}} = n\sigma_{\text{sc}},$$

where  $\sigma_{\text{sc}}$  is the photon-atom scattering cross-section defined as

$$\sigma_{\text{sc}} = \frac{\sigma_0}{1 + (2\delta/\Gamma)^2 + I/I_{\text{sat}}} \quad (3.10)$$

and  $\sigma_0$  is the on-resonance ( $\delta = 0$ ), small-signal ( $I \ll I_{\text{sat}}$ ) cross-section

$$\sigma_0 = \frac{\hbar\omega_0\Gamma}{2I_{\text{sat}}} \quad (3.11)$$

In general, the density is a function of the spatial coordinates. This dependence produces a spatially varying absorption which, in turn, results in an intensity profile which is measured and used to infer the density distribution. If the intensity of the incoming light  $I_{\text{in}}$  satisfies  $I_{\text{in}}/I_{\text{sat}} \ll 1$ , Equation 3.9 can easily be integrated and the intensity of the probe light after passing through the atomic cloud is

$$I_{\text{out}}(x, y) = I_{\text{in}}(x, y)e^{-n_z(x, y)\sigma_{\text{sc}}} \quad \text{where} \quad n_z(x, y) = \int_{\text{extent of cloud}} n(x, y, z) dz.$$

Therefore, the column density is given by

$$n_z = -\frac{1}{\sigma_{\text{sc}}} \ln \frac{I_{\text{out}}}{I_{\text{in}}}.$$

The total atom number  $N$  can be calculated according to

$$N = \int n_z(x, y) dx dy.$$

Details of the practical implementation of this technique can be found in Section 4.8.

### 3.5.1 Measuring the Temperature

The temperature of a trapped atomic cloud can be measured by releasing and imaging it after it has fallen for typically a few milliseconds. This process is repeated for several realisations of the experiment with different falling times.

Under the assumption that during the measurement all samples start with the same conditions, the temperature can be measured by looking at how the cloud expands. The assumption of all clouds starting with the same initial conditions can be verified by observing the behaviour of multiple repetitions at equal times of flight.

Regarding their external degrees of freedom, atoms behave classically for the majority of the cooling process. This means that they can be described using a Maxwell-Boltzmann distribution

$$f(\mathbf{r}, \mathbf{p}) \sim e^{-E(\mathbf{r}, \mathbf{p})/k_B T}, \quad (3.12)$$

where  $f$  is the probability per unit phase-space volume of finding a particle at  $(\mathbf{r}, \mathbf{p})$ . Approximating the trap as a harmonic confinement with frequency  $\omega$ , the energy becomes<sup>2</sup>

$$E(\mathbf{r}, \mathbf{p}) = \frac{1}{2}m\omega^2 r^2 + \frac{1}{2m}p^2. \quad (3.13)$$

The normalised probability distribution inside the trap is

$$f(\mathbf{r}, \mathbf{p}) = \frac{1}{(2\pi\sigma_r^2)^{3/2}} e^{-\frac{r^2}{2\sigma_r^2}} \frac{1}{(2\pi\sigma_p^2)^{3/2}} e^{-\frac{p^2}{2\sigma_p^2}}, \quad (3.14)$$

where  $\sigma_r^2 = \frac{k_B T}{m\omega^2}$  and  $\sigma_p^2 = mk_B T$ . After the cloud has fallen for some time  $t$ , the particles move from  $\mathbf{r}$  to  $\mathbf{r}' = \mathbf{r} + \frac{\mathbf{p}}{m}t$  and the distribution becomes

$$f(\mathbf{r}', \mathbf{p}) = \frac{1}{(2\pi\sigma_r^2)^{3/2}} e^{-\frac{|\mathbf{r}' - \frac{\mathbf{p}}{m}t|^2}{2\sigma_r^2}} \frac{1}{(2\pi\sigma_p^2)^{3/2}} e^{-\frac{p^2}{2\sigma_p^2}}. \quad (3.15)$$

Integrating out the momentum dependence we find

$$f(\mathbf{r}') = \frac{1}{(2\pi\sigma_t)^{3/2}} e^{-\frac{r'^2}{2\sigma_t^2}}, \quad (3.16)$$

where  $\sigma_t = \sqrt{\frac{1}{m^2}t^2\sigma_p^2 + \sigma_r^2}$ . The result is also a normalised Gaussian with standard deviation  $\sigma_t$  which we can write as

$$\sigma_t^2 = t^2 \frac{k_B T}{m} + \sigma_r^2. \quad (3.17)$$

By measuring  $\sigma_t^2$  as a function of time, the coefficient for  $t^2$  can be determined

---

<sup>2</sup>Here we ignore gravity which if included, would only shift the position but not the shape.

and hence the temperature as well.

Figure 3.2 shows the result of a temperature measurement. Two-dimensional Gaussian functions are fitted to the density profile that result from the captured images. The fit provides the Gaussian's widths  $\sigma_x(t)$  and  $\sigma_y(t)$ , as a function of time of flight. Performing a linear regression of  $\sigma_x^2$  and  $\sigma_y^2$  as a function of  $t^2$ , the slope, which according to Equation 3.17 is  $k_B T/m$ , is calculated. From this slope the temperature can be readily obtained. The mismatch between the temperatures on the  $x$  and  $y$  axes may indicate that the atoms have not fully thermalised after being transferred into the dipole trap. Furthermore, in the longitudinal direction, the cloud has only expanded by 30% and, with a longer time of flight a more precise determination could be made. However, this becomes challenging because as the cloud expands the signal-to-noise ratio of the atomic density decreases.

After quantum degeneracy has been reached, the wings of the cloud still have a Gaussian shape and have the same behaviour as the classical gas described in this section. Therefore, the temperature may be determined by the same procedure as long as the analysis is restricted to the wings of the cloud.

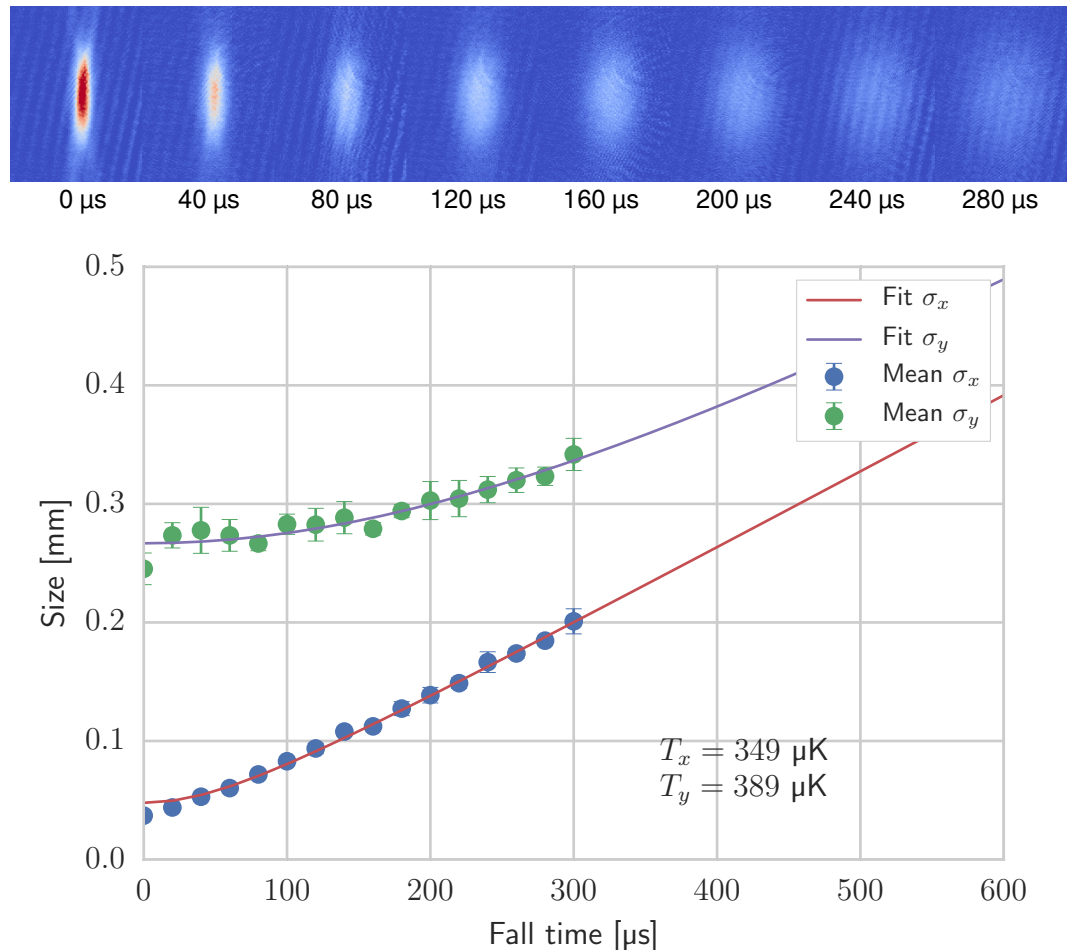


**Figure 3.2:** Temperature measurement of a lithium sample immediately after loading into the dipole trap. The strip of images (top) shows a sequence of absorption images captured at various times of flight indicated in each image. The resulting horizontal and vertical sizes of the cloud are plotted and fitted (bottom). The calculated temperature resulting from the measurements in each direction are displayed. The shown data is the average of three repetitions. Error bars represent the standard deviation out of three repetitions for each point.

## CHAPTER 4

# Experimental Apparatus

The system that has been built throughout this work encompasses a wide variety of technologies. Most notably, ultra-high vacuum, frequency stabilised lasers and high-power lasers. The experimental apparatus has been built on top of two independent optical tables. The first one contains all the lasers, optics and atomic reference cells to produce light at the required frequencies. This also includes shutters and modulators to control the intensity of the beams. This part of the setup is described in Section 4.1. The light from this table is coupled into several optical fibres to transfer it to the other table and facilitate alignment. The second optical table is mostly occupied by the vacuum chamber detailed in Section 4.2. This chamber has been equipped with coils that can generate high magnetic fields and gradients which are described in Section 4.3. The sections that follow, detail the parts of the experimental system which have been built to obtain (Section 4.4), trap and cool (sections 4.5, 4.6 and 4.7), and examine (Section 4.8) the atoms. A description of the computerised control system, needed to coordinate the operation of all the different parts of the apparatus is found in Section 4.9. In the last section of this chapter, an outlook of work to follow is discussed.

## 4.1 Laser System

The realisation of laser cooling requires precise control of the frequency and amplitude of several different laser beams. The light is produced by external cavity diode lasers (ECDLs), where the frequency of the output light is controlled by varying the length of the cavity using a piezo-electric crystal. The frequency is further adjusted by means of acousto-optical modulators (AOMs). Moreover, AOMs, together with mechanical shutters, are used to control the amplitude of

the various light beams. The techniques used to obtain the required frequencies are described in Subsection 4.1.1. The different nature of the lithium and caesium atoms demands different approaches in the optical setup of each of them. Thus, each system is described separately in subsections 4.1.2 and 4.1.3 respectively. Lastly, the lasers used to produce far-of-resonance optical dipole traps are described in Subsection 4.1.4. The laser systems have been described in detail in [36] and [37], and only a short overview is given here.

### 4.1.1 Frequency Stabilisation

The transition linewidth for both lithium and caesium is about 5 MHz. This sets the scale of the requirement of stability and linewidth from the lasers. To achieve the necessary linewidth, diode lasers are equipped with a holographic grating that creates an external cavity. This external cavity reduces the emission linewidth below 600 kHz [66]. However, not only does the laser linewidth need to be below the atomic linewidth but it is also necessary to avoid drifts in the absolute value of the frequency to ensure a reliable operation of the experiment. In order to fulfil the stability requirements, active stabilisation of the frequency is necessary. Using the absorption of light passing through a vapour cell filled with either lithium or caesium as a reference, the frequency of the lasers can be fixed as is described in Subsection 4.1.1.1. Once a laser has been fixed to a given frequency, this can be used as a reference such that other lasers can be compared to it. In this manner, the frequency of the second laser can be anchored relative to the reference laser. This technique is described in Subsection 4.1.1.2.

#### 4.1.1.1 Doppler-free Saturated Absorption Spectroscopy

A straightforward way of ensuring that a laser emits light with the frequency of an atomic transition, is to use the atoms themselves as a reference [45]. As light travels through a sample of atoms at rest, it will be scattered depending on its frequency. By measuring the light transmission as a function of frequency, the spectrum of the atoms can be found. However, at the temperature necessary to have enough vapour pressure to practically perform spectroscopy, the motion of the atoms at velocity  $v$  produces a Doppler shift in their resonance frequency  $\omega_0$  with respect to the lab frame given by  $\delta_D = \omega_0 v/c$ . Since atoms in a thermal gas have a distribution of velocities, there is a distribution of Doppler shifts. As a consequence, the transitions are widened and the sought-after details are washed

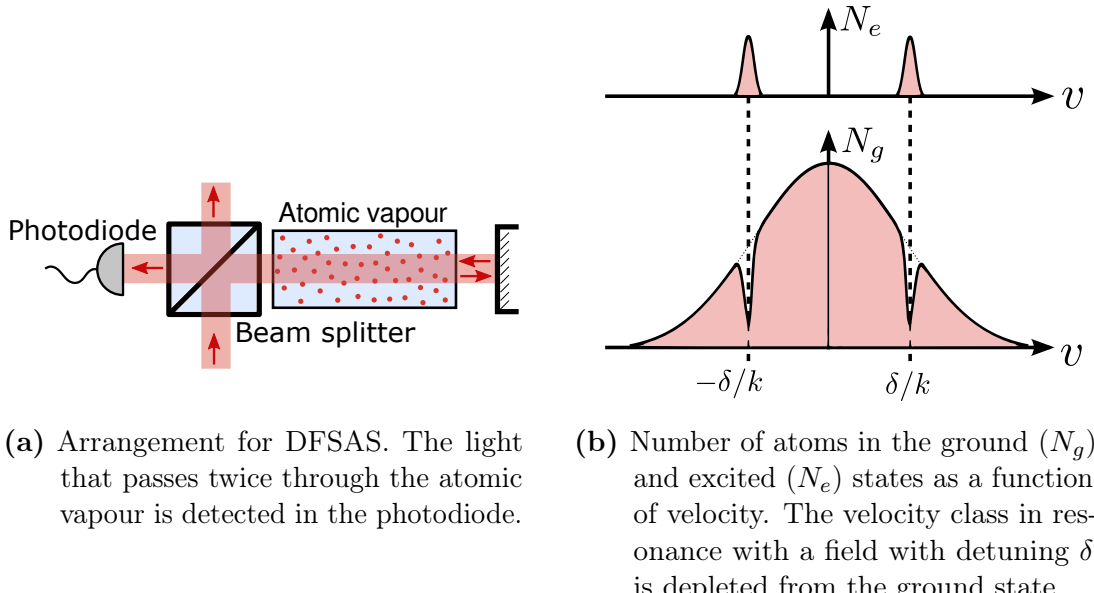


**Figure 4.1:** Doppler-free saturated absorption spectroscopy.

out. It is for this reason that using Doppler-free saturated absorption spectroscopy (DFSAS) is necessary.

The setup used in this work to perform DFSAS is illustrated in Figure 4.1a. A beam of light is made to travel twice through an atomic vapour cell and the transmitted light is measured in a photodiode. Its principle of operation can easily be explained considering two-level atoms, as shown in Figure 4.1b, driven by light with wave vector  $\mathbf{k}$  and detuning  $\delta = \omega - \omega_0$ . As light first traverses the vapour cell, atoms which have a velocity  $\mathbf{v}$  that satisfies  $\delta = \mathbf{k} \cdot \mathbf{v}$  will absorb and then scatter light. This process promotes atoms with velocity  $\mathbf{v}$  from the ground state to the excited state. Similarly, the returning beam has a wave vector  $-\mathbf{k}$  and atoms, with a velocity that satisfies  $\delta = -\mathbf{k} \cdot \mathbf{v}$ , will again scatter light. In each of these paths, light is lost from the original beam through scattering. However, in the case of  $\delta = 0$ , both  $\mathbf{k}$  and  $-\mathbf{k}$  beams address the same velocity class of atoms. Namely, those with velocity orthogonal to  $\mathbf{k}$ . In this case, since the first beam excites some of the atoms, the returning beam encounters fewer scatterers. In this manner, when the light is on resonance, there is a peak in the transmission versus frequency signal. It is worth noting that the width of this feature will depend only on the linewidths of the laser and the transition and is not affected by the Doppler broadening.

Once this spectroscopic signal is obtained from the photodiode, it can be used to fix the frequency of the laser to one of the peaks of the spectroscopy. For this

purpose, the output of the photodiode is fed into a lock-in amplifier to produce a signal which is the derivative of the original spectroscopy signal. The peaks in the spectroscopy become zero-crossings of the derivative. The derivative signal can then be used as an error signal for a proportional-integral-derivative (PID) feedback loop that can keep the frequency of the laser constant.

#### 4.1.1.2 Offset Lock

With the frequency of a laser fixed using DFSAS (reference laser), a secondary laser (slave laser) can be anchored with respect to the first one using an *offset lock* [67]. One specific task of this thesis was to produce offset locks capable of achieving large detunings necessary in the cooling process as well as for imaging in high magnetic fields. This type of lock fixes the frequency difference between the reference and slave lasers to a value set by a voltage-controlled oscillator (VCO). Thus, changing the voltage of the VCO changes its frequency and consequently, the frequency difference between the reference and slave laser is changed. This provides a straightforward way of adjusting the frequency of the slave laser via a computer control system during experimental runs. Broadly, an offset lock works by first measuring the frequency difference using a photodiode and afterwards producing a DC voltage signal that only depends on this difference. This is achieved by measuring the phase accumulated by the oscillatory signal while travelling through an interferometer. For an interferometer arm of fixed length, the phase accumulated is proportional to the frequency. This signal, that only depends on the frequency difference between the two lasers is then used as an error signal and fed into a PID feedback loop to keep it at a fixed value.

An offset lock is composed of a reference laser with angular frequency  $\omega_{\text{ref}}$  which is overlapped, on a photodiode, with a slave laser with angular frequency  $\omega_{\text{sl}}$ . It is important that not only both beams are well overlapped on the photodiode but also that they are parallel to each other so that the interference varies only in time and not in space along the sensitive area of the photodiode. The result of superimposing both beams can be understood using the trigonometric identity

$$\cos \omega_{\text{ref}} t + \cos \omega_{\text{sl}} t = 2 \cos \left( \frac{\omega_{\text{ref}} + \omega_{\text{sl}}}{2} t \right) \cos \left( \frac{\omega_{\text{ref}} - \omega_{\text{sl}}}{2} t \right).$$

That is, the superposition of two electric fields that oscillate at frequencies  $\omega_{\text{ref}}$  and  $\omega_{\text{sl}}$  can be also understood as an electric field that oscillates with frequency

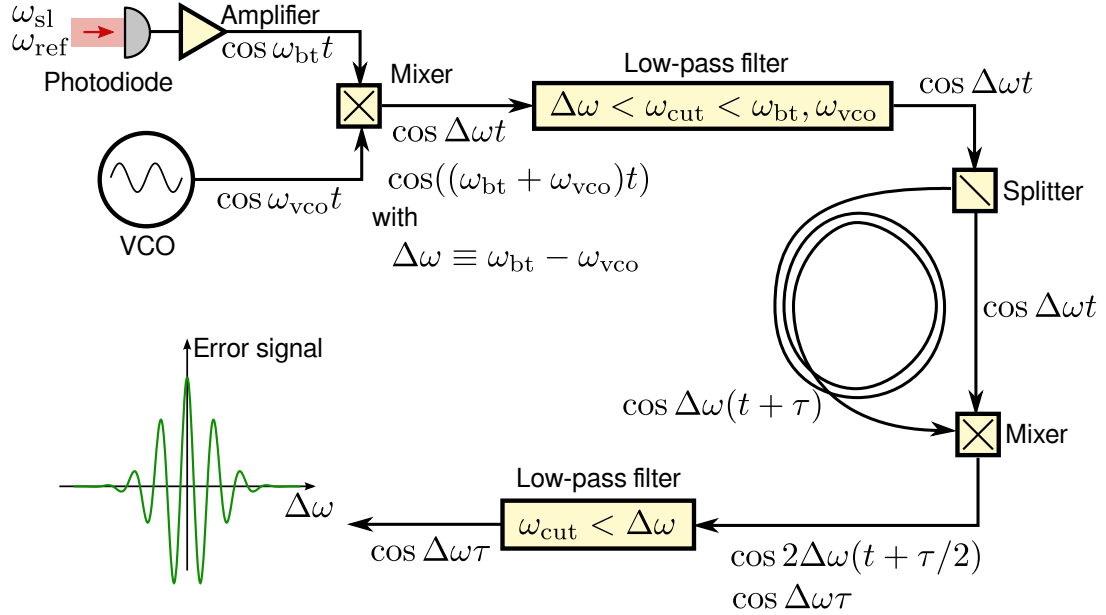


**Figure 4.2:** Schematic of error signal generation for an offset lock.

$(\omega_{\text{ref}} + \omega_{\text{sl}})/2$  modulated with a frequency  $(\omega_{\text{ref}} - \omega_{\text{sl}})/2$ . However, a photodiode measures not the amplitude of the field but the intensity which oscillates with double the frequency, namely  $\omega_{\text{ref}} + \omega_{\text{sl}}$  and  $\omega_{\text{ref}} - \omega_{\text{sl}}$ . Furthermore, the bandwidth of a photodiode is limited to a few gigahertz and the  $\omega_{\text{ref}} + \omega_{\text{sl}}$  frequency is in the range of hundreds of terahertz so this oscillation is averaged out and only the beat frequency  $\omega_{\text{bt}} := \omega_{\text{ref}} - \omega_{\text{sl}}$  signal is measured.

The purpose of the next stage of the lock is to generate a signal which depends on  $\omega_{\text{bt}}$  but is constant in time and can be used as an error signal for the feedback to the slave laser. This is achieved using a radio-frequency interferometer as shown in Figure 4.2. The photodiode beat signal of frequency  $\omega_{\text{bt}}$  is mixed (multiplied) with the output from a VCO, which is a sine wave generator whose frequency  $\omega_{\text{vco}}$  is proportional to an externally applied voltage. According to the trigonometric identity

$$\cos \theta \cos \phi = \frac{\cos(\theta - \phi) + \cos(\theta + \phi)}{2}, \quad (4.1)$$

the result of mixing the two signals, is a wave of frequency  $\omega_{\text{bt}} + \omega_{\text{vco}}$  superimposed with one of frequency  $\Delta\omega := \omega_{\text{bt}} - \omega_{\text{vco}}$ . In practice, RF wave mixers are not perfect and, additionally to the product of the waves, terms with the original frequencies are obtained. The signal of interest is the one with frequency  $\Delta\omega$  and therefore, a low-pass filter is used to remove all other components. Afterwards,

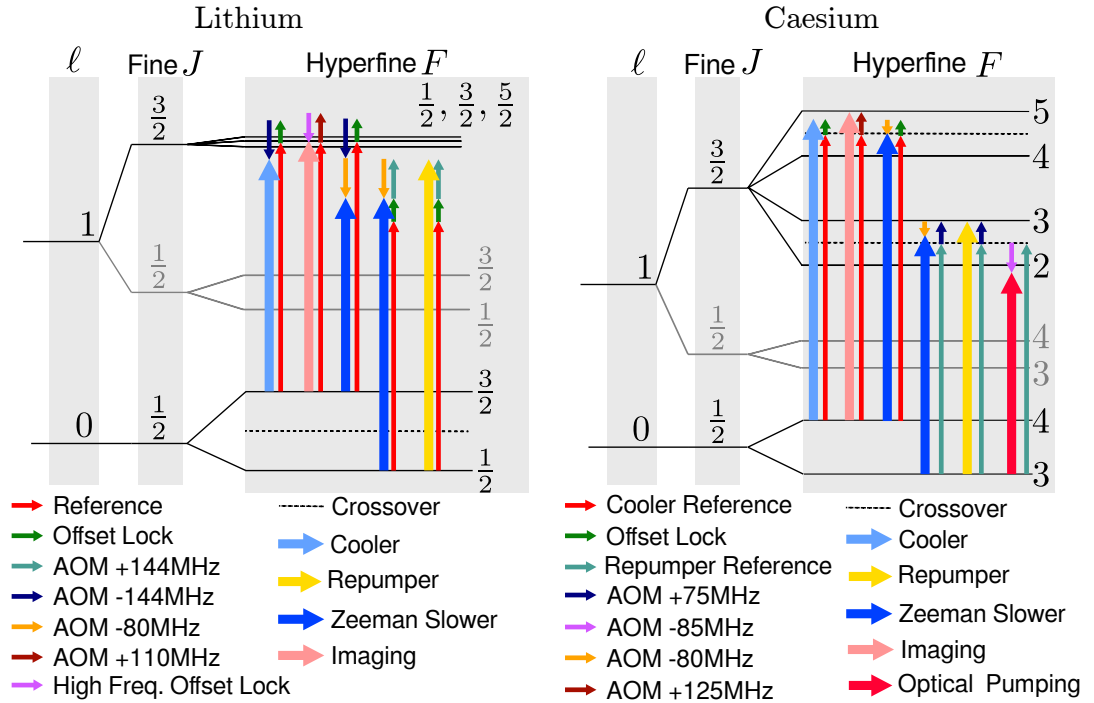


**Figure 4.3:** Generation of frequencies used in the experiment. Thin arrows add up to obtain the frequencies represented by the thick ones.

the signal is split and then propagated through an interferometer with two arms of different lengths. A delay  $\tau$  is accumulated by the signal travelling through the longest path after which both signals are mixed a second time. Once again, we get four frequency components after the mix, however, this time there is a DC component that depends on  $\tau\Delta\omega$ . Filtering out all the AC components we obtain the desired error signal only dependent on  $\tau\Delta\omega$ , which can be used to measure  $\Delta\omega$ . When feeding the error signal to a PID loop we ensure that  $\Delta\omega$  stays constant, thus, changing the frequency of the VCO produces a change in  $\Delta\omega$  which translates into a change in  $\omega_{bt}$  and therefore in  $\omega_{sl}$ .

The offset locks in this experiment are implemented using off-the-shelf components from Mini-Circuits. They are used to stabilise the lasers for the lithium and caesium magneto-optical traps (MOTs) with VCO frequencies between 100 MHz and 200 MHz. For imaging lithium at high magnetic fields, a high frequency offset lock described in Section 4.8.1 is used. The parts used for the lower frequency locks are: ZX60-8008E-S+ amplifier, ZX05-1-S+ mixers, SLP-30+ for the first low-pass filter and ZX95-200-S+ voltage-controlled oscillator. An RC filter is used as the second low-pass filter and a T-piece splits the signal.

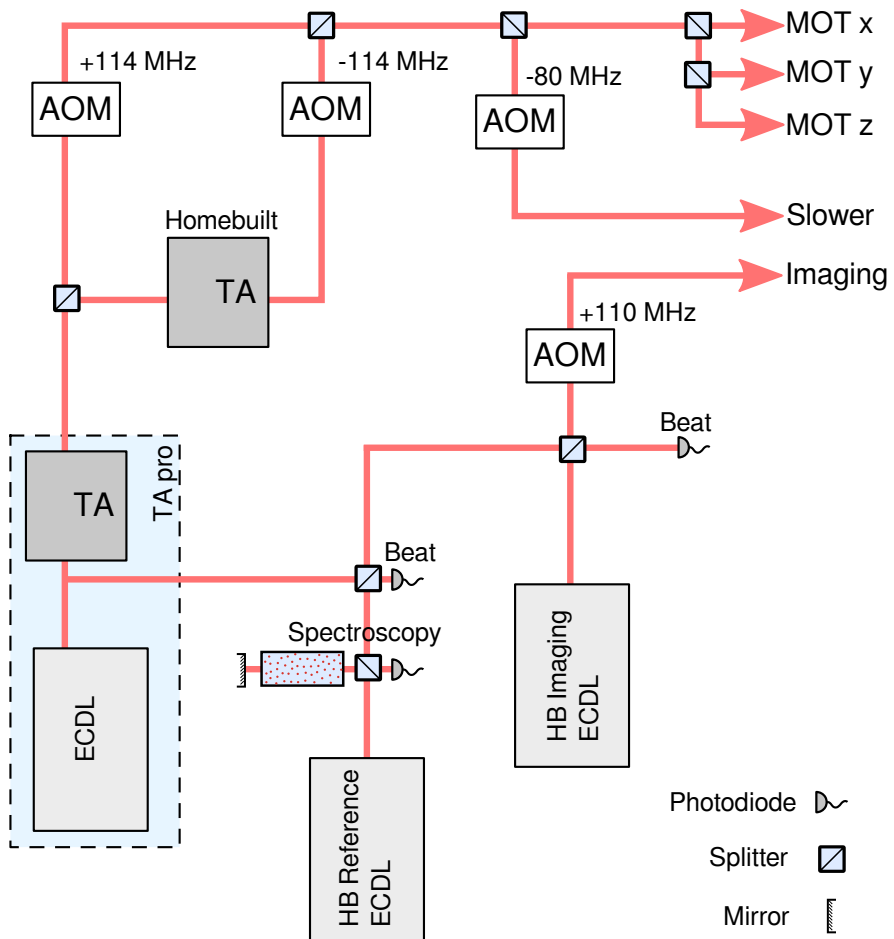


**Figure 4.4:** Schematic diagram of the laser setup for lithium.

### 4.1.2 Lithium Laser Setup

A vapour cell for lithium spectroscopy needs to be well designed and is more complex than for most alkali atoms. Because of its low vapour pressure at room temperature, lithium needs to be heated up to 640 K to practically do spectroscopy. Furthermore, lithium chemically reacts with glass so an evacuated glass cell, as used with caesium or rubidium, cannot be used. A heated, evacuated steel pipe containing a chunk of lithium is used. The pipe has glass windows at the ends. To prevent the lithium from reacting with the windows, the pipe is fitted with heat sinks to favour condensation on the pipe walls instead of on the windows. Secondly the pipe contains argon in order to reduce the mean free path of the lithium atoms. The setup of the spectroscopy cell is discussed with more detail in [36, Section 4.5.2].

Given the complexity presented by the spectroscopy cell, the lithium laser

Name	Role	Output Power [mW]
HB Reference	Used for spectroscopy to anchor the frequency of the other lasers.	12
HB Imaging	Exclusively used for absorption imaging at low and high magnetic fields.	8
Toptica TA pro (ECDL + TA)	Provides seed light for the homebuilt TA and re-pumping light for the MOT and Zeeman slower.	380
HB Tapered Amplifier	Generates the cooling light for the MOT and Zeeman slower.	300

**Table 4.1:** Homebuilt (HB) and commercial lasers used for cooling and trapping of lithium. Diodes for the HB tapered amplifier (TA) and the HB lasers are from eagleyard. The reported output power is measured after the necessary optical isolation.

system is based on a single laser referenced to the cell from which all other necessary frequencies are derived. The hyperfine splitting of lithium-6 is 228 MHz which allows that other required frequencies can be obtained by means of offset locks and AOMs.

However, since the  $2^2P_{3/2}$  states of lithium overlap, the cooling transition  $F = 3/2 \rightarrow F' = 5/2$  cannot be driven without also shuffling atoms into the  $F = 1/2$  ground state. As a consequence, it is necessary to drive the  $F = 1/2 \rightarrow F' = 3/2$  transition with almost as much power as the cooling light in order to keep the atoms in the absorption-emission cycle. This light is referred to as re-pumping light. Laser diode amplifiers that work at 670 nm are available up to a power of 500 mW. We use two amplifiers; one produces the cooling light and the other the re-pumping light.

In total, three different ECDLs together with two tapered amplifiers (TAs) are used to produce the necessary light as shown in Figure 4.4. The characteristics of these lasers are detailed in Table 4.1. The full scheme of frequencies used is illustrated in Figure 4.3. Using DFSAS the reference laser is locked to the crossover of the transitions from the  $F = 1/2$  and  $F = 3/2$  ground states to the overlapped D<sub>2</sub> excited states. The master ECDLs of the Toptica TA is offset locked with respect to the reference laser. The majority of the power out of the Toptica TA (340 mW) is used to produce the re-pumping light. The remaining fraction is used to seed the homebuilt TA from which the cooling light (300 mW) is produced. The output of each of the TAs passes through AOMs with a frequency of  $\pm 114$  MHz

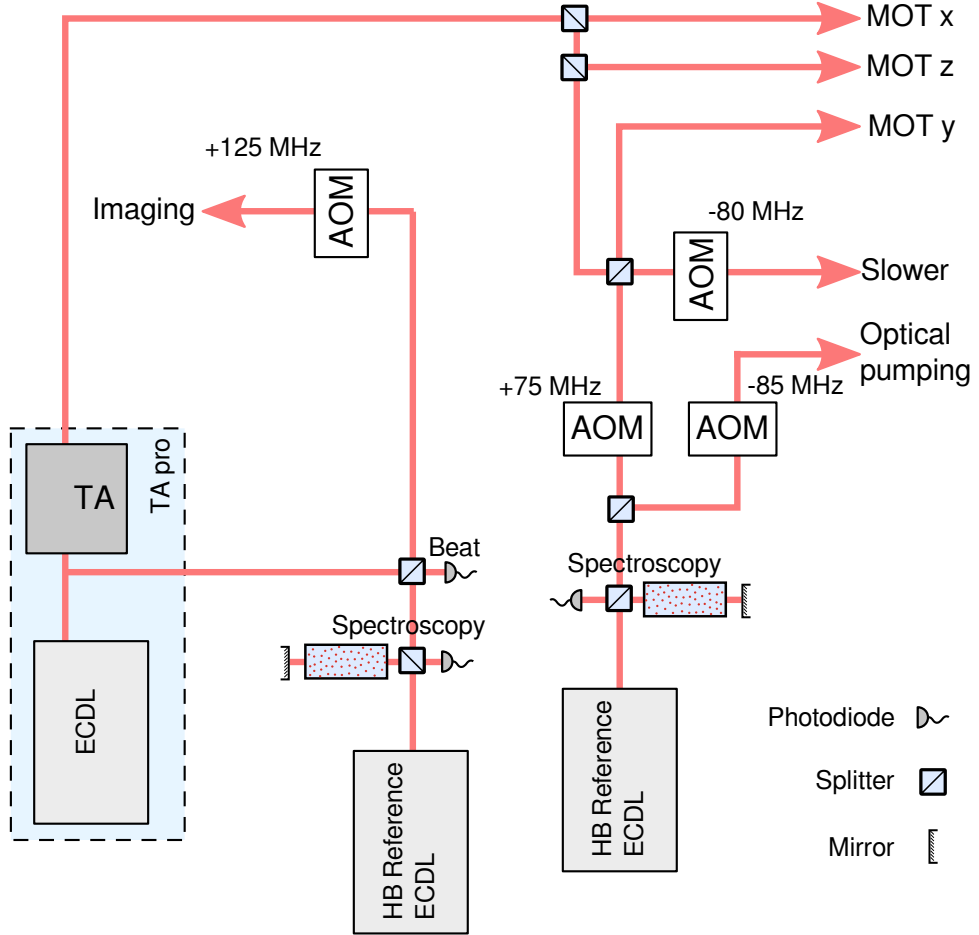


**Figure 4.5:** Schematic diagram of the laser setup for caesium.

so that they have a total frequency difference of 228 MHz corresponding to the hyperfine splitting of lithium. It should be noted that even though the frequency difference is fixed by the AOMs, the detuning with respect to the transition can be controlled with the offset lock for approximately 100 MHz limited by the lock's VCO.

A homebuilt imaging laser is also offset locked to the reference laser. The offset lock for this laser can achieve detunings of up to 1.3 GHz. See Section 4.8.1 for details.

### 4.1.3 Caesium Laser Setup

The overall structure of the caesium setup is similar to the one used for lithium with a reference laser to which the MOT cooling light is offset locked. However, the hyperfine splitting for caesium is  $\sim 9.2$  GHz which complicates obtaining

Name	Role	Output Power [mW]
HB Cooler Ref.	Used for anchoring the frequency of the cooling laser and for absorption imaging.	12
Toptica TA pro (ECDL + TA)	Provides cooling light for the MOT and Zeeman slower. Also used to produce Raman sideband cooling lattice (see Section 4.10.3 for details).	780
HB Repumper Ref.	Generates re-pumping light for the MOT and Zeeman slower as well as optical pumping.	8

**Table 4.2:** Homebuilt (HB) and commercial lasers used for cooling and trapping of caesium. The reported output power is measured after the necessary optical isolation.

cooling and re-pumping light from the same laser. Nonetheless, caesium gas reference cells are simple and readily available off the shelf from Thorlabs so it is straightforward to reference the two lasers separately. Moreover, the excited states are well separated compared to their linewidth so the probability of an atom falling out of the cooling cycle is low. This means that much less power is required for re-pumping the atoms as compared to the lithium system.

The caesium system, depicted in Figure 4.5, is composed of three ECDLs and one TA described in Table 4.2. A homebuilt reference laser is locked to the  $F = 4 \rightarrow F' = 4 \otimes 5$  crossover using DFSAS to which the master diode of the Toptica TA pro is offset locked. This reference laser is also used for imaging. A second homebuilt ECDL is locked to the  $F = 3 \rightarrow F' = 2 \otimes 3$  crossover and it is used to provide re-pumping power as well as optical-pumping light. The full scheme of frequencies used is depicted in Figure 4.3.

#### 4.1.4 Dipole Trap Lasers

The dipole trap consists of a narrow, high-power light beam overlapped with a wide lower power one (for details refer to Section 4.6). This composite beam is then crossed at the centre of the vacuum chamber. The narrow(wide) beam has a wavelength of 1070 nm(1064 nm) and a waist radius of 80  $\mu\text{m}$ (300  $\mu\text{m}$ ). The narrow beam is produced by a multi-mode 100 W IPG Yb fibre laser. The wide trap is produced by a 30 W Nufern amplifier which is seeded by a Mephisto S 200

single-mode laser from coherent. These lasers are detuned by several tens of terahertz, a factor of  $10^7$  of the transition's linewidth, with respect to the atomic transition so active stabilisation of the frequency is not necessary. More details of this setup such as how these lasers are being used and specifics about the traps created by them are found in Section 4.6.

## 4.2 Vacuum System

Laser cooling experiments need to take place in an ultra-high vacuum (UHV) environment. Otherwise, collisions with the background gas not only would heat the cooled atoms but will also eject them from the trap. This requirement implies that the experiments need to be carried out inside a vacuum chamber. However it is also necessary to have optical access and to be able to place optics and magnetic coils as close as possible to the atoms. For this purpose, a vacuum chamber as shown in Figure 4.6 is used. The chamber is divided into two sections by means of a differential pumping tube which allows to maintain a pressure of  $10^{-9}$  mbar in the oven section while keeping a pressure below  $10^{-11}$  mbar in the rest of the experimental chamber.

The pressure in the oven chamber is maintained by a titanium sublimation pump as well as a  $50 \text{ L s}^{-1}$  ion pump. This chamber contains an effusive oven of lithium as well as caesium dispensers. It also contains a mechanical feedthrough which allows to shut off the atomic flow into the experimental chamber by using an external stepper motor. Further details of this part of the chamber can be found in Section 4.4.

After passing through the differential pumping tube, atoms travel through the Zeeman slower to arrive into the main experimental chamber. This chamber has two recessed windows that facilitate the placement of magnetic coils at close proximity to the atoms. A cross section of this arrangement can be seen in Figure 4.8. The pressure in the experimental chamber is maintained by a titanium sublimation pump as well as a  $125 \text{ L s}^{-1}$  ion pump.

The pressure in the experimental chamber is measured with a vacuum gauge (Pfeiffer) to be below  $10^{-11}$  mbar. However, due to spatial restrictions this gauge is not directly on the chamber section where the experiments take place. However, an upper bound on the pressure in this chamber section may be obtained by measuring the lifetime of atoms inside a trap in the vacuum chamber. This estimate is obtained by first noting that the probability that a trapped atom

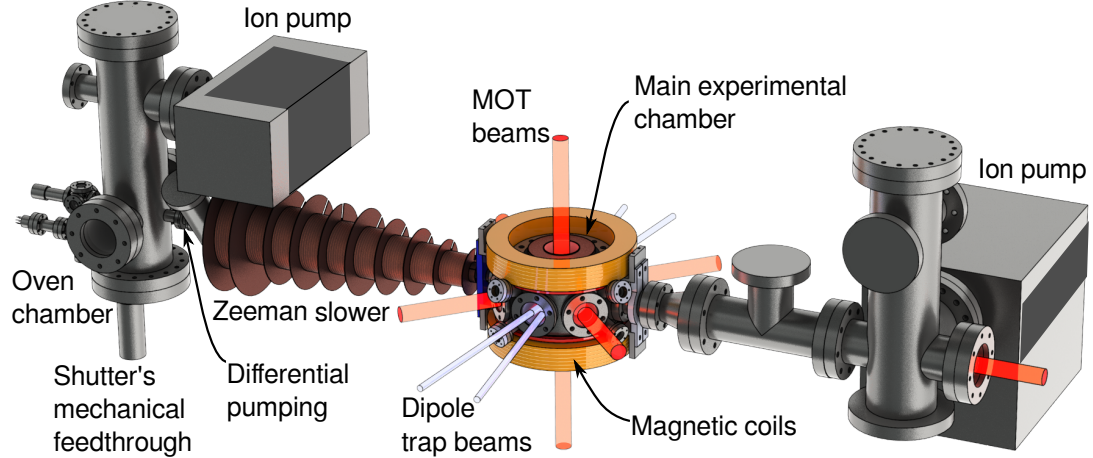


**Figure 4.6:** Overview of vacuum apparatus. See text for details.

collides with an atom from the background gas in the vacuum chamber is fixed by the pressure in the vacuum chamber. Hence, the probability of loosing an atom from the trap due to these collisions is proportional to the number of atoms in the trap. Another way of stating this is

$$\frac{dN}{dt} = -\gamma N,$$

with  $N$  the number of trapped atoms and  $\gamma$  the loss rate per atom. The solution is

$$N(t) = N_0 e^{-\gamma t}, \quad (4.2)$$

with  $N_0$  the initial atom number. The loss rate per atom is given by

$$\gamma = n_{bg} \bar{v}_{bg} \sigma,$$

where  $n_{bg}$  is the density of the background gas,  $\bar{v}_{bg}$  the mean velocity of the background gas and  $\sigma$  the collisional cross-section between a trapped atom and an atom from the background gas. Assuming that the background gas is mostly hydrogen molecules, at room temperature we get [8]

$$\gamma = 3.8 \times 10^3 \text{ s}^{-1} \frac{p_{bg}}{10 \times 10^{-10} \text{ mbar}} \frac{\sigma}{1 \text{ nm}^2}, \quad (4.3)$$

in which  $p_{bg}$  is the background pressure. The Li – H<sub>2</sub> collision cross section is

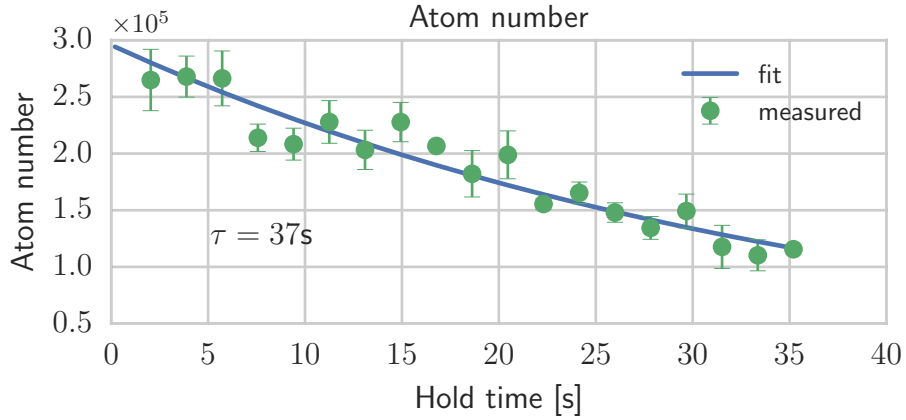


**Figure 4.7:** Decay of the number of lithium atoms in the dipole trap. A background magnetic field of 528 G is used to set the lithium-lithium scattering cross-section to zero. This measurement was carried out with a total dipole laser power of 3.6 W. The green data points show the average measured values out of three repetitions. Error bars represent the standard deviation. The blue continuous line indicates the exponentially decaying function that was fitted. Exponential decay indicates that the losses are one-body processes. The  $1/e$  lifetime provides an upper bound to the pressure in the vacuum chamber.

known to be  $2.39 \text{ nm}^2$  [68]. Thus, by measuring  $\gamma$  an upper bound for the pressure can be calculated. It is worth noting that this number is an upper bound because only losses caused by background-gas collisions have been considered in the model whilst ignoring losses such as photon absorption from the dipole trap light, plain evaporation, three-body recombination.

To measure the loss rate per atom, a fixed number of lithium atoms were loaded into an optical dipole trap and the number of remaining atoms were measured after various holding times. For this measurement, a magnetic field was used to set the lithium-lithium scattering cross-section to zero in order to avoid losses caused by elastic collisions. The result, shown in Figure 4.7, was then fitted with the exponential decay function presented in Equation 4.2 from which a  $1/e$  lifetime of  $\tau = 1/\gamma = 37\text{s}$  is obtained. With this value, an upper bound of  $2.9 \times 10^{-10} \text{ mbar}$  results for the pressure inside the main experimental chamber.

## 4.3 Magnetic Fields

Magnetic fields play an important role in the implementation of this experiment. They are used to produce an initial stream of cold atoms with a Zeeman slower, as part of a MOT to provide spatial confinement and to control the interactions between atoms by means of Feshbach resonances. In this section, the arrangement of magnetic fields for the last two cases will be detailed while the first one is detailed in Section 4.4. Additional to these coils, there is a set of six “offset” coils that produce weak homogeneous magnetic fields in the order of a few gauss which are used to compensate for earth’s magnetic field, for finely adjusting the position of the zero-field point, and to provide a quantisation axis during optical pumping.

The magnetic fields are produced for this experiment by passing an electrical current through various sets of coils. The arrangement of the coils is depicted in Figure 4.8. Kapton-insulated copper wire from S&W wire company with a  $5\text{ mm} \times 5\text{ mm}$  square cross section was used. This wire is hollow to allow for water cooling; the hole is round and has a diameter of 2.7 mm. All of the coils made using this wire have been wound using a back-winding technique which ensures that both leads are together and thus, the magnetic field produced by them cancels within a short distance. The water cooling allows the use of high currents, which for the Feshbach coils can be up to 400 A. In this way, fields of 1400 G can be produced at the position of the atoms.

### 4.3.1 Quadrupole Coils

The coils around the outer flange of the vertical windows carry currents in opposite directions, thus producing the magnetic field gradient necessary for the MOT. These coils have 6 radial and 7 axial windings and a resistance of  $50\text{ m}\Omega$  each. The geometry of the field produced by this arrangement was calculated numerically and is shown in Figure 4.9. The position of these coils was chosen to satisfy an intermediate condition between producing the maximum gradient and the most linear gradient at a given current.

The current through these coils can be turned off in less than 1ms using a FET-based switch. However, a fast change in magnetic flux through the steel chamber generates eddy currents which subside only after 10ms. The behaviour of the magnetic field inside the chamber was determined by using absorption imaging to measure the resonance frequency of atoms placed in the centre of the chamber

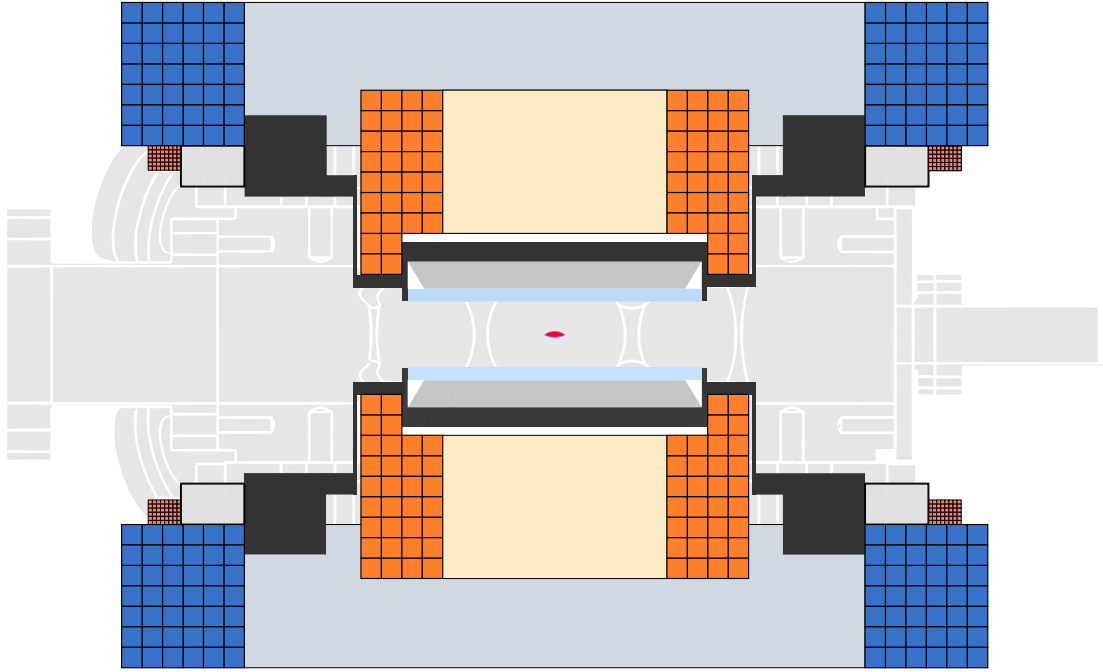


**Figure 4.8:** Cross section of main experimental chamber. This chamber has recessed windows (highlighted in black) in which the coils for the Feshbach field (orange) are contained. Next to the coils that produce the quadrupole field for the MOT (blue) are the vertical offset coils (red) for fine adjustment of the background magnetic field.

as a function of time after switching off the current in the coils. The atoms were placed and held in a 1 mK deep optical dipole trap before switching off the coils to allow for arbitrary measurement times. The results of this measurement are presented in Figure 4.10. At the moment the current through the quadrupole coils is turned off, the generated eddy currents in the steel chamber induce a magnetic field that shifts the resonance frequency by as much as 30 MHz within 4 ms. When the eddy currents decay, the resonance frequency of the atoms returns to what is expected at zero field.

The emergence of eddy currents is an unavoidable consequence of rapidly changing a magnetic field around a steel chamber. This is relevant not only when switching off the MOT but at any time the magnetic fields are changed. Therefore, this type of detailed study is important to work around this constraint.

### 4.3.2 Feshbach Coils

The coils described in this subsection are utilised to control the interactions between the atoms using Feshbach resonances. At the time when these coils

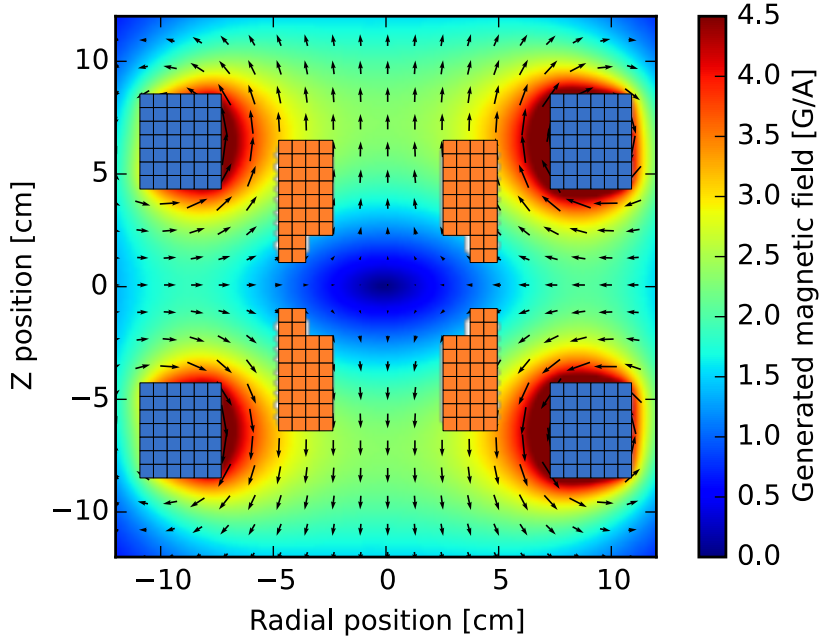


**Figure 4.9:** Quadrupole field geometry. Both quadrupole coils (■) and Feshbach coils (■) are shown. However, the field shown is only produced by the quadrupole coils and the current through the Feshbach coils is switched off. Given that the magnetic field scales proportionally to the current through the coils, the given values are divided by the current to provide a more general result.

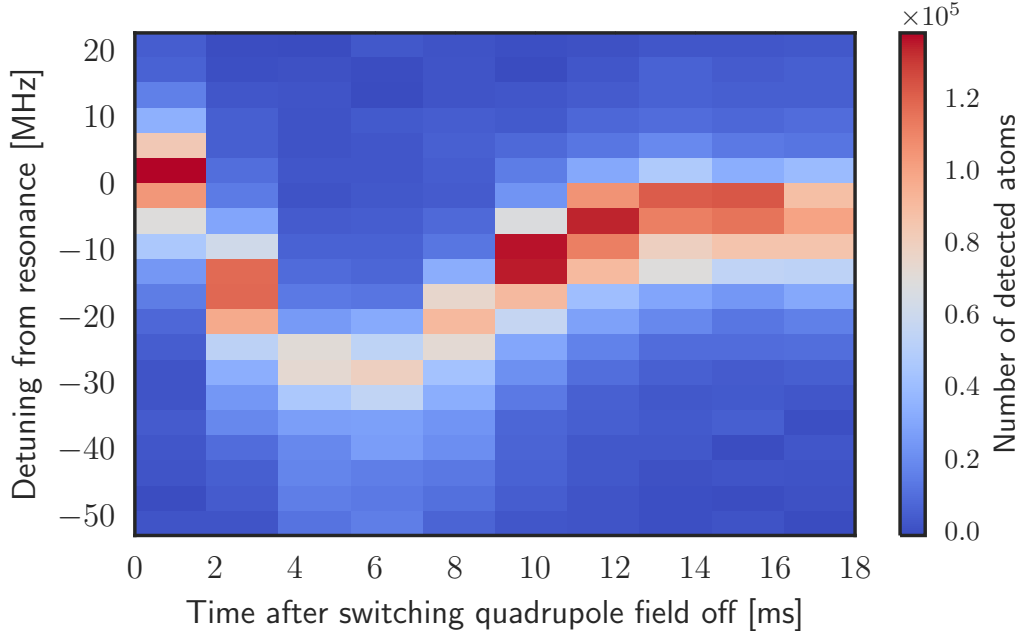


**Figure 4.10:** Shift of the atomic resonance frequency due to eddy currents caused by suddenly switching off the MOT quadrupole field.

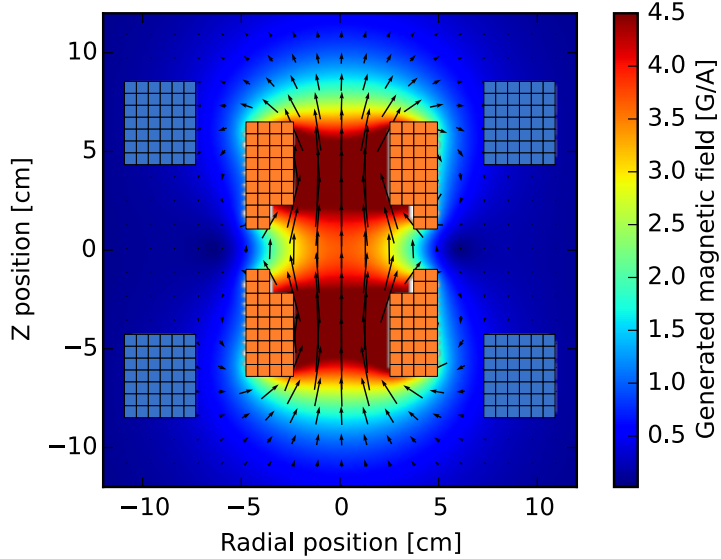


**Figure 4.11:** Field produced by the coils located inside the recessed windows (orange). These coils are used to control the interactions between the atoms. Given that the magnetic field scales proportionally to the current through the coils, the given values are divided by the current to provide a more general result.

were designed and built, the positions of the lithium-caesium resonances were not known. Thus, a robust system, capable of producing a wide range of magnetic fields, was necessary to ensure the resonances would be within reach.

The vertical windows in the main experimental chamber are recessed so that coils can be placed closer to the atoms and therefore achieve higher magnetic fields. The polarity of these coils is arranged such that a homogeneous magnetic field is produced at the position of the atoms. The coils were built with an axially varying number of windings as can be noted in Figure 4.8. The coils fit so tightly into these windows that extra care had to be taken during the design and winding process so that their leads would not obstruct them from fitting. The magnetic field produced by this arrangement was calculated numerically and is shown in Figure 4.11. Fields of up to 1400 G can be reached when passing a current of 400 A through them. When these coils are operated at 400 A, a stationary maximum temperature of 70 °C is reached. In practice, however, these coils are never used continuously but rather are only on for a fraction of an experimental sequence.

A magnetic field produced with coils which are finite in size will not be perfectly homogeneous. The residual curvature of the field results in a magnetic potential. This potential is trapping in the radial direction of the coils and

anti-trapping axially for atoms in the  $F = 1/2$  ground state, as can be seen in Figure 4.12. Furthermore, this potential adds to the one created from the dipole laser to produce a total trapping potential. To quantify the importance of the magnetic contribution to the potential, the trapping frequencies associated with it are calculated and compared with those of the dipole trap. This comparison is sufficient since the total trapping frequency, together with the atom number and temperature, determines the extent of the cloud as well as other thermodynamic properties. Figure 4.13 shows the frequencies of the magnetic trap (an imaginary frequency is used for the anti-trapping direction given that  $V(z) \propto \omega_{\text{vert}}^2$ ). In general, the trapping frequencies of the dipole trap are much higher than those of the magnetic trap. However, at dipole laser powers used at the end of evaporative cooling, these two frequencies are commensurate and the contribution from the magnetic trap becomes relevant.

It is important to accurately know the magnetic field at the position of the atoms as this determines the value of the scattering length. For this purpose, two different types of calibrations were done. The first one is based on finding the position of the zero-crossing of the scattering length of lithium which is well known to be 527 G [26]. Details about this measurement are presented in the following chapter in Figure 5.13. For the second calibration, the resonance frequency of lithium atoms was measured using absorption imaging. Since their interaction with static magnetic fields is well understood, the absolute value of the magnetic field was obtained from the resonance frequency of the atoms. These two methods give consistent results.

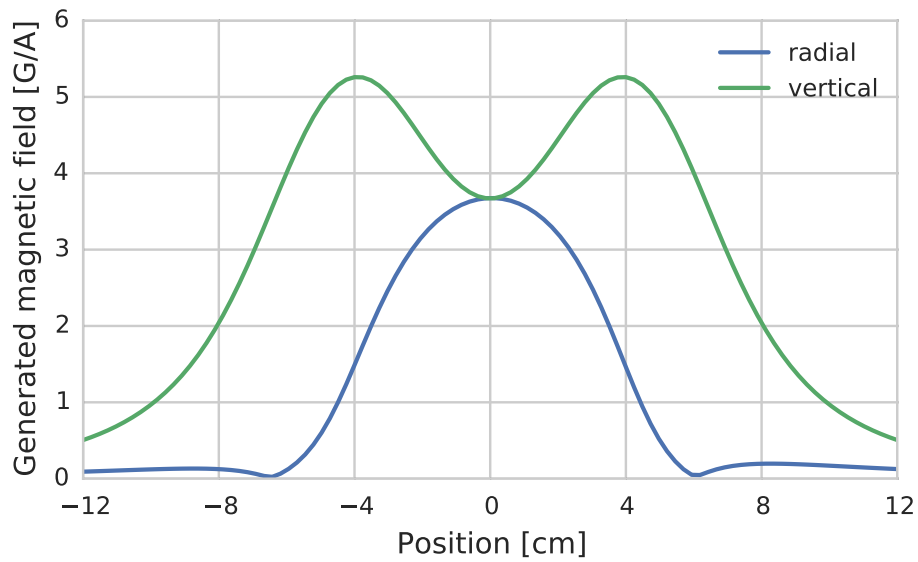


**Figure 4.12:** Radial ( $z = 0$ ) and vertical ( $r = 0$ ) cuts of the magnetic field shown in Figure 4.11 produced by the Feshbach coils.

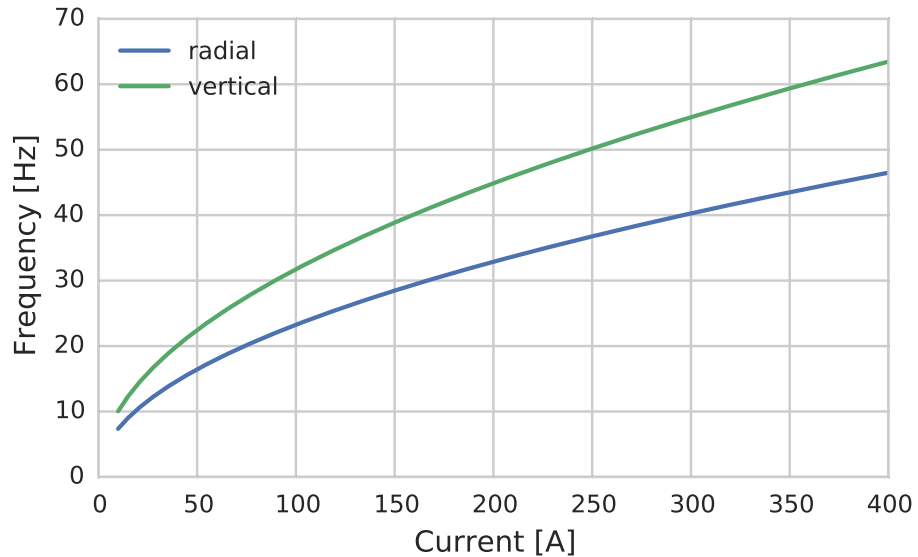


**Figure 4.13:** The finite curvature of the magnetic field produced by the Feshbach coils creates a potential. This potential is harmonically trapping in the radial direction while it is anti-trapping vertically. The given vertical frequency should be interpreted as an imaginary quantity such that the resulting potential is anti-trapping ( $V(z) \propto \omega_{\text{vert}}^2$ ).

## 4.4 Atom Source

An atomic beam is initially obtained by either heating a chunk of lithium or passing a current through caesium dispensers. Dispensers have been placed in the oven chamber as well as in the main experimental chamber to provide flexibility. Using the dispensers in the experimental chamber provides a higher flux of atoms at the expense of a degradation of the vacuum pressure. The lithium and caesium atoms that leave the oven are decelerated by the Zeeman slower on their way to the main experimental chamber so that they arrive with a velocity below the MOT's capture velocity. The magnetic field produced by the Zeeman slower is tailored independently for each of the atomic species and therefore, these are loaded sequentially. The reason behind designing the loading to be sequential stems from the fact that having a simultaneous MOT of lithium and caesium results in losses from light-induced collisions [69].

Figure 4.14 shows a detailed cross-section view of the oven chamber. The chunks of lithium consist of 95% pure lithium-6 from Sigma-Aldrich. To reach the necessary vapour pressure, it is heated to 700 K. At this temperature, the most probable velocity is  $1380 \text{ m s}^{-1}$  and 42% of the atoms are below this velocity. Since the MOT's capture velocity for lithium is around  $200 \text{ m s}^{-1}$ , a slower longer than a metre with fields over 1300 G would be required to slow down atoms with this initial velocity if 50% of the maximum possible acceleration  $a_{\max} = \Gamma \hbar k / 2$  is assumed. For practical reasons a 40 cm slower was built that only requires a maximum magnetic field of 860 G but still addresses 17% of the atoms leaving the oven. After an optimisation of the fields, it was found that an acceleration of  $0.3a_{\max}$  is more realistic.

A set of four caesium dispensers (SAES; model CS/NF/3.9/12 FT10+10) are used at a time in order to obtain caesium vapour. A current of typically 4.5 A is passed through the dispensers to heat them up to 820 K [70]. However, since there is no direct line-of-sight from the dispensers to the experimental chamber, caesium atoms undergo several collisions with the oven chamber before leaving towards the experimental chamber. The caesium oven chamber is heated to 370 K to avoid condensation on the walls. The most probable velocity for atoms in thermal equilibrium with the oven chamber is  $216 \text{ m s}^{-1}$  with, again, 42% of the atoms below this velocity. For these velocities, a slower of 80 cm with fields up to 110 G is necessary for an acceleration of  $0.5a_{\max}$ . Since the length of 40 cm is already fixed, we find that an optimum deceleration for caesium can be achieved with a

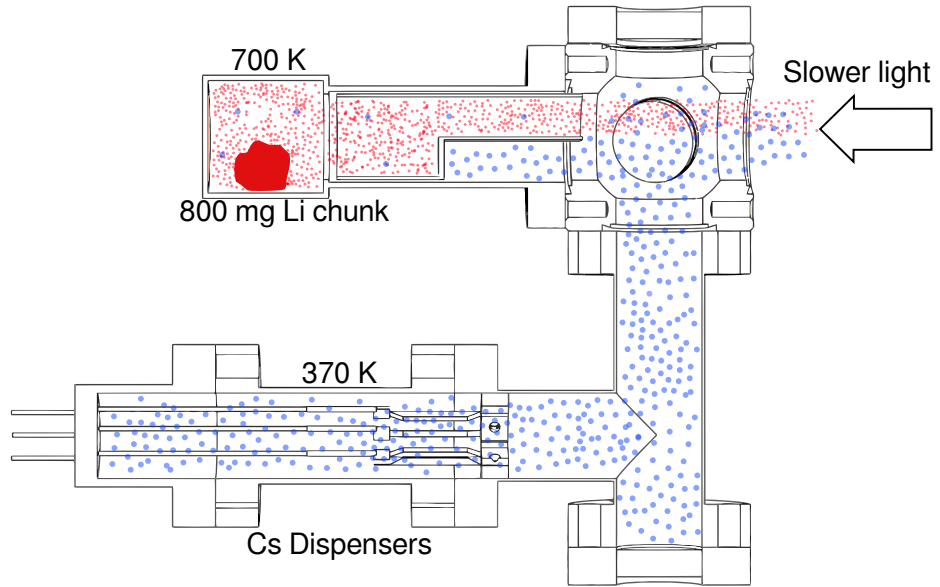


**Figure 4.14:** Oven chamber from which lithium (.) and caesium (●) are sourced. Lithium is obtained from heating a chunk in the upper section while caesium from running a current through dispensers in the lower section. Both atomic species leave this chamber towards the Zeeman slower located to the right of this diagram.

highest field of 80 G and this would address 21% of the atoms flowing through the slower. Nonetheless after manual optimization of the fields, an acceleration of  $0.8a_{\max}$  better reflects the behaviour of the slower.

After the atoms leave the oven chamber they travel through a series of coils that generate the magnetic field profile required for the operation of the Zeeman slower. Figure 4.15 depicts the oven chamber and the Zeeman slower's coils. These coils have been wound using Kapton-insulated, 1.72 mm × 3.14 mm copper wire. The maximum field produced by the largest coil is 900 G. The current in each of the coils is controlled using a series of field-effect transistors. For the caesium slower, 30 mW of cooling light is used with 0.6 mW of re-pumping light. The lithium slower is used with 20 mW of cooling and 14 mW of re-pumping light. The detunings at which the slower is operated are 95 MHz for cesium and 120 MHz for lithium for both the cooling and re-pumping transitions. Further details of this dual-species cold-atom source can be found in [1]. The performance of the slower with respect to the MOT loading is presented in Section 5.1.

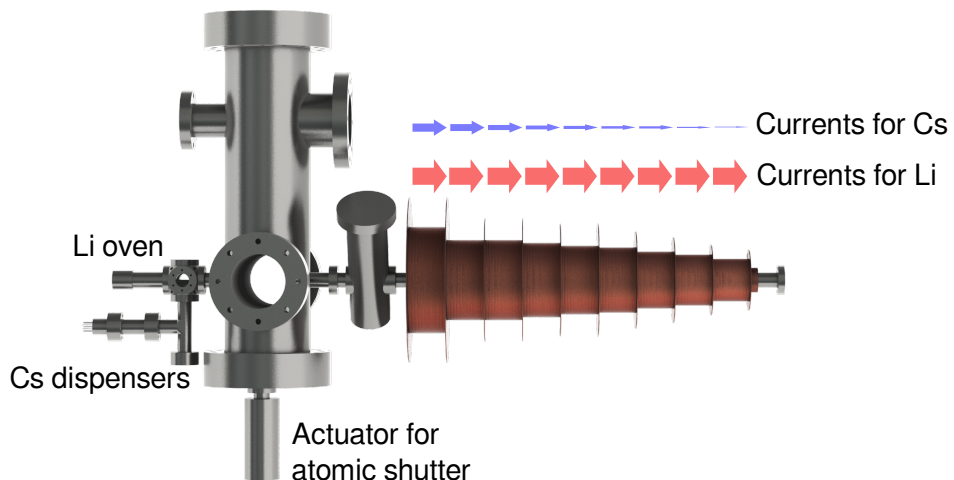


**Figure 4.15:** Zeeman slower coils. After atoms leave the oven chamber at the left of this figure they travel through a set of coils towards the experimental chamber. The current in each of the coils is tailored for each of the atomic species as depicted by the arrows shown.

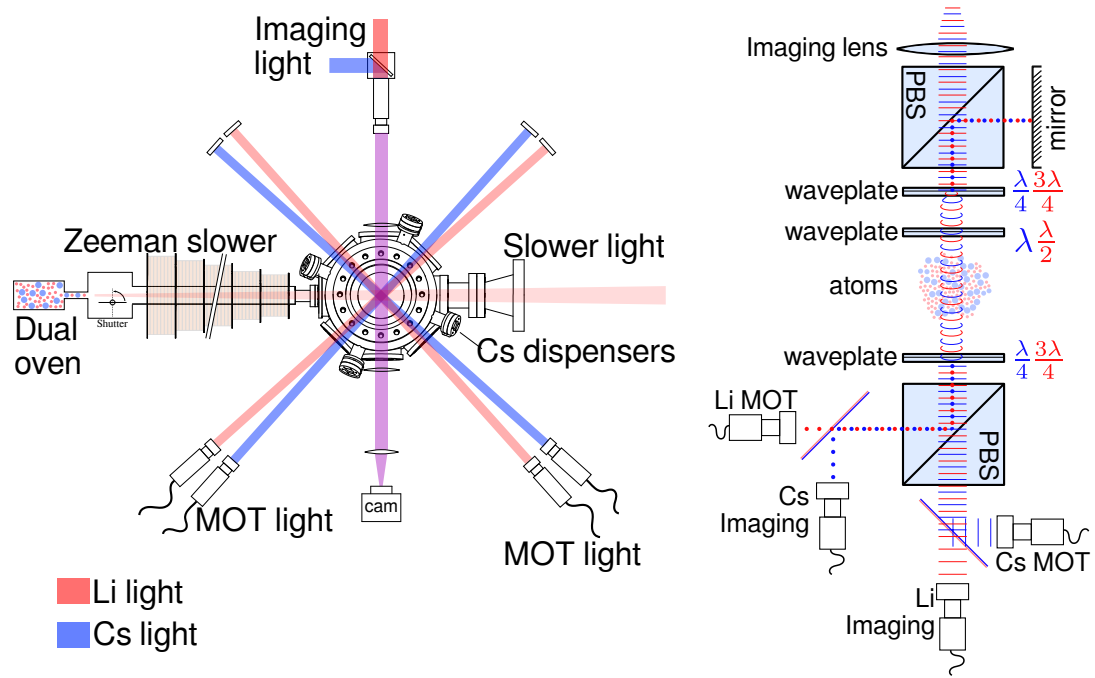
## 4.5 Magneto Optical Trap

Producing a MOT, as explained in Section 3.2, requires light for confinement in momentum space as well as a magnetic quadrupole field for spatial confinement. For a multi-species MOT, different wavelengths of light are required.

As was mentioned in Section 4.1, the light is prepared on a separate optical table to the one where the vacuum chamber is located and the MOT is created. Then, it is transferred to the proximity of the vacuum chamber through polarisation maintaining optical fibres. At the output side of the fibres, outcouplers with 10 mm lenses are used to collimate the light. The optical fibres used have a numerical aperture of 0.12 which, with this arrangement, results in beams with a  $1/e^2$  radius of 12 mm. Three optical fibres are used to obtain the light for each of the atomic species which is then retro-reflected to make up six beams. In the horizontal plane, lithium and caesium beams are produced by independent outcouplers. This arrangement is shown in Figure 4.16a.

The vertical MOT beams for lithium and caesium have been combined because the Feshbach coils inside the recessed windows constrain the angles of optical access. Furthermore, it is desirable to image the atoms from this axis for which the MOT beams are further combined with imaging light for both species. This arrangement is shown in Figure 4.16b.

For the lithium MOT, cooling and re-pumping light is distributed amongst



- (a) Horizontal arrangement. Light is obtained from independent outcouplers.
- (b) Vertical arrangement. Light is combined using PBS and dichroic mirrors.

**Figure 4.16:** Schematic of MOT optics.

all of the beams. Typically 28 mW are used for the cooler and 24 mW for the re-pumper per beam. The light for the Zeeman slower has 28 mW slowing light and 15 mW re-pumper.

On the other hand, for the caesium MOT, it is sufficient to provide re-pumping light through only one of the beams. Each beam has 24 mW of cooling light and one of them has an extra 2 mW of re-pumping light.

Producing both MOTs together leads to heating and losses due to large inelastic collisions between ground-state lithium atoms and excited caesium atoms [69]. To avoid this problem the two MOTs need to be loaded either spatially or temporally separated. In this work the MOTs are loaded sequentially and the caesium MOT displaced from lithium atoms loaded into the dipole trap by moving the zero-point of the magnetic field, where the MOT forms, using a bias field. The detuning of various beams is changed during the experimental sequence using the offset locks. Details of the timing and detuning can be found in Chapter 5.

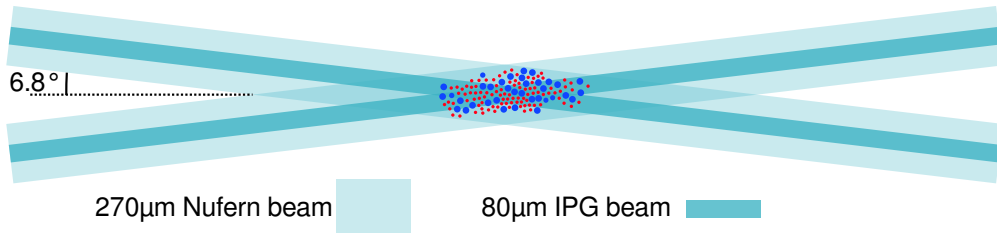


**Figure 4.17:** Geometry of the dipole trap beams in the vicinity of the crossing region where the atoms sit. The 80  $\mu\text{m}$  and 270  $\mu\text{m}$  beams are co-propagating.

## 4.6 Dipole Trap

After atoms have been trapped and cooled by the MOT, they are transferred into a far-of-resonance optical dipole trap for further cooling. This trap is produced by high-power infra-red lasers described in Section 4.1.4.

At the end of the MOT phase, the temperature of the caesium atoms is typically 40  $\mu\text{K}$  whilst lithium atoms can only be cooled down to typically around 400  $\mu\text{K}$ . In order to transfer a sufficiently large atomic sample from the MOT to the dipole trap, a much deeper trap is required for lithium than it is for caesium. However, having a red-detuned trap that would work for both species requires light with a frequency which is smaller than the transition frequencies for both the species, and would necessarily be deeper for caesium. Moreover, a far-of-resonance trap is desirable for evaporative cooling since this reduces photon scattering which causes heating. For this reason, lasers that emit with wavelengths around 1064 nm are used. High power 1064 nm lasers are commercially available together with the necessary optical components. At this wavelength the polarisabilities of lithium and caesium are  $4.5 \times 10^{-39} \text{ C m}^2 \text{ V}^{-1}$  and  $19.2 \times 10^{-39} \text{ C m}^2 \text{ V}^{-1}$  respectively [71] because the caesium resonance is closer. This means that a trap created with this wavelength would be a factor of 4.29 deeper for caesium than it is for lithium.

Given that the output power of the laser used to produce the trap is finite, a compromise between depth and size of the trap must be made. The large depth required by lithium imposes an upper bound on the size of the beam waists. On the other hand, with the larger polarisability and lower temperature achievable with caesium, a bigger and shallower trap would capture a larger atom number and avoid excess potential energy. For this reason a composite trap as shown in Figure 4.17 was implemented using the lasers described in Section 4.1.4. The

100 W IPG laser is focused down to a waist radius of 80  $\mu\text{m}$  and reflected back into the experimental chamber to cross it and produce the deep trap. With the Nufern 30 W amplifier, a shallow trap with a beam of waist radius of 270  $\mu\text{m}$  is created and is overlapped with the narrow trap.

When a harmonic trap is occupied by atoms, adiabatically changing the shape of the potential, i.e. the trapping frequency, changes the density and temperature while keeping the phase-space density constant. In contrast, if the trap resulting from the combined beams is filled with atoms, a potential which is more complex than a simple harmonic one is applied on them. This potential can be understood as a trap with a reservoir and dimple [72]. In this situation, a condensate can be formed by changing the frequency of the dimple or reservoir. For this to be possible, it is necessary that the ratio of the trapping volumes between the dimple and reservoir traps is large [72], which is the case of the presented setup.

An optical system is necessary in order to obtain the required beam sizes as well as controlling the intensity of the beams in time. The intensity of the beams is controlled using AOMs and a feedback loop as detailed in Subsection 4.6.1. The optical system was designed by modelling the Gaussian beam propagation using transfer matrices. The resulting scheme is shown in figures 4.18 and 4.19 for each of the lasers. The intensities reached can be high enough to cause thermal lensing when using conventional BK7 lenses. Instead, most of the lenses used are made of UV fused silica which has a lower thermal expansion coefficient as well as lower absorption compared to BK7 glass. The exception are the two lenses right next to the experimental chamber which are gradient-index lenses designed to withstand high powers. Using a gradient of index of refraction to make a lens as opposed to varying the thickness of the material, has the advantage that thinner lenses can be manufactured which is beneficial to avoid thermal lensing.

Using the polarisabilities of lithium and caesium mentioned before, the potentials created by the far-of-resonance light can be calculated. At high laser powers, where the forces produced by this potential greatly exceed the gravitational force, the trap depth  $U$  and trap frequency  $f$  is related to the power by  $U = cP$  and  $f = A\sqrt{P}$  respectively, where  $c$  and  $A$  are proportionality constants. These parameters, that characterise the trap, have been calculated independently for each of the lasers and are reported in Table 4.3. These values are valid in the horizontal plane where gravity does not play a role and thus, the simple functional forms given are accurate. Vertically, the effect of gravity was estimated using a truncated harmonic potential. In the case of the IPG laser, the depth decreases

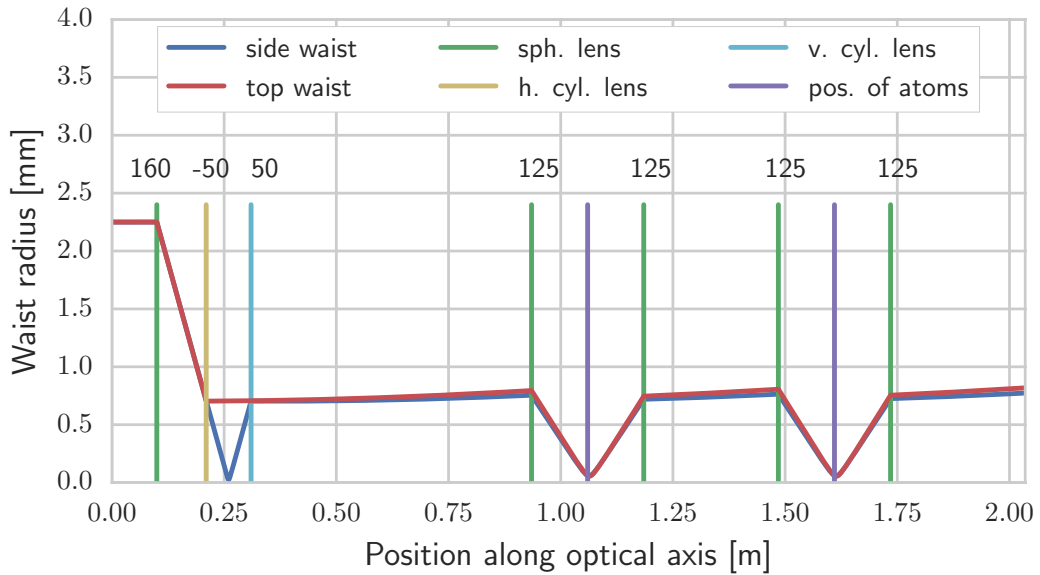


**Figure 4.18:** Lens arrangement for the IPG laser. Cylindrical lenses are used for optimal operation of the AOM. Therefore, the waist is given for both the side and top views. At the position of the atoms, an  $80\text{ }\mu\text{m}$  beam waist is achieved for both passes of the beam.

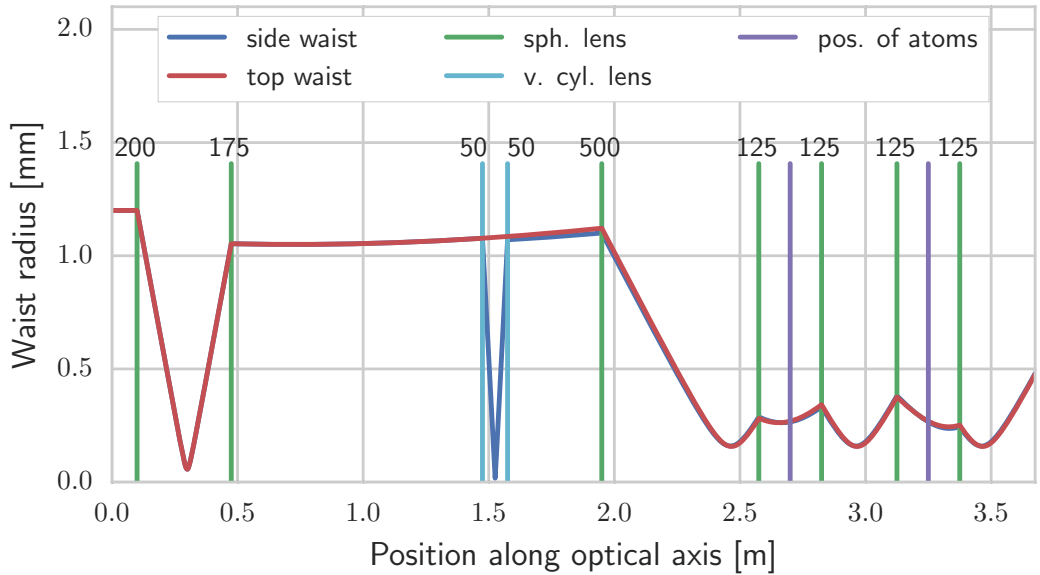


**Figure 4.19:** Lens arrangement for the Nufern laser amplifier. Cylindrical lenses are used for optimal operation of the AOM. Therefore, the waist is given for both the side and top views. At the position of the atoms, an  $270\text{ }\mu\text{m}$  beam waist is achieved.

by 10% due to gravity at 10 W for caesium and 2 W for lithium. For the Nufern trap, gravity is always important in the vertical direction for both species.

		Trap depth [ $\mu\text{K W}^{-1}$ ]	Radial freq. [ $\text{Hz W}^{-1/2}$ ]	Long. freq. [ $\text{Hz W}^{-1/2}$ ]
Lithium	IPG	12.1	525.5	62.7
	Nufern	1.1	45.0	5.4
Caesium	IPG	52.1	236.7	28.2
	Nufern	4.7	20.3	2.4

**Table 4.3:** Calculated depth and frequency coefficients for the dipole trap.

Depth  $U$  relates to power  $P$  as  $U = cP$  and the  $c$  coefficient is given in the table. For the trap frequency  $f$  the behaviour is  $f = A\sqrt{P}$  and the  $A$  coefficient is the one reported.

For the dipole trap to operate as intended, it is necessary to cross the two beams precisely with each other. However, the only way to assess the crossing is by observing atoms loaded into the trap. This, together with the high powers involved, makes using manually operated mirror mounts difficult. A mirror mount, motorised using a picomotor from Newport, facilitates the alignment process. This alignment is carried out using images from a point of view like the one in Figure 4.17. Even though the separation between the beams is not apparent from this point of view, it is obvious when the beams are crossed. Only when they are crossed is there longitudinal confinement and atoms concentrate in the crossed region. The crossing of the beams is adjusted by moving the returning beam vertically, using the pico motor, until an enhancement of the number of atoms in the central region is observed. This process is repeated at lower dipole powers to more finely adjust the crossing.

The frequencies for the trap created with the IPG laser have been measured using two different methods. The first method, illustrated in Figure 4.20, is called parametric heating. For this, the atoms are placed in the dipole trap and held at the desired trapping power, after which, the intensity of the trap's light is modulated at various frequencies. When the modulation frequency is twice the trap frequency an enhanced loss of atoms is observed due to parametric heating. The factor of two can be understood by first considering the atoms occupying harmonic oscillator states  $|n\rangle$  resulting from the potential  $V(x) = \frac{1}{2}m\omega_0^2x^2$ . Then, a perturbation of the form  $V_p(x, t) = \frac{1}{2}m\lambda^2 \cos(\omega_p t)x^2$  is applied, where  $\lambda$  is the strength of the perturbation and  $\omega_p$  its frequency. The important point here is

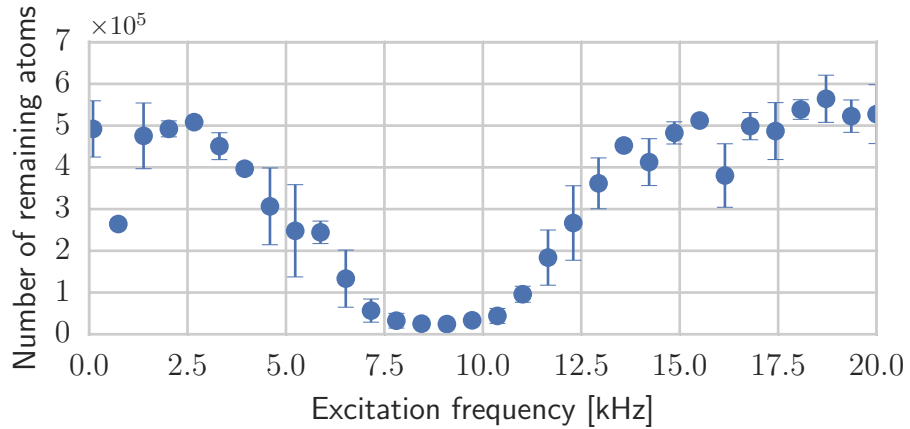


**Figure 4.20:** Parametric excitation trap frequency measurement. The number of remaining atoms is measured after modulating the dipole laser intensity for 100 ms at various frequencies. Loss resonances can be seen at  $\sim 1$  kHz and  $\sim 9$  kHz corresponding to the longitudinal and radial trap frequencies respectively. For each frequency, the atom number measurement is repeated three times and averaged. Error bars represent the standard deviation.

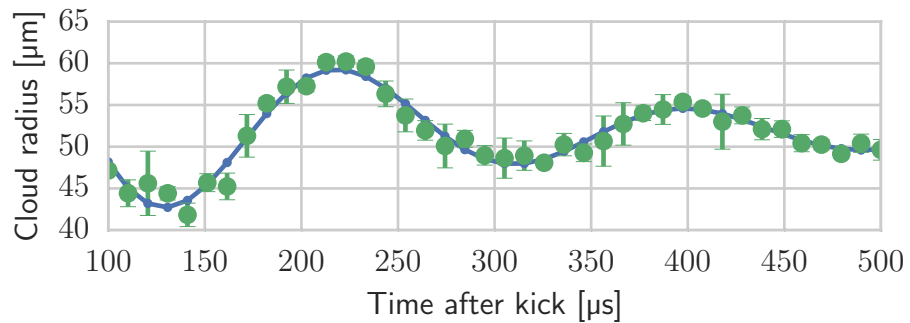


**Figure 4.21:** Breathing-mode oscillation trap frequency measurement. The size of the atomic cloud is measured as a function of time after a sudden change in the trap frequency at  $t = 0 \mu\text{s}$ . Each point has been measured three times and error bars represent the standard deviation. The cloud radius is determined by fitting a Gaussian to the cloud's profile and the standard deviation of the Gaussian is used as the radius.

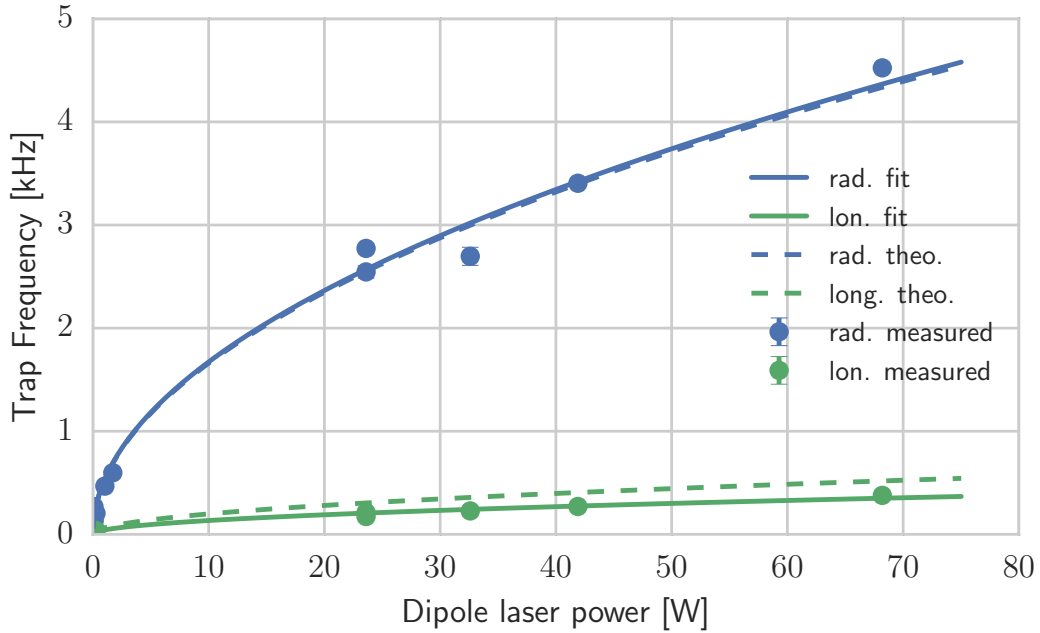


**Figure 4.22:** Frequencies for the trap created by the IPG laser. Theoretical and experimental data are compared for both radial and longitudinal frequencies.

that the perturbation is proportional to

$$x^2 = \frac{\hbar}{2m\omega_0} (aa + a^\dagger a + aa^\dagger + a^\dagger a^\dagger),$$

where  $a$  and  $a^\dagger$  are the raising and lowering operator of the unperturbed harmonic oscillator. All the terms in  $x^2$  only couple states of equal parity and therefore, for the perturbation to drive the atoms upwards in the energy ladder it must provide an energy of twice the level spacing.

The second method begins by suddenly changing the trap frequency which induces breathing-mode oscillations of the atomic cloud. The size of the cloud will oscillate as shown in Figure 4.21 at twice the trap frequency. Thus, the trap frequencies are determined by measuring the size as a function of time. An overview of the results is shown in Figure 4.22 in which the results for both methods have been aggregated. We find good agreement between the model and measured radial frequencies whilst the actual longitudinal frequencies are 68% of the theoretically predicted ones.

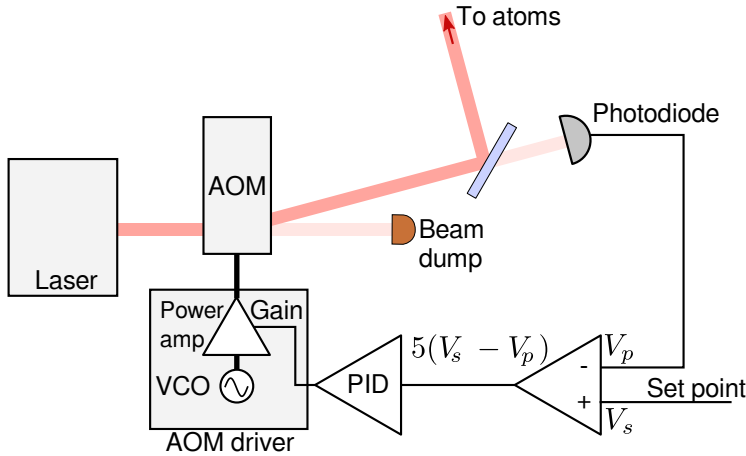


**Figure 4.23:** Scheme for power stabilisation of dipole trap lasers. A fraction of the beam's power is collected in a photodiode. The output of the photodiode is used as feedback in a PID stabilisation system.

#### 4.6.1 Power Stabilisation

Implementing evaporative cooling requires precise control of the depth of the dipole trap. For this purpose, the intensity of the light that produces the trap is actively controlled through a feedback loop. This control not only facilitates the implementation of evaporation ramps, but it also decreases fluctuations in the intensity that would otherwise lead to heating.

The stabilisation system is shown in Figure 4.23 and the same principle is used for both of the dipole trap lasers. The output of the laser is passed through an AOM and the first order of the diffracted light is then used to produce the optical dipole trap. By, changing the RF power going into the AOM it is possible to control the amount of light power going into the first order. A small fraction of the diffracted light is diverted into a photodiode which is used to provide feedback. The measured power is compared with a set-point provided by the experimental control system using a differential amplifier. This differential amplifier also increases the amplitude of the signal by a factor of five to improve the sensitivity of the system. The amplified signal is then used as an error signal and fed into a PID controller. The output of this PID controller is connected to the AOM driver and sets the power of the RF signal going into the AOM.

With this scheme it is straightforward to produce any evaporation ramp, within the bandwidth of the feedback loop, generated by the experimental control system. The power of the laser has been sinusoidally modulated with frequencies of up to 15 kHz with this system, where it has been applied to measure the trapping

frequencies.

A limiting factor with the presented method is that only signals within the range of the photodiode may be controlled in this way. If the photodiode is set to cover the full range of laser powers, the sensitivity at the final stages of the evaporation, where it is most critical, would not be favourable. For the lithium evaporation sequence, the power of the dipole trap decreases by a factor of  $10^3$ . Therefore, the laser's current is used to control the output power in the higher end of the range, from 100 W to 40 W, while the feedback system is only active at the lower end, from 30 W down to 50 mW, thus, achieving a higher stability is achieved during operation at low power.

Despite the stabilisation system reducing the noise in the intensity [37], residual fluctuations of intensity and beam pointing, as well as off-resonant photon absorption cause heating of the atoms. We measured the heating rate for lithium atoms and the results are presented in Figure 4.24. For this measurement, an equal mixture of lithium atoms in the  $|F = 1/2, m_F = 1/2\rangle$  and  $|F = 1/2, m_F = -1/2\rangle$  ground states was placed in the dipole trap and subsequently evaporatively cooled until a power of 3.3 W was reached. Then, the atoms were held in the dipole trap for various amounts of time after which the temperature was measured using time-of-flight images. It is worth noting that this measurement was taken at a final dipole trap power of 3.3 W and it is not expected that the heating rate should be the same at all powers of the dipole trap.

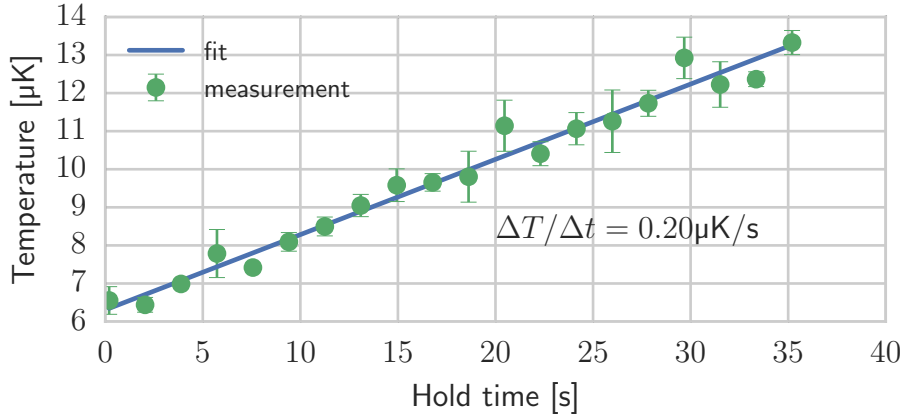


**Figure 4.24:** Heating rate in the dipole trap produced by the IPG laser. A lithium sample in an equal mixture of the  $|F = 1/2, m_F = 1/2\rangle$  and  $|F = 1/2, m_F = -1/2\rangle$  ground states is placed in the dipole trap. Evaporative cooling is then carried out until the laser power reaches 3.3 W which corresponds to a depth of 40  $\mu\text{K}$ . At this point the scattering length was set to zero and the sample was held at various amounts of time, after which the temperature was measured using time-of-flight images. Error bars represent statistical standard deviation resulting from three repetitions. A line was fitted to calculate the heating rate.

## 4.7 Total Trapping Potential

While the dipole trap dominates for large laser powers, at the low end of the range a potential that arises from the magnetic field becomes relevant. As mentioned in Section 4.3.2, the coils that produce the magnetic field, used to control the scattering length, generate a magnetic field with a slight gradient. Thus, a potential arises from the interaction of this field with the atomic spins. The following analysis shows that this potential is very shallow and it is only relevant during the final stages of evaporation. The contributions of this magnetic potential and the optical potential created by the IPG laser are analysed in Figure 4.25. Each of these mechanisms, which independently produce a trap frequency  $f_i$  in a given direction, add up to an effective total trap frequency given by

$$f_{\text{eff}} = \sqrt{\sum_i f_i^2}.$$

Therefore, the fit to the experimental data of the total frequency  $f_{\text{tot}}$  was calculated using a model function of the form

$$f_{\text{tot}}(P) = \sqrt{A^2 P + f_{\text{mag}}^2},$$

where  $A$  is a constant determined by the fit and  $P$  is the dipole laser power and  $f_{\text{mag}}$  is the calculated magnetic trap frequency when the coils produce a field of 780 G. This value for the magnetic field is in the vicinity of the Feshbach resonance addressed during evaporative cooling. As made clear by the figure, extinguishing the optical dipole trap does not result in free fall if the magnetic potential still remains. In the radial direction of the atomic cloud, the optical trap frequency remains high compared to the magnetic trap and therefore there is practically no influence of the magnetic component. For the longitudinal direction, the magnetic contribution is the largest for powers below 1 W. In this case, if the trapping frequency decreases to 80% of its original value  $f_{\text{tot}}$  when the dipole laser is turned off, the cloud would have a size which is 5% smaller than a free expanding one within  $\sim 1$  ms. The consequences of this are further discussed in Section 5.4.3.

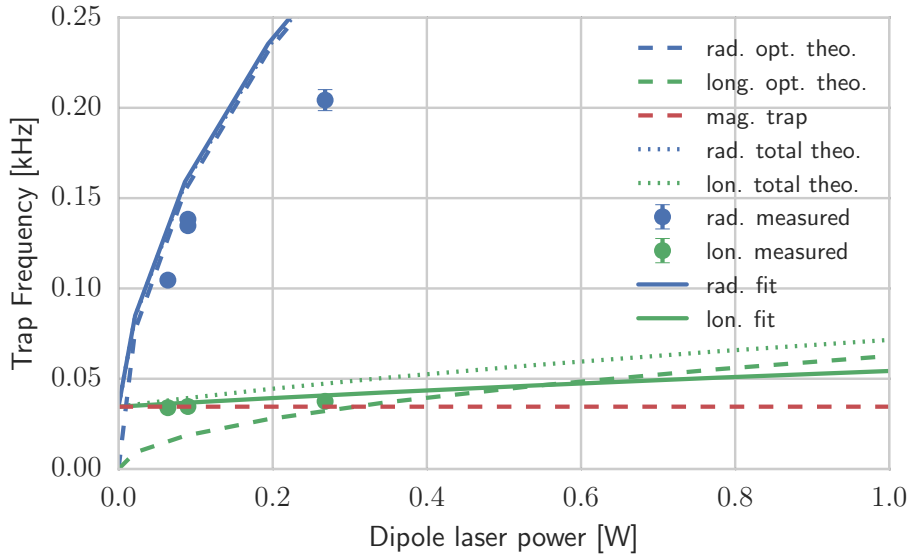


**Figure 4.25:** Analysis of trap frequencies at low laser powers. The basic contributions to the trap frequency by the optical (opt.) and magnetic (mag.) potentials are presented for the case where the Feshbach coils produce a field of 780 G. These contributions were theoretically calculated and are the same that appear in figures 4.13 (mag.) and 4.22 (opt.). These two contributions add up to the total theoretical frequencies shown. The experimentally measured values and their corresponding fits are also displayed. Here, radial (rad.) and longitudinal (long.) refer to the directions defined by the elongated atomic cloud in the dipole trap.

## 4.8 Imaging

A vast majority of the measurements presented in this work have been obtained through absorption imaging, the principle in which is described in Section 3.5. In brief, this method consists in shining a beam of light onto an atomic cloud and quantifying the amount of light that gets absorbed and subsequently scattered. Regions of higher atomic density lead to higher absorption which results in mapping the atomic density into a light intensity pattern which is measured using a CCD camera.

The frequency of the imaging laser is set to be resonant with an atomic transition and controlled using an offset lock. This is convenient since it allows to finely adjust this frequency to optimise the sensitivity of measurement. The number of detected atoms as a function of probe light frequency is shown in Figure 4.26. The power of the probe beam is such that the intensity is much lower than the atoms' saturation intensity (with a 1 mW beam of 25 mm in

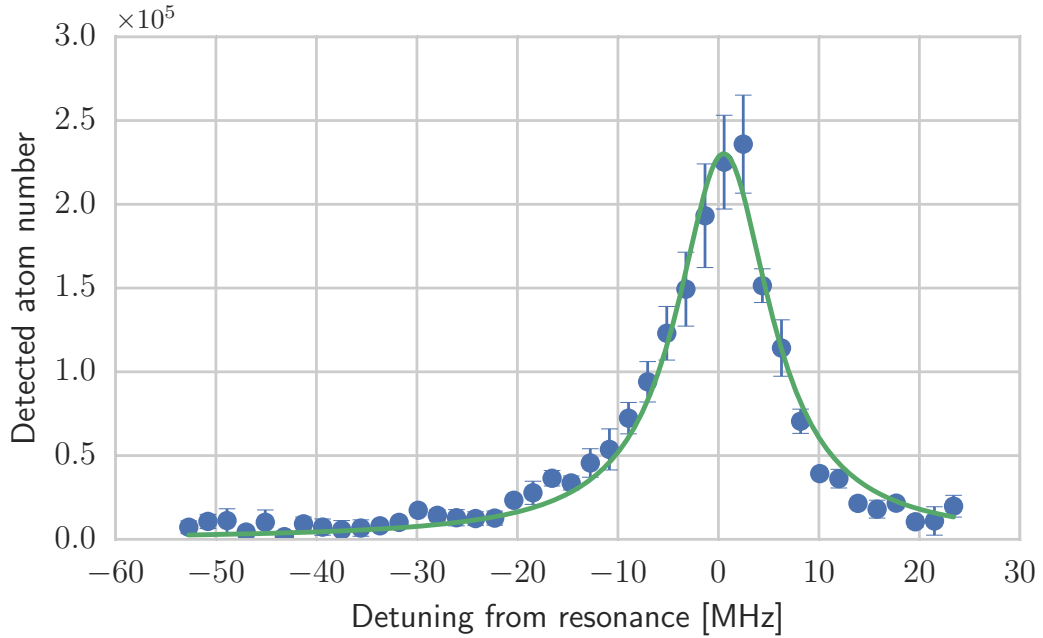


**Figure 4.26:** Number of detected lithium atoms through absorption imaging as a function of the frequency of the probing light. This measurement was carried out at zero magnetic field after holding the atoms in the dipole trap for 500 ms to avoid effects of transient electromagnetic fields created by the MOT. The line shown is a Lorentzian fit that results in a linewidth (FWHM) of  $\Gamma/2\pi = 11.3$  MHz. As the excited states of lithium overlap (see Figure 2.1) the measured linewidth is larger than the natural linewidth of the  $F = 3/2 \rightarrow F' = 5/2$  transition which is  $\Gamma/2\pi = 5.2$  MHz [42]. Error bars represent the statistical standard error resulting from measuring each point four times.

diameter,  $I_{\text{probe}} \approx 0.2I_{\text{sat}}$ ). The advantage of using this regime is that the density measurement depends only on the ratio  $I_{\text{out}}/I_{\text{in}}$  and not on the absolute intensities (see Equation 3.10).

The measurement is performed by capturing three images as shown in Figure 4.27. A first one (4.27a), which contains the intensity profile after light has been absorbed by the atoms. The second (4.27b), is captured after the atoms have left the field of view and only measures the unaltered incoming light. Finally a picture is taken without atoms and probing light to account for any stray light (4.27c). The measured density profile resulting from these images is displayed in Figure 4.27d.

The intensity profiles are imaged onto a CCD (AVT Guppy 038-B) camera chip using a two-lens telescope as shown in Figure 4.28. This optical setup is used

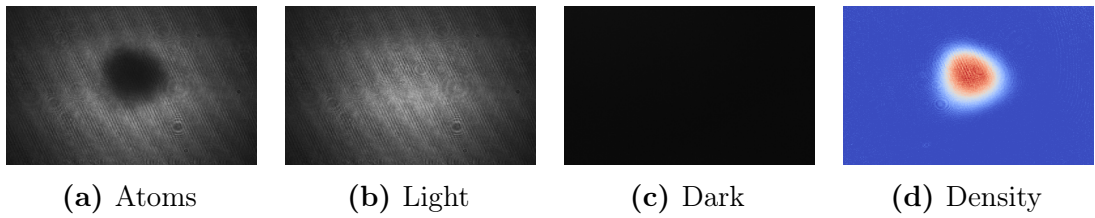


**Figure 4.27:** Typical absorption imaging measurement. The three images captured for absorption imaging (a-c) to measure the distribution of atoms (d). Images (a-c) are obtained from the CCD camera and brighter regions indicate higher light intensity. The density is calculated from these three images and it is shown in (d). In this, redder regions indicate a higher density.

with a magnification between 0.5 and 3.3 depending on the scale of interest. When studying the MOT, a de-magnification is preferred while for observing atoms in the dipole trap, a magnification of 3.3 is used. The probe light intensity was below  $0.4 \text{ mW cm}^{-2}$  and the exposure time used was between  $10 \mu\text{s}$  and  $100 \mu\text{s}$ .

The maximum attainable resolution is determined by the lens closest to the atoms. Vertically, this is a 25.4 mm diameter lens with a focal length of 75 mm. The diameter of this lens is constrained because it is placed inside of the coils in the recessed windows. The constraint in the focal length results from the optics needed to retro-reflect the MOT beams (see Figure 4.16b). However, replacing the polarising beam-splitter cube and mirror which are next to the imaging lens with a reflective polariser, this situation may be improved. The horizontal lens is a 50 mm diameter gradient-index lens with a focal length of 125 mm also used to focus down the dipole trap. With this arrangement, the diffraction-limited achievable resolution is calculated according to the Rayleigh criterion and shown in Table 4.4.

	Lithium	Caesium
Horizontal Resolution [ $\mu\text{m}$ ]	2.0	2.6
Vertical Resolution [ $\mu\text{m}$ ]	2.5	3.1

**Table 4.4:** Resolution limit for each of the atomic species for both the vertical and horizontal imaging axis with the currently used lenses. The numbers are given in  $\mu\text{m}$ .

When imaging without an external magnetic field, the probe light is on resonance with the  $F = 3/2 \rightarrow F' = 1/2$  transition for lithium and the  $F = 4 \rightarrow F' = 5$  for caesium. As with the MOT, re-pumping light is needed to keep the atoms in the desired cycling transition. For this purpose, the re-pumper

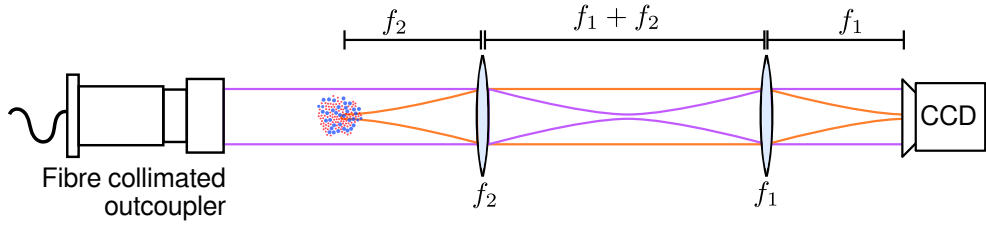


**Figure 4.28:** Geometry of imaging optics setup. The distance between the lenses chosen as such ensures that the magnification of the system will be less sensitive to misalignment. For the horizontal arrangement the lenses used are  $f_1 = 60$  mm and  $f_2 = 125$  mm. Vertically  $f_1 = 250$  mm and  $f_2 = 75$  mm lenses are used.

light from the MOT is shone while capturing absorption images. For simplicity, the re-pumping light is not combined with the imaging beam but rather, the re-pumper from the MOT outcouplers is used.

#### 4.8.1 High Field Imaging for Lithium

The relatively small hyperfine splitting of the lithium-6 ground state implies that the Paschen-Back regime of the atom-field interactions can be reached at relatively low magnetic fields above 200 G (see figures 2.2 and 2.3). In this regime, the transitions become closed and absorption imaging can be performed without the need of re-pumping light. The transition frequencies required for imaging can be calculated analytically. The ground state energies as a function of magnetic field are obtained with the Breit-Rabi formula [44]. For the excited state, treating the hyperfine splitting as a perturbation to the magnetic interaction  $\mu_J \cdot \mathbf{B}$  is a good approximation.

When lithium atoms are loaded into the dipole trap they are pumped into the  $|F = 1/2, m_F = -1/2\rangle$  and  $|F = 1/2, m_F = +1/2\rangle$  ground states to avoid inelastic collisions with atoms in the  $F = 3/2$  ground state manifold. Additionally, this mixture is necessary for evaporative cooling, which relies on elastic collisions, that with a single state would not be possible. At high magnetic fields, compared to the hyperfine splitting, these two states correspond to  $|m_J = -1/2, m_I = 0\rangle$  and  $|m_J = -1/2, m_I = 1\rangle$ . Varying the frequency of the imaging laser it is possible to observe the population in each of these states as shown in Figure 4.29. The measured linewidth of  $\Gamma/2\pi = 13$  MHz is wider than the natural linewidth  $\Gamma/2\pi = 5.2$  MHz. This broadening may be due to the linewidth of the imaging laser. The separation between the levels was measured to be 78.4 MHz and the expected one,

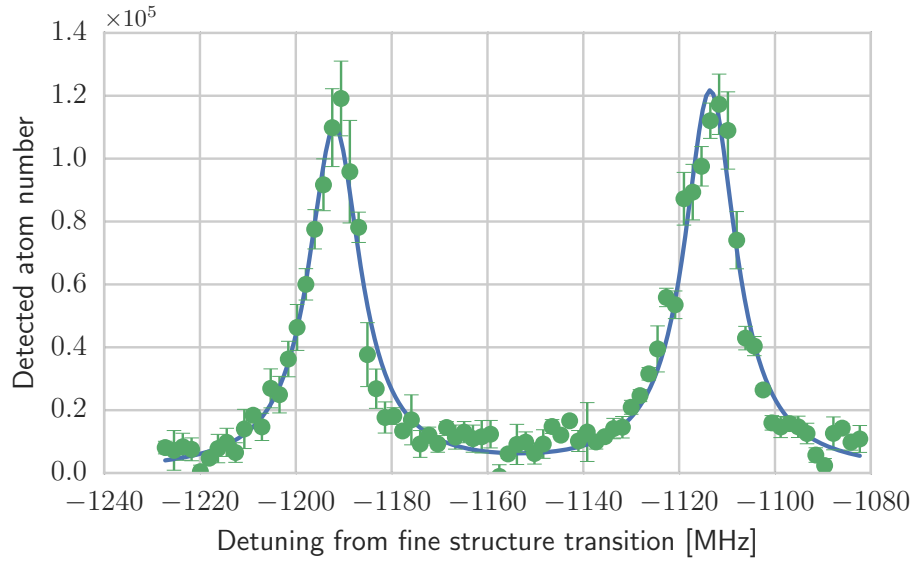


**Figure 4.29:** High-field spectrum of lithium at 856 G. Number of detected atoms in the dipole trap through absorption imaging as a function of the frequency of the probe light. These atoms were optically pumped into the  $F = 1/2$  ground state while loading them in the trap. The two states  $|m_J = -1/2, m_I = 0\rangle$  and  $|m_J = -1/2, m_I = 1\rangle$  are clearly resolved. The line shown is a fit with a dual-Lorentzian function that result in a linewidth (FWHM) of  $\Gamma/2\pi = 13$  MHz, population ratio of 53:47 between them, and a separation of 78.4 MHz between the two maxima. Error bars show the statistical standard error resulting from four repetitions.

according to the theory described in Section 2.2, is 76.9 MHz.

The desired frequency can be obtained by locking the imaging laser using an offset lock which works on the principle described in Subsection 4.1.1.2. This version, capable of higher detuning, is based on previous work [73]. It is able to cover a wide range of frequencies and thus, magnetic fields. This design is more complex than the other offset locks used in the experiment. This setup uses two VCOs (Mini-Circuits ZX-95-200-S+ and ZX95-1700W-S+) which are switched between (ZX80-DR230-S+) to be able to cover the required frequency range. Using the high-field VCO, detunings (with respect to the fine-structure transition) between -600 MHz and -1230 MHz can be reached; this corresponds to magnetic fields between 450 G and 950 G. Also, for splitting the signal, a splitter (Mini-Circuits ZFSC-2-1-S+) is used instead of a T-piece to obtain a cleaner signal. A coupler (ZFDC-15-5-S) is helpful for measuring the beat frequency directly.

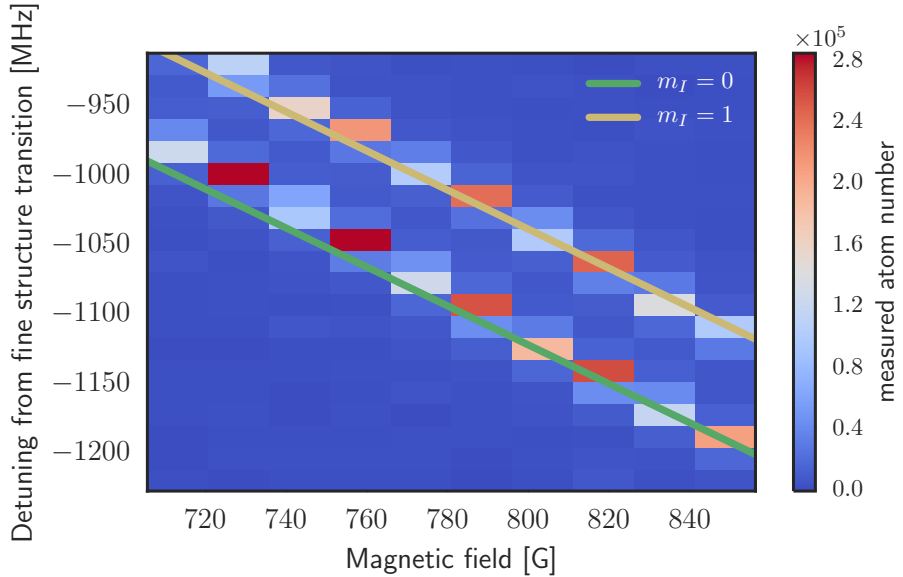


**Figure 4.30:** High-field spectrum of lithium. Grayscale pattern shows the number of detected atoms as a function of probe light detuning and magnetic field. The lines show theoretically calculated transition frequencies according to the theory described in Section 2.2.

Furthermore, a high-bandwidth photodiode (Hamamatsu G4176 has a bandwidth of 9 GHz) is used to detect the beat.

With this system, the spectroscopic measurement of Figure 4.29 can be easily executed. Collecting many of these measurements at different magnetic fields it was possible to measure the behaviour of the energy levels as in the Breit-Rabi diagram. The aggregated results of such measurement is shown in Figure 4.30. The slight mismatch between the measurement and theoretical values may be due to fluctuations in the magnetic field or technical errors in the determination of the absolute frequencies.

## 4.9 Control System

The execution of this experiment requires controlling a vast number of parameters such as the detuning and intensity of the cooling, re-pumping, Zeeman slower, optical pumping and optical dipole trap light. Also the current going through the Zeeman slower, MOT, Feshbach field and offset coils is controlled. Moreover, multiple devices need operating during an experimental run. These include CCD cameras, mechanical and acousto-optical shutters for the light, actuators for the alignment of the dipole trap, and atomic dispensers.

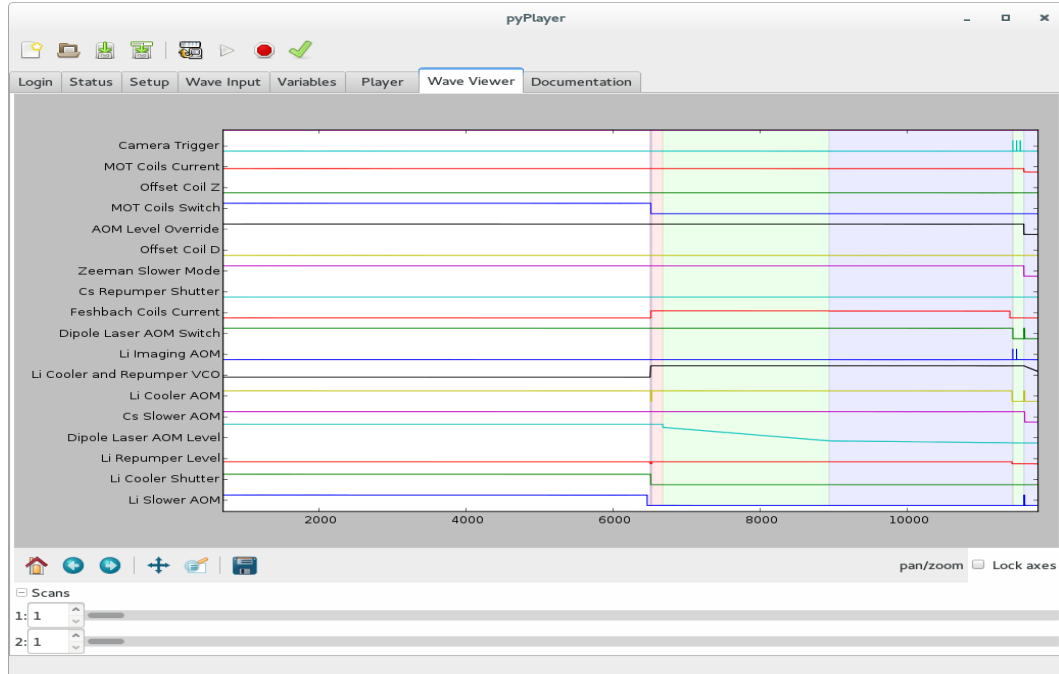


**Figure 4.31:** Screenshot of control system client showing the tab used to visualise the sequence.

The orchestration of all of these components is carried out by a programmable signal generator. This control system is based on National Instruments' PXIE-8130 controller and its add-on digital and analogue output cards. With this hardware it is possible to output signals defined with a temporal resolution of  $1\text{ }\mu\text{s}$  and voltage resolution of 16 bits spanning from  $-10\text{ V}$  to  $10\text{ V}$ .

The software of this system was developed in house and it has a client-server architecture. The PXIE-8130 runs the server software tasked with synthesising the signals from the instructions sent by the client. The client and server communicate through a custom-made TCP/IP protocol.

The client program provides a graphical user interface (GUI) for the development and execution of experimental sequences. This piece of software was developed jointly by Matthew Jones [37] and the author using python some of its common libraries (pygtk, numpy and matplotlib). One of the modules developed by the author is the sequence plotter shown in Figure 4.31. This allows the visualisation of sequences during their design and execution for a better understanding of the factors at play, highlighting the advantages of developing a GUI-based software.

An important feature built into this client is the ability to create modular control sequences. This means that blocks of instructions can be invoked into

a sequence making it easy to conceptualise and implement the different stages involved in an experimental run. Further details of the control system, including both the client and server, can be found in [37].

## 4.10 Apparatus Outlook

The experimental apparatus described in this chapter is in continuous evolution. With it, Bose-Einstein condensates (BEC) containing  $10^4$  lithium Feshbach molecules are routinely produced and important steps towards producing ultra-cold caesium gases have been made. Through using and testing the apparatus improvements good areas of improvement have been identified. In this last section an overview of some suggested improvements that can be carried out in the near future are presented.

### 4.10.1 Magnetic Field Curvature Compensation

The Feshbach coils shown in Figure 4.8 (marked with  ) produce strong and stable magnetic fields. The finite curvature in the field results in an undesirable magnetic potential described in Section 4.3.2. This does not affect in-situ measurements but makes carrying out time-of-flight studies at and around the Feshbach resonance challenging. It is thus, convenient to remove this curvature.

A straightforward approach may be to use the MOT coils (marked as  ) in addition to the Feshbach coils, such that the field would add up and cancel the the curvature. However, the magnetic features produced by these coils would be too blunt to correct for the inhomogeneity caused by the smaller Feshbach coils. Alternatively, the larger coils may be used to produce the bulk of the field which, to start with, would be more homogeneous. Then, the inner coils can further flatten the magnetic field.

The implementation of this scheme requires that the polarity of one of the coils is flipped during the experimental sequence. In one configuration it would be used to produce the quadrupole field for the MOT whilst it would play a part in generating the homogeneous magnetic field when the polarity is flipped. For this purpose an H-bridge can be used.

In order to use the larger coils to produce a magnetic field with the same strength as the inner coils can produce, a current which is 16% higher than the currently used value  $I_{\text{cur}}$  is required. With this arrangement, the radial frequency

of the magnetic trap resulting from only using the larger coils is 2.9 times smaller than if the smaller coils are used.

Using the large and small coils in combination, a current in the large coils  $I_{\text{lrq}}$  which is 30% larger than  $I_{\text{cur}}$  would be needed. This is because a current in the small coils found to be  $I_{\text{sml}} = -0.1I_{\text{lrq}}$  compensates for the curvature while decreasing the overall field. With this arrangement, the frequency of the undesirable magnetic trap is decreased twenty-fold with respect to the current value. With this reduction, when releasing the atoms after evaporative cooling, the atomic cloud would need to expand for  $\sim 10 \text{ ms}$  before its size differs more than 5% from a free expanding cloud. This should be compared with the case where the magnetic field curvature hasn't been compensated, in which a difference of 5% in size occurs already within  $\sim 1 \text{ ms}$  after turning off the optical dipole trap. Compensating the magnetic field allows carrying out time-of-flight studies to better determine the atomic sample temperature.

#### 4.10.2 Nufern Amplifier Trap

The dipole trap described in Section 4.6 results from a composite beam made out of an  $80 \mu\text{m}$  beam produced by an IPG laser and a  $270 \mu\text{m}$  generated with a Nufern amplifier. However, the Nufern trap was only recently added into the system and at the time of writing it has not yet been tested.

Once atoms are successfully loaded into this trap it is necessary to characterise it. Mainly, to measure the trap's frequency. Furthermore, the procedure of loading this trap would require optimisation. Additionally, the process of producing a caesium BEC using a dimple trap may be explored.

#### 4.10.3 Improving the Loading of the Dipole Trap

Evaporative cooling is a very efficient technique for increasing the phase-space density of an atomic cloud. For each order of magnitude lost in atom number, three orders or magnitude are gained in phase space density (see Section 5.3.3). Therefore, lossless cooling methods, that rely on off-resonant photon scattering, are an attractive prospect since they would allow to load more and colder atoms into the dipole trap. Consequently, larger and purer degenerate gases could be obtained.

For caesium, an often-used method is called resolved-sideband Raman cooling [74–77]. For this scheme, atoms are first loaded into an optical lattice. The

harmonic motion modulates the transition frequency and produces sidebands, the separation of which is determined by the harmonic oscillator frequency. However, the potential wells created by the optical lattice are tight enough that these sidebands can be resolved. Therefore, it is possible to optically drive a transition between vibrational states and in this way pump the atoms towards the ground state of the wells.

A major part of this scheme is already in place and caesium atoms have been successfully loaded into the Raman cooling lattice. However, at that time, caesium atoms were obtained from dispensers in the experimental chamber which greatly limited the lifetime of atoms in the lattice. Now, with a working caesium Zeeman slower it is possible to hold the atoms for longer times and take the implementation of this scheme to its conclusion.

Further optical cooling of lithium could also be implemented. It has been recently demonstrated in other labs using two different methods described below. The first one exploits a UV transition whose linewidth is seven times narrower than the typically used transition [78]. This lower linewidth results in a significantly lower Doppler temperature. The second method is based on the combined effect of a gray molasses, working on the  $D_1$  transition, and velocity-selective coherent population trapping in a Lambda-type three-level system [79–81]. The latter has the advantage that the same type of light sources that are already used in the experiment would be suitable as opposed to using a more expensive UV laser which would also require special optical components and vacuum windows.

## CHAPTER 5

# Experimental Scheme

The experimental sequence, and rationale behind it, used to produce ultracold samples of caesium-133 and lithium-6 is described in this chapter. Through most of the construction of this experiment, the techniques for each of the atomic species have been developed in parallel. This experiment has been advanced into a stage where degenerate quantum gases of lithium can be created. Additionally, high magnetic fields are generated around the atomic sample to control the scattering length of the  $|F = 1/2, m_F = 1/2\rangle$  and  $|F = 1/2, m_F = -1/2\rangle$  states of lithium. This results in a system which can realise both a Bose-Einstein condensate (BEC) and a Fermi gas, including the crossover. Caesium has been loaded into an optical dipole trap at high phase-space density and the system is ready to pursue evaporative cooling towards quantum degeneracy. Also, the low temperatures reached with both species allows us to begin the pursuit of ultracold mixtures.

Lithium is first obtained from an effusive oven and decelerated with a Zeeman slower to be captured by the magneto-optical trap (MOT) as described in Section 5.1. This continuous loading process is carried out until enough atoms have been gathered. An optical dipole trap is overlapped with the atomic cloud. At the same time the MOT parameters are adjusted to minimise the temperature and maximise the density to optimally load the dipole trap [82]. At the end of this phase, the atoms are optically pumped to produce a balanced mixture of the  $|F = 1/2, m_F = -1/2\rangle$  and  $|F = 1/2, m_F = 1/2\rangle$  states. The process of cooling and transfer into the dipole trap is described in Section 5.2. At this point the MOT has been turned off and the atoms are solely contained by the optical dipole trap. Evaporative cooling is performed on these atoms by decreasing the depth of the trap. For this cooling process, the strength of interactions between the atoms is controlled using a Feshbach resonance. The scheme used for evaporative cooling

is detailed in Section 5.3. This process is carried out until quantum degeneracy is reached. The observation and characterisation of a Bose-Einstein condensate are discussed in Section 5.4.

The scheme for caesium begins with a dispenser-fed oven from which hot atoms are obtained. The atoms travel through a Zeeman slower which allows them to be captured by a MOT as described in Section 5.1. The number of captured atoms saturates within a couple of seconds after which the transfer into the dipole trap begins. This transfer consists of using an optical molasses to sub-Doppler cool the caesium cloud into the optical dipole trap. After turning off the sub-Doppler cooling light, the atoms are optically pumped to the lowest hyperfine state  $|F = 3, m_F = 3\rangle$  to avoid inelastic collisions. The transfer into the dipole trap and optical pumping stage are detailed in Section 5.2.

## 5.1 Zeeman Slower and MOT Loading

The MOT light is aligned by placing irises in the optical fibre out-couplers and using paper templates with 1 mm pinholes on both sides of the chamber. This ensures that all of the beams cross at the centre of the vacuum chamber. Slight, intentional misalignment of the return beams can lead to an increase of 15% of atoms in the trap. However, this process leads to instabilities in the MOT number and keeping the beams aligned proved to result in a more reliable and repeatable method for transferring the atoms into the dipole trap.

The aim at the beginning of the experimental sequence is to gather a high number of atoms into the MOT. This is to be done while avoiding an increase of the overall pressure in the experimental chamber. Also, the duration of the experimental cycle should be kept to a comfortable length that permits multiple repetitions to be carried out in a short amount of time.

Once atoms are successfully loaded from the Zeeman slower into the MOT, several steps of optimisation can take place. The performance of the slower has been improved by using the MOT loading rate as a figure of merit. In this manner, the slower light power, slower re-pumper light power and magnetic field in the slower were adjusted to find the best values to operate on. Figure 5.1 shows the behaviour of the slower for both lithium and caesium while varying the slower light power.

With the atomic source adjusted, the next step is to find the operation parameters for the MOT. With this in mind, the detuning of the light and

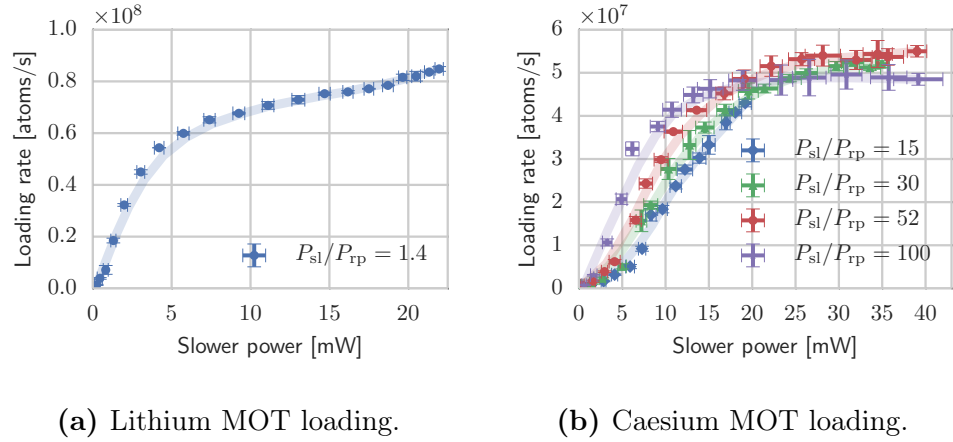
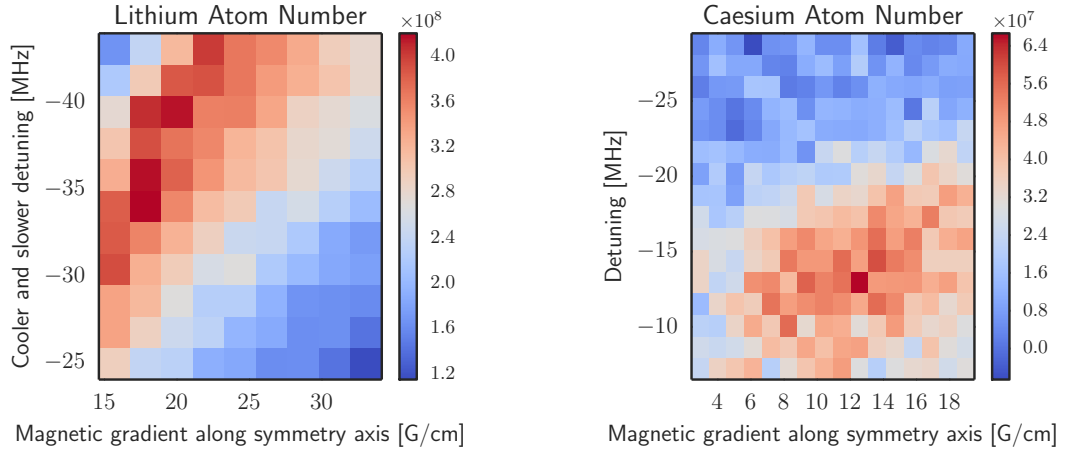


**Figure 5.1:** Rate of loading atoms into the MOT as a function of slower light power for both species. The parameter  $P_{sl}/P_{rp}$  is the ratio of power of slowing and re-pumping light. The optical setup for caesium allows to vary this ratio so different ratios are explored. Error bars show the statistical standard deviation. The shown lines are moving averages added as a guide to the eye.

magnetic field gradient around the MOT's position are adjusted to optimise the number of captured atoms. The measurements summarised in Figure 5.2 show the behaviour of the number of atoms captured in the MOT as a function of these parameters. The measurements for each of the species are qualitatively different because the experimental parameters were varied in different ways. For the caesium measurement, the MOT was loaded from dispensers next to the chamber so that it could be optimised independently of the Zeeman slower's performance. In contrast, lithium atoms are loaded via the Zeeman slower and, the lithium optical setup is arranged in such a way that when the MOT detuning is changed, the detuning of the slower light also changes accordingly. From this analysis, a detuning of -40 MHz (-6.8 $\Gamma$ ) and axial magnetic gradient of 20 G cm $^{-1}$  are concluded to be optimal loading parameters for the lithium MOT. The optimal caesium loading values are a -15.5 MHz (-2.9 $\Gamma$ ) for the detuning and 12.5 G cm $^{-1}$  for the axial magnetic gradient.

With both the slower and the MOT adjusted, a typical experimental cycle begins by loading either caesium for 2 s to 5 s or lithium for 5 s to 10 s. The growth of the number of captured atoms during the loading process is shown in Figure 5.3.

Usually, the lithium MOT is not loaded to saturation because an increase in the number of atoms in the MOT does not lead to an increase in the atoms loaded into the dipole trap. This fact is illustrated in Figure 5.4 where the number of



- (a) Lithium loading. Atoms are loaded from Zeeman slower. The detuning of the cooling, repumping and slowing light are varied in parallel for various magnetic gradients.
- (b) Caesium loading. The detuning of the cooling light and the magnetic gradient are varied. Atoms are loaded from dispensers next to the experimental chamber.

**Figure 5.2:** Number of atoms loaded into the MOT measured with absorption imaging for various MOT parameters.

atoms loaded into the dipole trap is plotted against MOT loading time. The reason for this is that the maximum achievable density in the MOT is limited. This limit arises because spontaneously emitted photons from the atoms in the MOT get re-absorbed by other atoms, resulting in an effective repulsive force between them which increases as the density becomes larger [83].

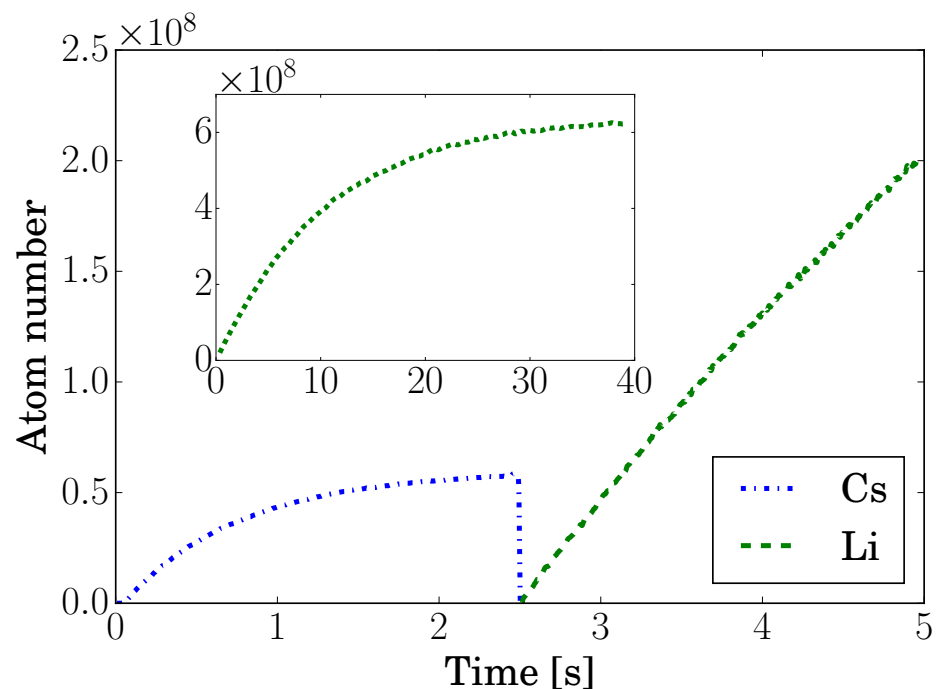


**Figure 5.3:** Sequential loading of a caesium and lithium MOT. Atom number from calibrated photodiode signal. Between 0 s and 2.5 s the cesium MOT is loaded. Between 2.5 s and 5 s a lithium MOT is loaded. The curves shown are the average of 6 measured traces. The inset shows a lithium loading curve measured over a longer time showing the saturation of the MOT.

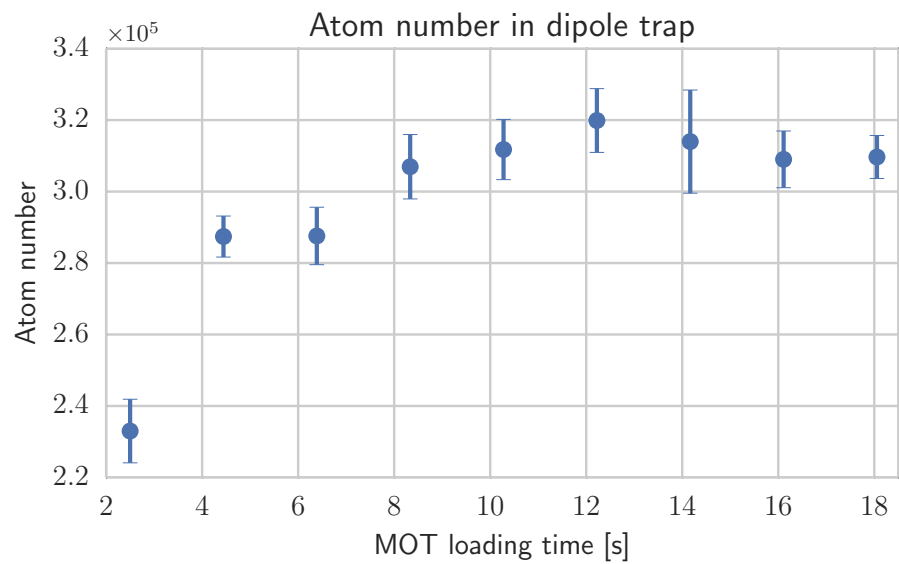


**Figure 5.4:** Number of lithium atoms loaded into the dipole trap for various MOT loading times, an upper bound in the density of the MOT causes the curve to saturate within 12 s even though the MOT is still increasing in number.

## 5.2 MOT Cooling and Transfer Into Dipole Trap

In the initial section of the experimental sequence, the MOT parameters are adjusted to maximise the collection of atoms into the trap. However, these values for optimal loading will not result in the coldest nor most dense cloud. In the following step, the magnetic gradient and light detunings are varied to increase the phase-space density as much as possible and thus, enhance the transfer into the dipole trap. This step is significantly different for lithium and caesium. For caesium, sub-Doppler cooling mechanisms take place while for lithium, the excited  $^2P_{3/2}$  levels overlap (see Figure 2.1) prevents these mechanisms from working [58].

As atoms are transferred into the optical dipole trap, they are optically pumped. Caesium atoms are pumped into the  $|F = 3, m_F = 3\rangle$  and  $|F = 3, m_F = 2\rangle$  states and eventually only to the  $|F = 3, m_F = 3\rangle$  to avoid inelastic collisions. Lithium atoms are pumped to an equal mixture of the  $|F = 1/2, m_F = 1/2\rangle$  and  $|F = 1/2, m_F = -1/2\rangle$  states. For lithium, a mixture of states is required because collisions, necessary for evaporative cooling, are suppressed for fermions in the same state. An overview of the timing used for caesium and lithium at this stage is shown in Figure 5.5 and Figure 5.6 respectively.

### 5.2.1 Compression and Optical Molasses

The lowest achievable temperature for lithium in the MOT is limited by its Doppler temperature which is  $T_D^{\text{Li}} = 141 \mu\text{K}$  as calculated by Equation 3.4. This temperature is reached when the detuning is  $\delta = -\Gamma/2$ , where  $\Gamma$  is the transition's line width. For this reason, after loading the MOT, the detuning is changed from  $-40 \text{ MHz} (-6.8\Gamma)$  to  $-2.9 \text{ MHz} (-0.5\Gamma)$  within 11 ms. Through this process, the temperature of the sample drops from  $2000 \mu\text{K}$  to  $600 \mu\text{K}$ . The reason for this value being significantly higher than the theoretical  $T_D^{\text{Li}}$  has to do with the fact that this temperature was calculated with a two-level atom approximation and using only the linewidth of the  $F = 3/2 \rightarrow F' = 5/2$  transition. In reality, all the states in the  $^2P_{3/2}$  are overlapped and a much larger linewidth should be considered. A Doppler temperature of  $270 \mu\text{K}$  results if the linewidth obtained from the measurement shown in Figure 5.20 is used.

The process with caesium is phenomenologically different since  $\sigma^+ - \sigma^-$  sub-Doppler cooling takes place (see Subsection 3.2.1). To enhance this mechanism at the end of the MOT-loading phase, the detuning is linearly increased within

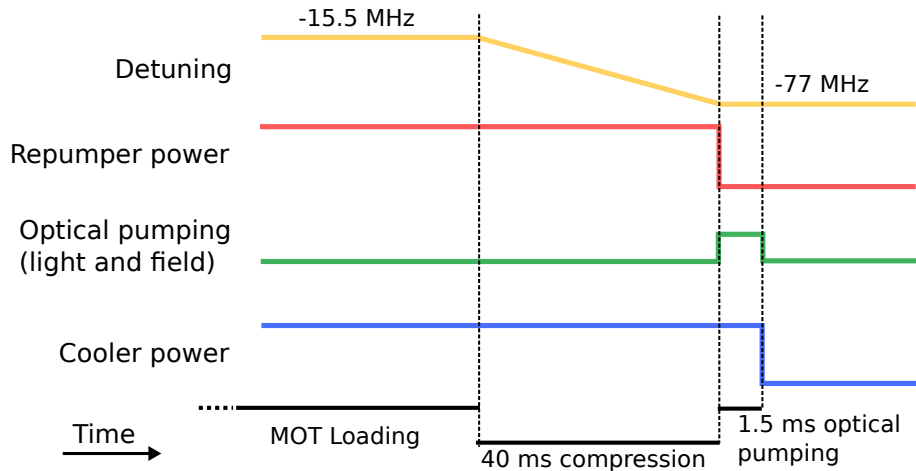


**Figure 5.5:** Timing sequence for transferring caesium atoms into the optical dipole trap. The detuning is increased to enhance sub-Doppler cooling and are optically pumped afterwards. The dipole trap is constantly on during this process.

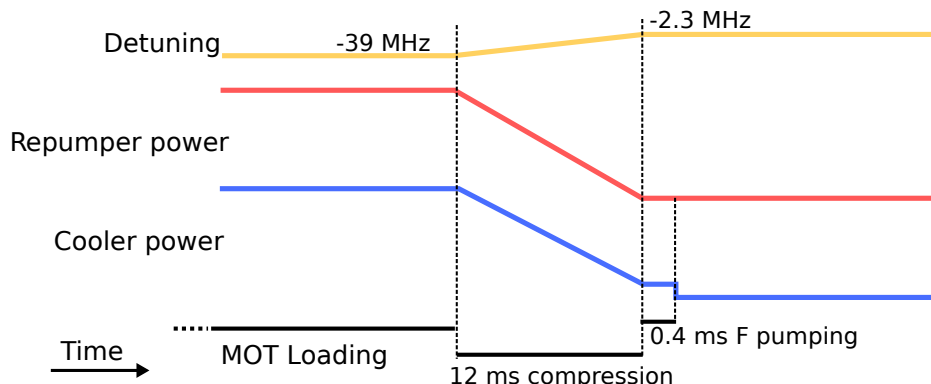


**Figure 5.6:** Timing sequence for transferring lithium atoms into the optical dipole trap. The detuning is decreased while simultaneously decreasing the cooling and repumping power to minimise the Doppler cooling temperature. After, the atoms are pumped to the  $F = 1/2$  ground state. The dipole trap is constantly on during this process.

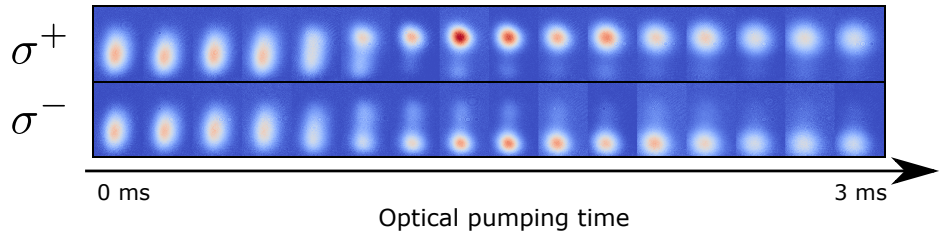


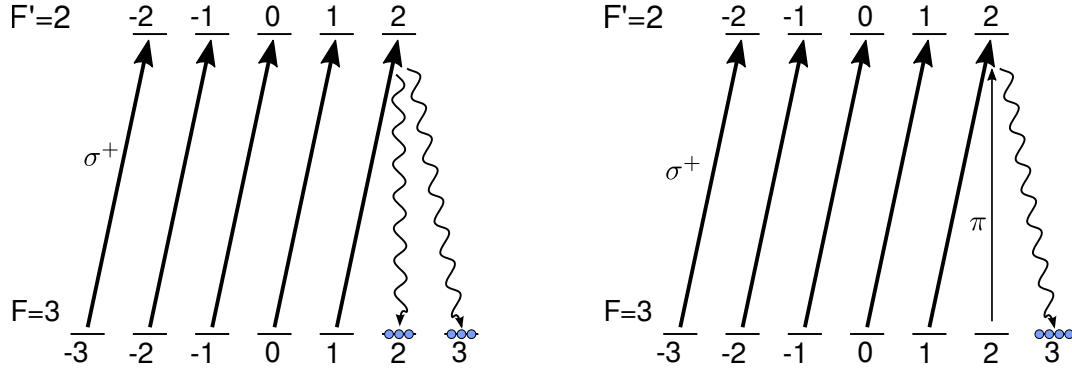
**Figure 5.7:** Optical pumping of caesium. Several density measurements are shown after 14 ms time of flight. A vertical magnetic gradient is present during the flight which applies a state-dependent force on the atoms. For each column, the time that the optical pumping light is on is different, increasing in duration towards the right side. The top and bottom rows of images correspond to two different polarisations of pumping light.

75 ms to -77 MHz (-14.7 $\Gamma$ ) which is the largest detuning possible with the present locking scheme. At the same time the magnetic field gradient is decreased down to zero. The time scale of the cooling mechanism is determined by the photon scattering rate. However, the magnetic fields are ramped much slower than this to avoid generating eddy currents that would distort the atomic cloud. With this process, temperatures of 16  $\mu\text{K}$  are routinely achieved [36].

It is worth noting that the dipole trap is a conservative trap and a free atom that enters the trap would promptly leave it, keeping the same kinetic energy it had initially. Thus, the mere presence of the trap in a region of space will not capture the atoms that fly through it. Only atoms that have a low enough energy and are at the location of the trap when the light is turned on are captured if there is no dissipation mechanism. However, this mechanism can be provided by the MOT light to increase the number of loaded atoms [84].

### 5.2.2 State Preparation

As the atoms are loaded into the dipole trap, it is important that they are in the lowest energy state to avoid inelastic collisions which would cause heating and loss of atoms. For caesium, this is particularly important since it has a giant spin relaxation coefficient [85]. In a Cs-Cs collision where spin relaxation occurs and the state of one or both of the atoms changes from  $F = 4$  to  $F = 3$ , the energy released is at least  $\Delta E = h \times 9.2 \text{ GHz} = k_B 441 \mu\text{K}$ . For this reason, it is not possible to magnetically trap caesium for long times since all the magnetically trappable states have a high rate of spin-changing collisions [86]. Therefore in



(a) Partial optical pumping is achieved using  $\sigma^+$  light.

(b) Adding a weak  $\pi$  component atoms accumulate in  $|F = 3, m_F = 3\rangle$ .

**Figure 5.8:** Optical pumping scheme for caesium using the  $F = 3 \rightarrow F' = 2$  transition.

order to cool caesium into quantum degeneracy, optical confinement is necessary since it only depends very weakly on the internal state of the atoms and allows trapping them in their absolute ground state.

Inelastic collisions of caesium atoms are avoided by optically pumping them to the lowest hyperfine state  $|F = 3, m_F = 3\rangle$ . As mentioned before, for the final MOT cooling process, the magnetic quadrupole field is turned off. For state preparation, a homogeneous bias magnetic field of 1 G is turned on for 1.5 ms to define a quantization axis. This field is parallel to the optical pumping light and it is produced using a pair from the set of offset coils (see Section 4.3). At the same time, 1 mW of  $\sigma^+$  polarized light which is -10 MHz detuned from the  $F = 3 \rightarrow F' = 2$  transition is shone on the atoms. Optical pumping with this light causes an accumulation in the  $|F = 3, m_F = 3\rangle$  and  $|F = 3, m_F = 2\rangle$  states as depicted in Figure 5.8a. The degree of polarisation is analysed using a Stern-Gerlach technique. Applying a vertical magnetic gradient during time of flight, the atoms are pushed up or down depending on the internal state. Figure 5.7 shows qualitatively the effect of optical pumping for two different polarisations of the pumping light. This detection technique is limited by the temperature of the atoms and the speed at which the magnetic fields can be changed. It is worth noting, however, that this speed does not only depend on the inductance of the coils and the capability of the power supply but also is affected by eddy currents that are induced in the stainless steel experimental chamber. For this

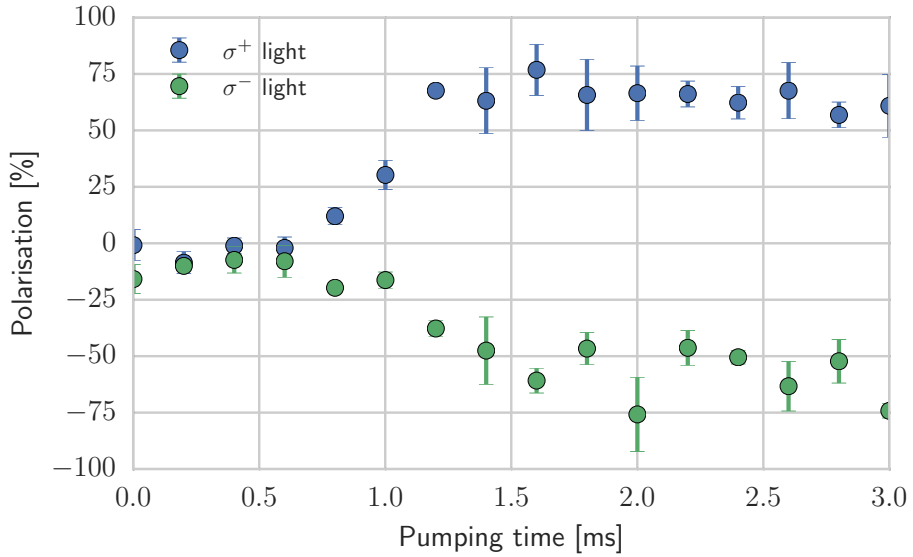


**Figure 5.9:** Optical pumping of caesium atoms using two different polarisations of pumping light. Measuring the number of atoms in the upper ( $N_U$ ) and lower ( $N_L$ ) halves, and the total atom number ( $N_T$ ), the degree of polarisation is defined as  $p = \frac{N_U - N_L}{N_T}$ . The results shown in this figure are obtained with the data displayed in Figure 5.7. Error bars show the standard deviation calculated using three measurements for each point.

measurement, a gradient of  $\approx 150 \text{ G cm}^{-1}$  was used during the first 3 ms of a total time of flight of 14 ms. These values were chosen so that the largest gradient could be applied whilst allowing the magnetic field to subside before absorption imaging takes place.

The detection method used cannot resolve the  $m_F$  states individually. Nonetheless, we can quantify the degree of polarisation by counting the number of atoms that are shifted in one direction relative to the total number of atoms. The results of this analysis are shown in Figure 5.9. After implementing evaporative cooling of caesium, lower temperatures will be achieved which would allow resolving the different states and fine tune the pumping parameters. Currently, 75% of the atoms are pumped to the desired state within 1.6 ms.

There are several advantages to using the  $F = 3 \rightarrow F' = 2$  transition for optical pumping. Firstly, since the  $F' = 2 \rightarrow F = 4$  decay is dipole-forbidden, fewer atoms would fall into the  $F = 4$  ground state, which then require being pumped back to the  $F = 3$  ground state resulting in an overall heating of the sample. Secondly, by rotating the magnetic field with respect to the pumping beam, a small

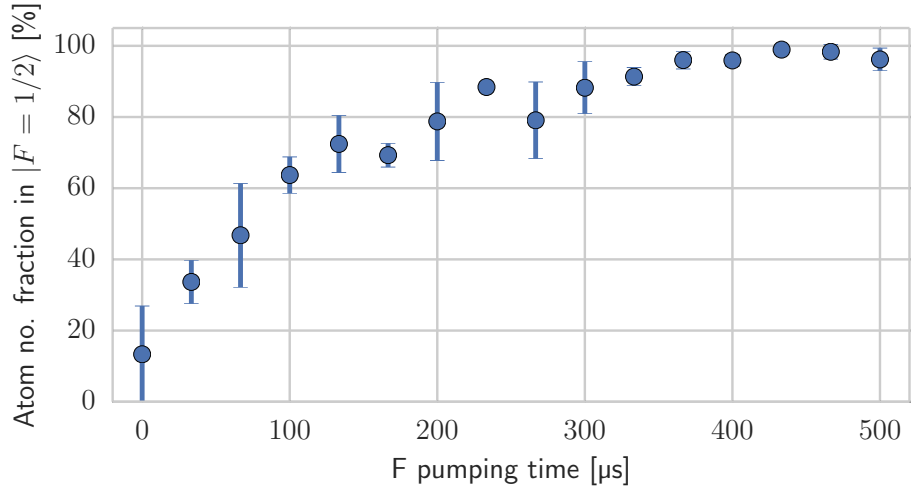


**Figure 5.10:** Pumping efficiency of lithium into the  $F = 1/2$  state. Optical pumping is carried out by switching off the cooler beam for a varying amount of time. The number of atoms in this manifold is obtained by first carrying out absorption imaging without using any re-pumping light to obtain the number of remaining atoms in the  $F = 3/2$  ground state manifold. The total atom number is then measured with re-pumper on. The difference gives the amount of atoms in the  $F = 1/2$  state.

$\pi$ -polarised component is added which couples to the  $|F = 3, m_F = 2\rangle$  making it no longer a dark state. Therefore, all atoms accumulate in the  $|F = 3, m_F = 3\rangle$  states as shown in Figure 5.8b. Having a weak  $\pi$ -component is beneficial for implementing Raman sideband cooling since it suppresses reabsorption heating in the final stages of cooling where it is most critical [76].

Optical pumping is carried out differently for lithium. Low-temperature collisions of fermionic particles in the same state are suppressed due to Pauli's exclusion principle [87]. However, collisions are necessary for evaporative cooling and therefore, an equal mixture of atoms in the two lowest energy states  $|F = 1/2, m_F = 1/2\rangle$  and  $|F = 1/2, m_F = -1/2\rangle$  is prepared. This is achieved by turning off the re-pumping light before the cooling light during the process in which the MOT light is extinguished and the dipole trap is loaded. This time interval is called *F pumping time* in the plot shown in Figure 5.10. In this figure, the fraction of atoms in the  $F = 1/2$  manifold is measured as a function of the pumping time. This pumping process is very effective and leads to more than 95% of the atoms in the  $F = 1/2$  groundstate manifold within 400  $\mu$ s. Using high-field imaging, described in Section 4.8.1, the different hyperfine states of lithium can be resolved. With this system, it can be verified from the relative height of the

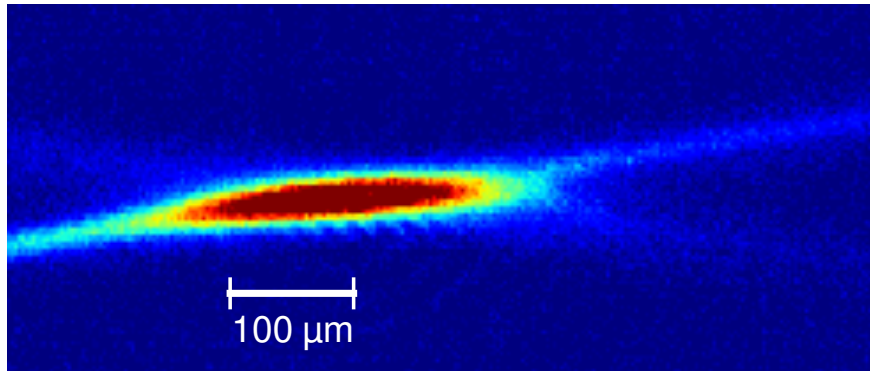


**Figure 5.11:** Absorption image of an equal mixture of lithium atoms in the  $|F = 1/2, m_F = 1/2\rangle$  and  $|F = 1/2, m_F = -1/2\rangle$  states loaded into the crossed optical dipole trap. This image was taken after 500 ms of plain evaporation at 700 G with the IPG dipole trap operating at full power (100 W). The number of atoms in the crossing region is  $4 \times 10^5$  at a temperature of  $\approx 150 \mu\text{K}$ . The Rayleigh length of the dipole trap beams is about 2 cm so there are atoms trapped in the beams for a distance much further than what is shown in this image. However, the majority of the atoms occupy this region close to the crossing of the beams.

peaks in Figure 4.29 that the mixture that results from this pumping process is fairly balanced having a 53 : 47 ratio between the population of the  $m_F = 1/2$  and  $m_F = -1/2$  substates.

In this section the transition process from loading a MOT to cooling and state-preparing them while transferring into an optical dipole trap has been discussed. The atoms loaded into the dipole trap can be measured through absorption imaging. As a result,  $2 \times 10^6$  caesium atoms and  $6 \times 10^5$  lithium atoms have been loaded into this trap. Figure 5.11 shows lithium atoms in the trap after loading. The structure of the crossed dipole trap is clearly visible.

## 5.3 Evaporative Cooling of Lithium

### 5.3.1 Scattering Cross-Section

Given the crucial role that elastic collisions play in the evaporative cooling process (see Section 3.4), it is at this point that controlling the scattering properties through Feshbach resonances starts to become important. In the following, a balanced mixture of lithium in the  $|F = 1/2, m_F = 1/2\rangle$  and  $|F = 1/2, m_F = -1/2\rangle$  states has been loaded into the dipole trap and the scattering length of atoms in these

two states will be controlled. However, even though a Feshbach resonance allows to set any arbitrary scattering length, it will be shown below that this does not imply that the cross-section can be controlled arbitrarily but rather, it has an upper bound determined by the kinetic energy. At high temperatures, the maximum achievable scattering cross-section is bounded and the exact magnetic field value is not that important. At low temperatures, the scattering-cross section can be varied by 10 orders of magnitude as shown in Figure 5.12.

Lithium atoms in the  $|F = 1/2, m_F = 1/2\rangle$  and  $|F = 1/2, m_F = -1/2\rangle$  states are distinguishable from each other and their s-wave scattering cross-section is given by Equation 2.10 and reproduced here

$$\sigma = \frac{4\pi a^2}{1 + a^2 k^2}. \quad (5.1)$$

This equation is valid as long as the particle's kinetic energy is small compared to the height of the centrifugal barrier. For  $p$ -wave collisions of lithium-6, this height is 8 mK. This is much higher than the atoms' temperature in the dipole trap which is always below 1 mK (see Section 2.4).

For a given value of the wave number  $k$ , the scattering cross-section has an upper bound, when  $a \rightarrow \infty$ , given by

$$\sigma_{\max} = \frac{4\pi}{k^2},$$

known as the unitarity-limited scattering cross-section. This means that for  $k \gg 1/a$ ,  $\sigma_{\max}$  is an upper bound for the scattering cross-section. Figure 5.12 illustrates how as the temperature decreases below 10  $\mu\text{K}$ , the enhancement of the cross-section close to the Feshbach resonance starts to become important.

However, there is no lower bound to the scattering cross-section and when the scattering length approaches zero, the cross-section becomes zero as well. As a result, it is much easier to observe the zero-crossing of the scattering length, caused by the presence of a nearby Feshbach resonance, than to observe the resonance itself [88]. This feature is exploited for the measurement summarised in Figure 5.13 where the zero-crossing is clearly observed. This measurement consists of transferring the atoms into the dipole trap and holding them for five seconds at various values of the magnetic field. After this, the number of remaining atoms is measured using fluorescence imaging with a field of view large enough to ensure that also the atoms in the wings of the trap are detected. The finite

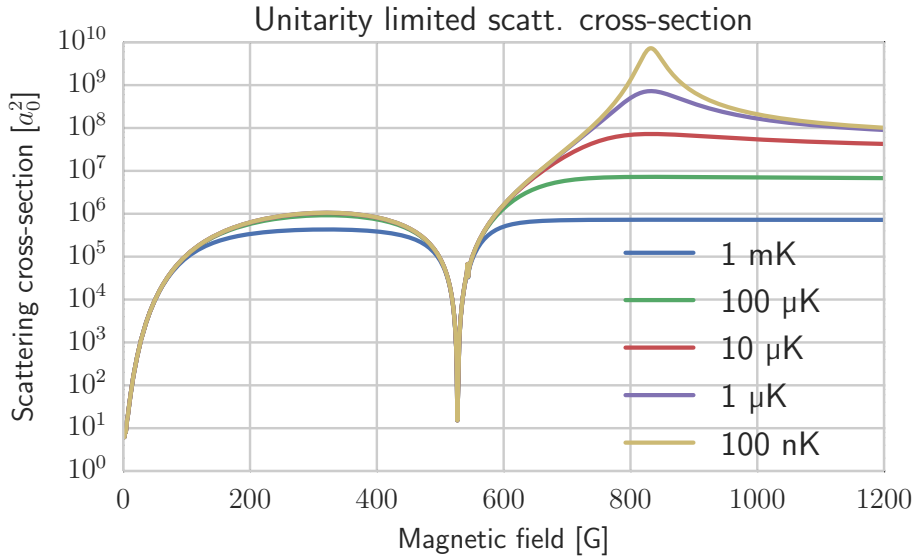


**Figure 5.12:** Unitarity limited scattering cross section calculated using Equation 5.1 for the most probable  $k$  at various temperatures. The scattering length was obtained from [26].

depth of the dipole trapping potential allows for the most energetic atoms to escape. Afterwards, through elastic collisions, the energy is redistributed among the atoms; those which attain enough energy leave the trap whilst decreasing the energy per particle of the remaining atoms. If instead, elastic collisions are suppressed, this prevents the redistribution from happening, thus the mechanism for atoms to get enough energy to leave the trap is removed. In this way, the zero-crossing of the scattering length produces a peak in the figure.

### 5.3.2 Plain Evaporation

The previously described process with constant trap depth through which interacting atoms leave the trap is called *plain evaporative cooling*. This is advantageous as it removes the most energetic atoms without the need of decreasing the depth of the trap. The ability to adjust the scattering cross-section allows us to enhance or inhibit this mechanism. A comparison of this process with and without elastic collisions is shown in Figure 5.14 demonstrating the cooling effect of the collisions. Here, the evaporation rate depends strongly on the truncation parameter (see Section 3.4). It is worth noting that, as made evident by Figures 5.12 and 5.14, a magnetic field of several hundreds of gauss is necessary to initiate evaporative cooling for lithium. However, as the cloud's temperature is several hundreds of

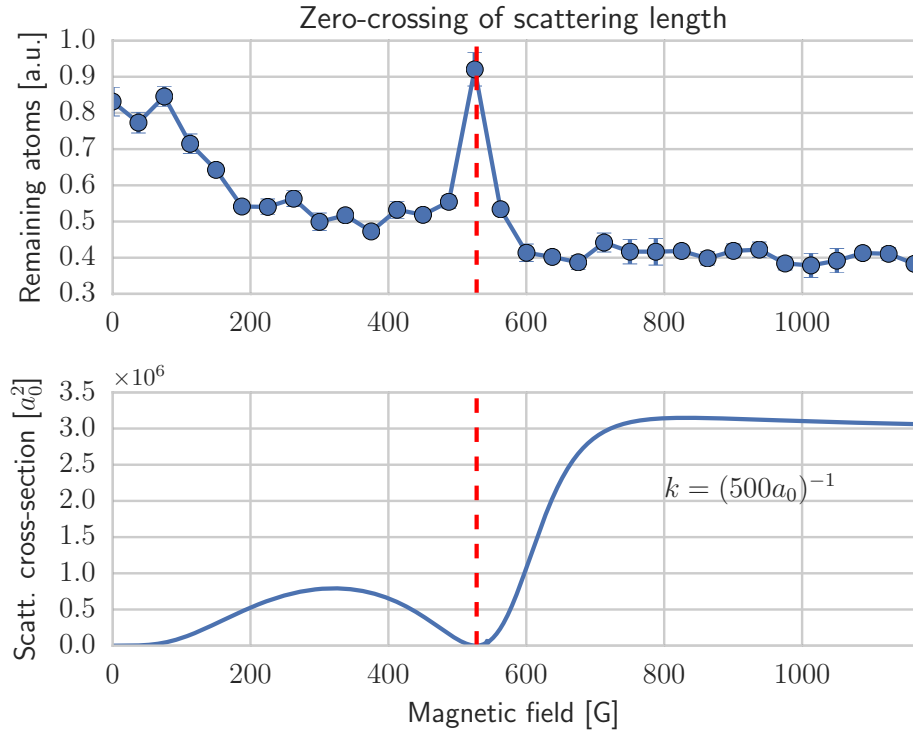


**Figure 5.13:** Zero-crossing of scattering length measured through plain evaporation. Top plot shows the measured number of remaining atoms after holding them in the dipole trap at maximum power (100 W) for 5 s at various magnetic fields. During this process their temperature changes from  $\approx 250 \mu\text{K}$  to  $\approx 100 \mu\text{K}$ . Bottom plot shows the corresponding unitarity-limited scattering cross-section using the expected value of the scattering length obtained from [26] and an average  $k$  that is consistent with a temperature of  $230 \mu\text{K}$ . Each point is measured three times and the error bars show the statistical standard error.

micro kelvin, the specific value of the scattering length is not important (see Figure 5.12). Usually, a bias magnetic field with values between 700 G and 850 G is used during plain evaporation and is kept throughout most of the evaporation process.

A non-interacting trapped gas is only expected to lose atoms due to collisions with energetic non-trapped particles from the background gas, known as “one-body losses”. Whereas interacting particles have additional loss mechanisms. The apparent, more rapid loss of non-interacting particles during the evaporation in Figure 5.14 seemly contradicts this. An important detail is that the greater loss of non-interacting particles only happens when measuring the number of atoms in the crossed region; counting the atoms throughout the beams gives the expected

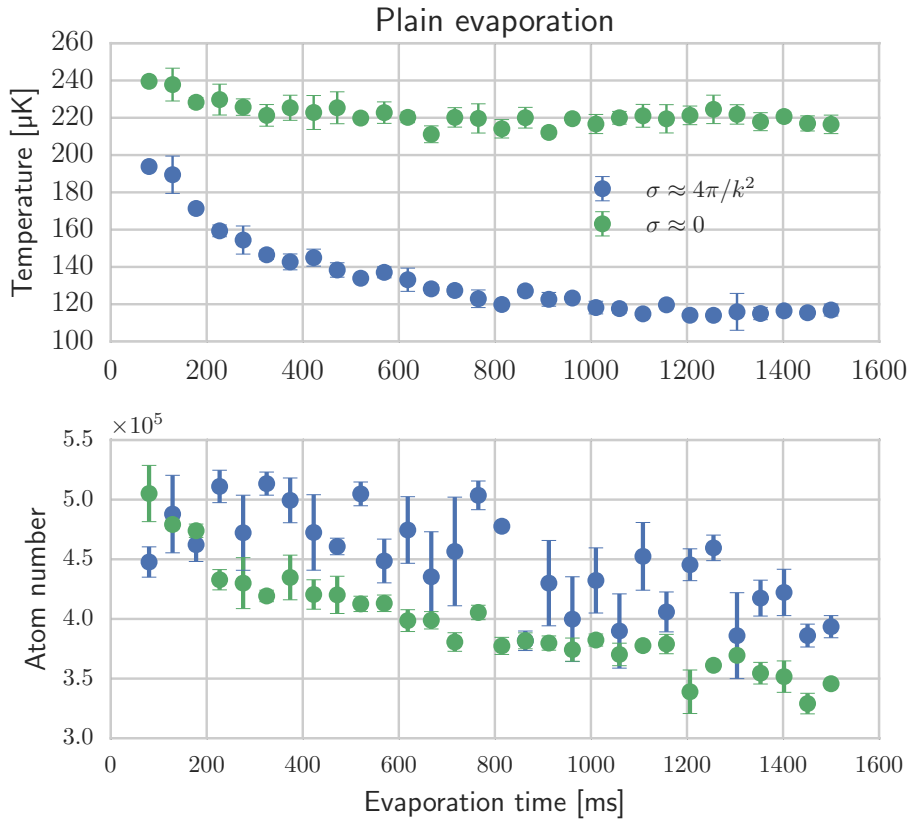


**Figure 5.14:** Temperature and atom number during plain evaporation of lithium for different scattering cross-sections. Scattering length is set to  $10^4 a_0$  and  $0 a_0$  at 698 G and 528 G respectively. The trap depth is 1 mK and plain evaporation approaches stagnation when a truncation factor of  $\eta \approx 9$  is reached. For this measurement only atoms close to the region where the beams of the dipole trap are crossed, as in Figure 5.11, are counted. As atoms from the wings of the dipole trap evaporate, the remaining ones descend into the crossed region and thus, replenish it. Therefore, a faster decay is observed when evaporation doesn't occur.

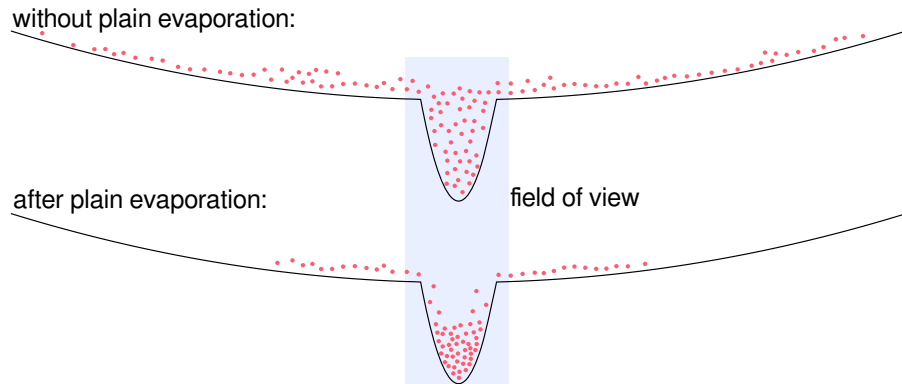


**Figure 5.15:** Replenishment of atoms at the centre of the trap during plain evaporation. During plain evaporation, atoms in the wings of the trap fall into the centre. Only the blue region is within the field of view and therefore, even though there are fewer total atoms after evaporation, the number of detected atoms does not decrease.

result (see Figure 5.13). The explanation for this discrepancy is illustrated in Figure 5.15. As the atoms in the wings collide and get cooled down they descend towards the region where the dipole beams cross, thus, replenishing the atoms there. That is, the trap wings act as a reservoir to the dimple created in the crossing region.

### 5.3.3 Forced Evaporation

The process of plain evaporation decreases the ensemble's temperature which in turn, makes it less likely for an atom attain enough energy to leave the trap and therefore, the evaporation rate decreases. This can be quantitatively understood by considering the truncation parameter  $\eta = U/k_B T$  and recalling that the evaporation rate is proportional to  $\eta e^{-\eta}$  (see Section 3.4). It can be seen in Figure 5.14, that once the temperature reaches a value of  $115 \mu\text{K}$ , corresponding to a truncation parameter of  $\eta \approx 9$ , plain evaporation stagnates. In order to lower the temperature further, it is thus necessary to carry out forced evaporation by lowering the depth of the trap. This is done by decreasing the power in the dipole laser which, as consequence, decreases the trap's frequency and thus, the atoms' collision rate. Nonetheless, this is not a problem since the tight dipole trap has high frequencies from the start and, using a Feshbach resonance, the scattering cross-section is set to a value such that high scattering rates are achieved. In the case of lithium, the scattering length can be greatly increased without the risk

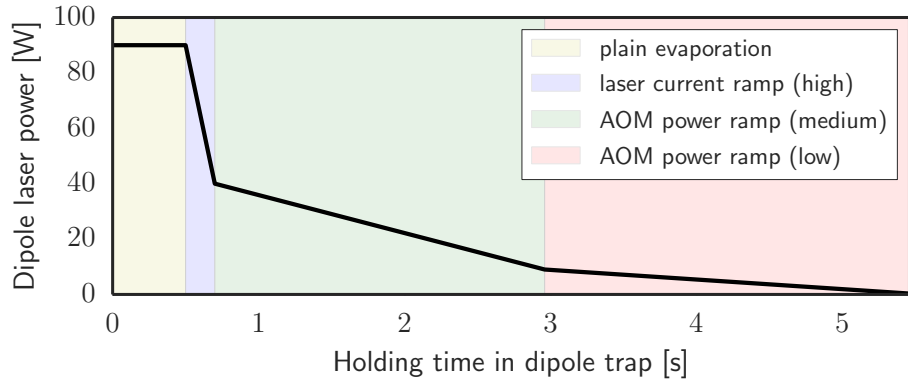


**Figure 5.16:** The power as a function of time in the optical dipole trap used for evaporation. In the *high* ramp, the laser's power is controlled by the input current. In the *medium* and *low* ramps, a feedback loop is used to control the power using an AOM.

of inducing three-body losses because these collisions are suppressed by Pauli's exclusion principle [87].

As detailed in Section 4.6, the intensity of the dipole trap light can be controlled by either changing the current of the IPG laser or by changing the diffracted power through the acousto-optical modulator (AOM). The evaporation ramp is depicted in Figure 5.16. The time scale at which the power should be decreased is dependent on the collision rate. When plain evaporation stagnates after roughly 500 ms (see Figure 5.14), the current of the laser is linearly decreased during 150 ms from the loading value down to 40 W. This value has to be chosen low enough to ensure that the photodiode of the feedback loop which controls the AOM has a suitable signal range, but high enough that the laser will operate stably. The following stage of evaporation is controlled by the dipole laser power stabilisation system and it consists of two linear ramps with a length of 2.2 s and 2.5 s respectively. As the trap depth is lowered the temperature also decreases accordingly. These three stages of forced evaporation are depicted in Figure 5.17. Throughout this process the truncation parameter  $\eta$  varies roughly between 7 and 10, when the evaporation is least and most efficient respectively. With these values, the phase-space density (PSD) increases by 3 orders of magnitude while the atom number only decreases by 1 order of magnitude, from  $10^6$  to  $10^5$ .

Evaporatively cooling lithium is a straightforward process because the unitarity regime can be accessed without significant three-body recombination losses. In unitarity, the energy dependent cross-section leads to a runaway evaporation

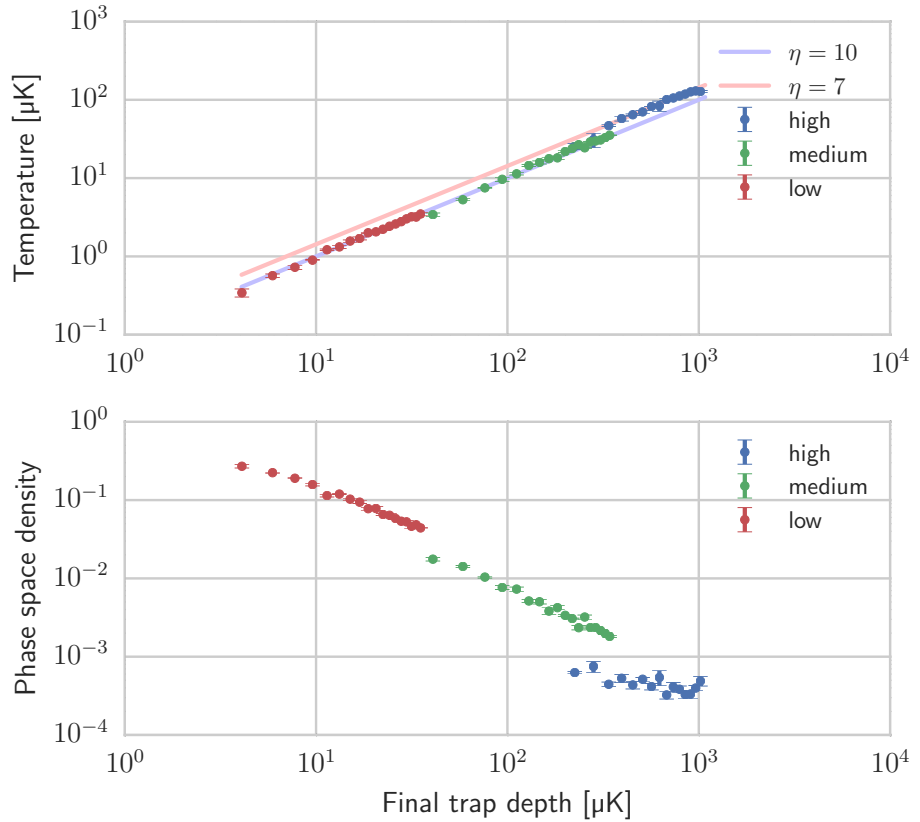


**Figure 5.17:** The three different stages of evaporation are shown. The color of the points match the color for the stages in Figure 5.16. The statistical error bars are contained within the data points. The temperature plot also shows a lines where  $\eta = U/k_B T = 7$  and  $\eta = 10$  for comparison.

regime. In contrast, with caesium these recombination losses are not suppressed and, in fact, scale with the scattering length  $a$  as  $a^4$  [89]. An alternative approach is to use a magnetic gradient to levitate the atoms out of the trap. In this method, the frequency of the trap remains constant and a runaway evaporation regime is also reached [90].

### 5.3.4 Feshbach Molecules

Feshbach molecules can be formed by two different methods. The first is by magneto-association, where a cold sample is held in the trap while the magnetic field is swept across a resonance [49, 91]. An alternative method, which is employed in this work, is to keep the atoms at a fixed magnetic field where a molecular state exists. Then, a molecule is formed through a three-body collision which is

required to conserve energy and momentum in the process. Conversely, when a molecule collides with an atom, it may dissociate into individual atoms. Both processes take place simultaneously and for slow enough evaporation ramps, an atom-molecule equilibrium is reached [92]. The molecule-to-atom ratio is given by

$$\frac{N_{\text{mol}}}{N_{\text{at}}} = \phi_{\text{at}} e^{-E_b/k_B T}, \quad (5.2)$$

where  $E_b = \hbar^2/ma^2$  is the binding energy of the molecules,  $T$  is the temperature and  $\phi_{\text{at}}$  is the atomic phase-space density [92].

For evaporative cooling to continue after molecule formation takes place, it is necessary that a high collision rate is maintained. This rate is dependent on the trap frequency, the density and the molecule-molecule scattering length. The trap frequency is the same for the molecules as it is for the free atoms despite the mass being double because the polarisability of the molecules is also double [21]. The density of molecules is half of the atomic density. Finally, the molecule-molecule scattering length  $a_m$  is proportional to the atom-atom scattering length  $a$  and is given by [87]

$$a_m = 0.6a.$$

An important loss mechanism of Feshbach molecules occurs in an atom-molecule collision where a dimer collides with a particle and becomes more tightly bound. In such a collision the binding energy is converted into kinetic energy and the collision partners are lost from the trap. Nonetheless, following the analysis in [87] for a two-component mixture of fermions, which is the case of this work, these collisions are suppressed due to Pauli's exclusion principle. Thus, these results indicate that this system exhibits a remarkable stability as compared to its bosonic counterparts. While the fermionic suppression of three-body collisions inhibits the formation of tightly bound dimers through collisions, it does not limit the formation of Feshbach molecules through the same type of collisions. This is also analysed in [87] and, to understand why this happens, it is important to note that Feshbach molecules have a size on the order of the scattering length  $a$ . This length determines the distance the atoms need to approach each other for the collision to result in the formation of a Feshbach molecule. A deeply bound molecule on the other hand has a much smaller size  $R_d \ll a$  and the probability of three atoms being within this distance is reduced because of the exclusion principle by a factor proportional to a power of  $(R_d/a)$ .

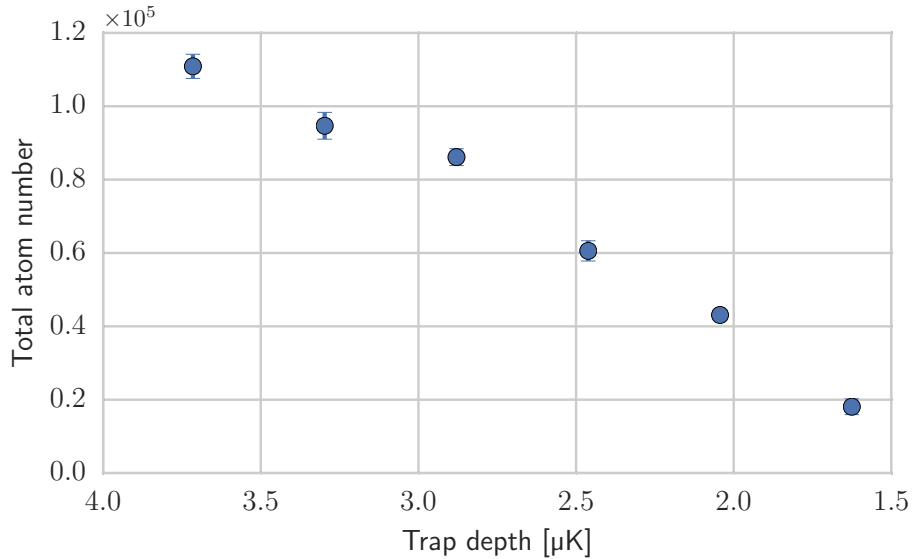


**Figure 5.18:** Total atom number as a function of trap depth during evaporative cooling. Atom number is measured using absorption imaging. Error bars represent the statistical standard error. Each point was measured 6 times.

## 5.4 Bose-Einstein Condensation

Pushing evaporative cooling further causes the molecular gas to undergo a phase transition in which a macroscopic occupation of the ground state of the confining potential occurs. Thus, the molecular gas can be understood as having a condensed fraction, containing all the atoms in the ground state, and a thermal one, comprising the rest. In this section, the process of condensation and properties of this gas are discussed.

### 5.4.1 Final Stage of Evaporation

The atom number as evaporation progresses is shown in Figure 5.18. This measurement includes both the condensed and thermal fractions and does not discriminate between pairs of atoms in a molecular state and single atoms. The behaviour is similar to previous evaporative cooling stages in that the atom number decreases linearly, in proportion to the trap depth.

The production of a Bose-Einstein condensate may be detected by observing a bi-modal distribution [16, 17]. However, as shown in the following subsections, strong interactions between the molecules decreases the contrast between the thermal and condensed fraction and hence, the visibility of the latter. A natural

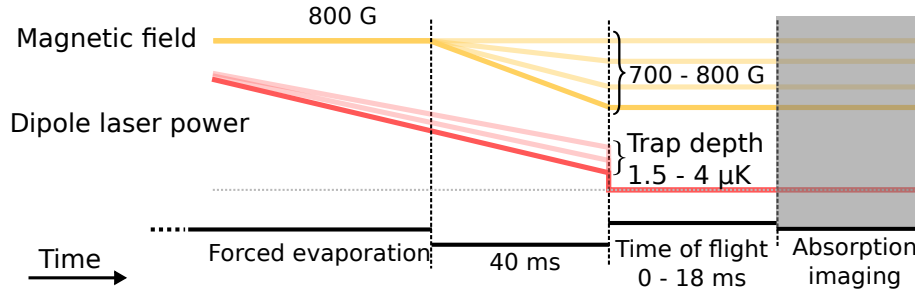


**Figure 5.19:** Timing during the final stage of evaporative cooling. The optical dipole trap is switched off at the end of evaporative cooling and imaged after some time of flight. Different values for the final trap depth and magnetic field have been used to vary the temperature and strength of interactions.

step towards better detection of the condensate would be to decrease the scattering length before release, in order to improve its visibility. However, decreasing the scattering length increases the binding energy of the Feshbach molecules according to  $E_b = \hbar^2/2ma^2$ , making imaging not possible. Thus, a compromise must be made between the contrast of the two fractions and the visibility of the individual atoms during imaging. Setting the magnetic field to 700 G ensures that the molecules can be imaged [93] while the two fractions can still be distinguished.

In the present scheme depicted in Figure 5.19, evaporative cooling has been carried out at 800 G after which, the magnetic field is changed to 700 G in order to make the bimodal distribution most apparent. The field is changed in a span of at least 40 ms, while the atoms are still held by the dipole trap, to ensure that no unwanted currents are excited in the vacuum chamber. As a result, the densities presented in Figure 5.20 are measured for final evaporation trap depths of 3.7 μK, 2.9 μK and 1.6 μK. For this figure, the optical dipole trap is extinguished and the atomic distribution is measured after 5 ms of time of flight, allowing for the bimodal distribution to become discernible. It clearly shows the emergence of a bimodal distribution with an almost pure BEC for the lowest depth of dipole trap of 1.6 μK.

To better analyse the presented results, the coming subsections describe the properties of a bosonic gas containing condensed and thermal fractions mostly following the theory presented in [64, 94]. It is followed by a more detailed discussion of the experimental results.

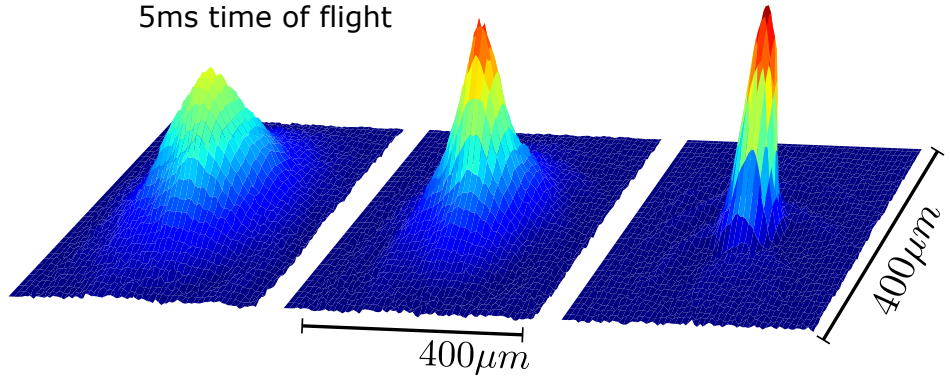


**Figure 5.20:** Density after time-of-flight at various stages of evaporation. Left: thermal gas above the transition. Middle: both thermal and condensate fractions are present. Right: virtually pure condensate.

### 5.4.2 In-trap Density

In the case of a non-interacting gas in a harmonic potential given by

$$V(\mathbf{r}) = \frac{1}{2}m(\omega_x^2x^2 + \omega_y^2y^2 + \omega_z^2z^2),$$

the condensed fraction density is given by the harmonic oscillator ground state wave function  $\psi_0(\mathbf{r}) = \left(\frac{m\omega_{\text{ho}}}{\pi\hbar}\right)^{3/4} \exp\left[-\frac{m}{2\hbar}(\omega_x x^2 + \omega_y y^2 + \omega_z z^2)\right]$  and the number of atoms in the ground state  $N_0$  by

$$n_0(\mathbf{r}) = N_0|\psi_0(\mathbf{r})|^2,$$

where  $\omega_{\text{ho}} = (\omega_x \omega_y \omega_z)^{1/3}$ . Thus, the distribution of particles of the condensed fraction has a Gaussian shape with a width determined by the oscillator length

$$a_{\text{ho}} = \sqrt{\frac{\hbar}{m\omega_{\text{ho}}}}.$$

It is worth noting that the size of a non-interacting condensate is independent of the number of atoms. The density of the thermal part can be found using the Bose-Einstein distribution and is given by

$$n_{\text{Th}}(\mathbf{r}) = \frac{1}{\lambda_T} g_{3/2}(e^{V(\mathbf{r})/k_B T}),$$

where  $g_{3/2}(z)$  is the polylogarithm function of order 3/2 [95], and the thermal wavelength is  $\lambda_T = \sqrt{2\pi\hbar^2/mk_B T}$ . The ratio of the square width of the thermal

and condensed part in the direction  $k = x, y, z$  is

$$\frac{\langle r_k^2 \rangle_{\text{Th}}}{\langle r_k^2 \rangle_0} = 2 \frac{\zeta(4)}{\zeta(3)} \frac{k_B T}{\hbar \omega_k},$$

with  $\zeta$  being the Riemann zeta function. Thus, since  $k_B T \gg \hbar \omega_k$ , the two fractions are clearly discernible. Furthermore, the ratio of the densities at the trap centre of the respective components is

$$\frac{n_{\text{Th}}(0)}{n_0(0)} = \zeta\left(\frac{3}{2}\right) \left(\frac{k_B T}{\hbar w_{\text{ho}}}\right)^{3/2},$$

so the contrast between the two fractions is high and this allows them to be clearly distinguished by measuring the atomic density in the trap.

However, the ideal approximation is far from appropriate for our system and thus, interactions need to be accounted for. As repulsive interactions come into play, the distribution of the condensed fraction becomes wider and the peak density decreases. This does not affect the thermal fraction as much since in this case the kinetic energy still dominates. The limit in which the interaction energy dominates the condensate dynamics and the kinetic energy can be neglected is the Thomas-Fermi regime. The extent to which this approximation is valid is determined by the Thomas-Fermi parameter

$$\frac{aN}{a_{\text{ho}}},$$

where  $a$  is the molecule-molecule scattering length.

In this experiment the Thomas-Fermi parameter is on the order of  $10^3$  therefore, it falls well within the Thomas-Fermi description. In this description the number density is given by

$$n_{\text{TF}}(\mathbf{r}) = \frac{1}{g} (\mu_{\text{TF}} - V(\mathbf{r})),$$

where  $g = \frac{4\pi\hbar^2 a}{m}$  is the coupling strength and the chemical potential  $\mu_{\text{TF}}$  is determined by a normalisation condition; it has the form

$$\mu_{\text{TF}} = \frac{\hbar\omega_{\text{ho}}}{2} \left(\frac{15Na}{a_{\text{ho}}}\right)^{2/5}.$$

For a harmonic potential, the density takes the form of an inverted parabola

$$n_{\text{TF}}(\mathbf{r}) = n_{\text{TF}}(0) \max \left( 1 - \frac{x^2}{R_x^2} - \frac{y^2}{R_y^2} - \frac{z^2}{R_z^2}, 0 \right), \quad (5.3)$$

with

$$R_k = a_{\text{ho}} \left( \frac{15Na}{a_{\text{ho}}} \right)^{1/5} \frac{\omega_{\text{ho}}}{\omega_k}$$

for  $k = x, y, z$ , and

$$n_{\text{TF}}(0) = \frac{1}{8\pi a_{\text{ho}}^2 a} \left( \frac{15Na}{a_{\text{ho}}} \right)^{2/5}.$$

The ratios of the sizes and densities of the two fractions can now be calculated for the interacting case and are both on the order of unity for our experimental parameters. This means that for a strongly interacting system, it is not easy to distinguish the condensed and thermal fractions with in-trap measurements. Taking advantage of the different expansion dynamics for the thermal and condensed part, time-of-flight images are generally used to study the system [94].

### 5.4.3 Expansion

In this subsection the expansion dynamics are discussed. First, the theory presented in [96, 97], that describes the expansion process is outlined. Then, when comparing with measurements of the release of the cloud from the trap we have observed interesting behaviour (shown in Figure 5.21), which is analysed in detail within this framework. It is partly caused by the strong interactions in the cloud and partly due to the residual magnetic trapping potential.

Upon release from the trap, the thermal part will undergo ballistic expansion and therefore, the size of the cloud in the direction  $k = x, y, z$ , denoted by  $\sigma_k(t)$ , will increase according to

$$\sigma_k(t)^2 = \sigma_k(0)^2 + \frac{k_B T}{m} t^2, \quad (5.4)$$

as was shown in Section 3.5.1. It is worth noting that the size grows at the same rate in all directions and for long times defined by  $\frac{k_B T}{m} t^2 \gg \sigma_k(0)^2$ , it attains a spherically symmetric distribution regardless of the shape of the trapping potential.

In contrast, for an anisotropic trapping potential, the expansion of the condensed part is also anisotropic. This occurs for both an ideal gas and a strongly

interacting one. In both cases an inversion of the aspect ratio is observed. However, it is for different reasons that this occurs.

The momentum distribution in the trap is the Fourier transform of the spatial wavefunction. For an ideal gas this distribution does not change during free fall and thus, the expansion dynamics are determined by this. The uncertainty relation dictates that where a particle's spatial wavefunction is tightly confined, the corresponding momentum wavefunction will have a large spread. Therefore, the gas will expand faster along the more tightly confined directions [64]. In comparison, for a condensate in the Thomas-Fermi regime, the anisotropic expansion is a result of the repulsion, both in-trap and during expansion [64].

In general, the dynamics of an interacting gas in a harmonic trap with time-dependent frequencies can be described with a classical model in which each particle experiences a force

$$\mathbf{F}(\mathbf{r}, t) = -\nabla (U(\mathbf{r}, t) + g\rho(\mathbf{r}, t)),$$

where  $\rho(\mathbf{r}, 0) = n_{\text{TF}}(\mathbf{r})$  as introduced in [96, 97]. In particular, the release from the trap corresponds to a sudden change in all the trap frequencies to zero. With this model, the distribution, which is originally an inverted parabola as in Equation 5.3, will continue to be an inverted parabola that is rescaled according to

$$R_k(t) = R_k b_k(t).$$

After applying this ansatz to Newton's second law, the scaling factors  $b_k(t)$  are found to behave according to [96]

$$\ddot{b}_k = \frac{\omega_k^2(0)}{b_k b_x b_y b_z} - \omega_k^2(t) b_k. \quad (5.5)$$

The initial conditions are  $b_k(0) = 1$  and  $\dot{b}_k(0) = 0$  since the cloud is initially at rest. The expansion is well described by this classical approach and does not depend of the interaction strength. The quantum mechanical aspect is relevant only in determining the initial density in the trap.

For an axially symmetric, elongated trap where the aspect ratio  $\lambda = \omega_z/\omega_{\perp} \ll 1$ ,

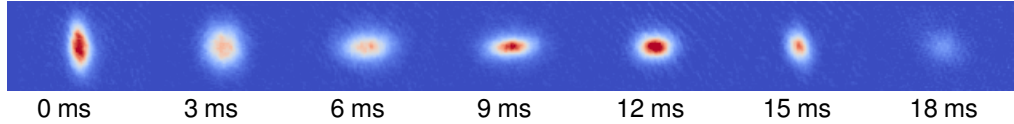


**Figure 5.21:** Atomic density after release from the optical dipole trap for different times of flight. Evaporation and expansion takes place in a magnetic field of 800 G. The final trap depth before release is  $U_0/k_B = 1.1 \mu\text{K}$ . Time of flight indicated under each image.

an analytic approximate solution of Equation 5.5 is available

$$\begin{aligned} b_{\perp}(\tau) &= \sqrt{1 + \tau^2} \\ b_z(\tau) &= 1 + \lambda^2 \left( \tau \arctan \tau - \ln \sqrt{1 + \tau^2} \right) \end{aligned}$$

with the dimensionless time  $\tau = \omega_{\perp} t$ . These results show that the gas expands rapidly in the directions of strong confinement while in the other direction the expansion is suppressed by a factor of  $\lambda^2$  [94].

In the Thomas-Fermi regime, the expansion of the condensate does not reflect the momentum distribution of the system in the trap since it changes during expansion due to the released interaction energy. However, the in-trap distribution can be determined through Bragg spectroscopy [98].

#### 5.4.4 Condensate Properties

Using the theory presented in the previous subsections as a framework, the experimental measurements resulting from releasing the atomic cloud, shown in Figure 5.21, are discussed. In this figure, a strongly interacting BEC is produced at 800 G and an oscillation in the aspect ratio of the cloud is observed after it is released. Regardless of the regime (thermal, ideal or Thomas-Fermi), upon release from the trap, the previously discussed theory predicts that the cloud size should increase in every direction albeit not necessarily at the same rate in contrast with what is observed.

To have a more quantitative description of the observed dynamics, a new measurement is carried out with an expansion at 700 G where the thermal and condensed fractions can be distinguished. Then, a bimodal Thomas-Fermi fit is calculated for each of the shots as described below. For the condensed part, the Thomas-Fermi distribution, presented in Equation 5.3, is used as a model. For comparison with the measured density profiles, these are integrated along each

axis and compared separately. The three-dimensional Thomas-Fermi distribution is twice integrated to obtain a one-dimensional distribution, resulting in

$$n_{\text{TF}}(x) = \max \left[ \frac{15N_0}{16R_x} \left( 1 - \frac{x^2}{R_x^2} \right)^2, 0 \right],$$

where  $N_0$  is the number of condensed molecules and  $R_x$  is the condensate size. The analysis of the thermal fraction is carried out approximating the distribution of the thermal fraction by a Gaussian distribution. The one-dimensional distribution is

$$n_{\text{Th}}(x) = \frac{N_{\text{Th}}}{\sqrt{2\pi}\sigma_x} \exp \left( -\frac{x^2}{2\sigma_x^2} \right).$$

Here,  $N_{\text{Th}}$  is the number of thermal molecules and  $\sigma_x$  determines the width of the distribution. The total density

$$n(x) = n_{\text{Th}}(x) + n_{\text{TF}}(x), \quad (5.6)$$

is fitted to the measured profile.

The resulting widths for the thermal and condensed fractions are plotted in Figure 5.22. Here, the sizes are shown as a function of time after extinguishing the light of the optical dipole trap. While in the  $x$  direction, expansion is observed as expected, it is striking that both the thermal and condensed fractions decrease in size in the  $y$  direction.

The explanation to this and to the observed oscillations in the aspect ratio, lie in the different contributions to the trapping potential. Recalling Figure 4.25, there is a magnetic contribution from the field that is used to control the interactions together with the contribution from the optical dipole trap. At the point where the BEC phase transition occurs, the magnetic contribution becomes comparable to that of the optical dipole trap. Moreover, this field is on during imaging and therefore, extinguishing the light of the optical dipole trap does not result in a free expansion of the atomic gas. Thus, care must be taken to analyse this behaviour.

Using Equation 5.5 the residual trap, that arises from the magnetic field, can be accounted for during the expansion. The plot shown in Figure 5.23 depicts the evolution of the cloud's size for the data shown in Figure 5.21 together with a numerical solution of Equation 5.5. For this figure, the overall size of the cloud is used, which includes both the thermal and condensed fractions. The numerical solution is calculated using the trap frequencies obtained in the

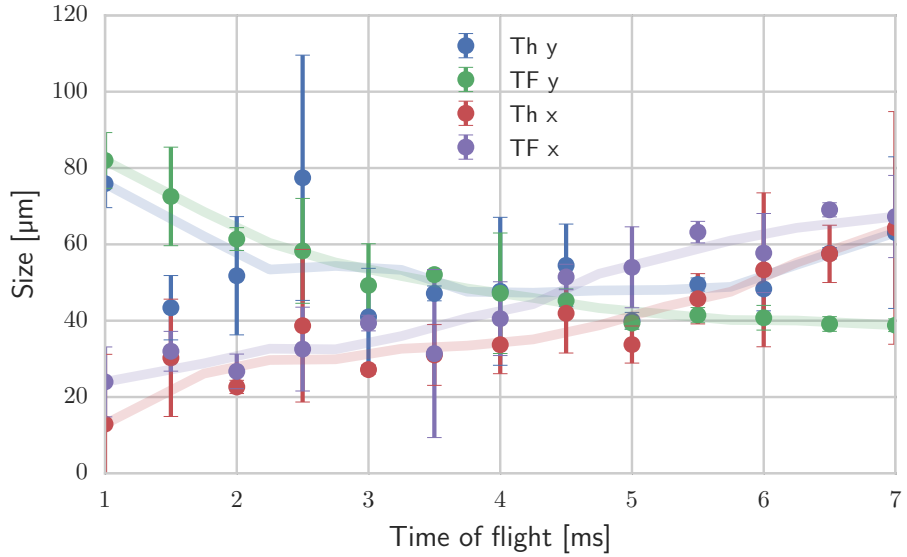


**Figure 5.22:** Release dynamics of thermal and condensed fractions after extinction of the dipole trap. For each shot, a bimodal fit is calculated from which the different widths are extracted. The sizes of the thermal (Th) and Thomas-Fermi (TF) fraction are reported separately as a function of time. A decrease in size is observed in the  $y$  direction which is not consistent with a free expansion. Error bars show the standard deviation calculated from three repetitions. The lines shown are a moving average shown as a guide to the eye.

analysis shown in Figure 4.25. The trap frequencies change from  $(\omega_x, \omega_y, \omega_z) = (867, 867, 245)\text{s}^{-1}$  to  $(220, i220, 220)\text{s}^{-1}$  (The  $i = \sqrt{-1}$  on the frequency indicates that the potential becomes anti-trapping in that direction since  $V(z) \propto \omega_{\text{vert}}^2$ ). This change corresponds to turning off the contribution of the light to the potential while leaving the magnetic contribution. With this model the positions of the maxima and minima are accurately reproduced. However, the amplitude of the oscillation does not match the predicted value. A reason for this may be that the model only accounts for the behaviour of the condensed fraction. It is expected that when including the thermal fraction in this analysis, the minima become less pronounced as it is seen in the measured data. This is because at the moment of release from the optical trap, the thermal atoms are moving in random directions and thus, the arrival times at the centre of the trap will not be the same for all of them. This spread on initial conditions will limit the minimum cloud size that can be obtained through these oscillations.

Whilst in the current setup the atomic cloud does not truly undergo free fall,

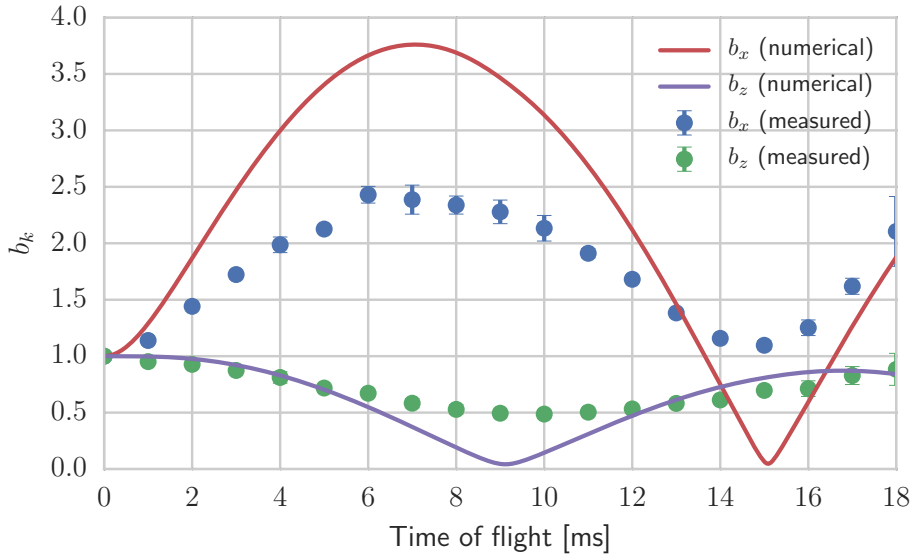


**Figure 5.23:** Dynamics of the atomic cloud after release from the optical dipole trap. The points mark the measured values in each direction. Solid lines are numerical solutions of Equation 5.5 without any free parameters. The data shown in this figure was obtained from the measurements shown in Figure 5.21

the expansion in the direction in which the trap frequency changes the most during release, can be used to estimate some of the parameters such as the temperature and condensate fraction. In this case, a free expansion may be assumed for short times (compared to the trapping frequencies).

In order to determine the condensed fraction of the density profiles shown in Figure 5.20, they are integrated along one direction resulting in the profiles shown in Figure 5.24 and fitted with the bi-modal Thomas-Fermi distribution given by Equation 5.6.

Figure 5.24 has been produced with the same data as the one used for Figure 5.20 and therefore shows the density after 5 ms of time of flight. Before and during the expansion, the magnetic field is set to 700 G, corresponding to a scattering length  $a \approx 1600a_0$ .

The temperature is estimated as described in Section 3.5.1 with the difference that only the thermal fraction's width is used in this calculation and also, only the short-time expansion of the tightly confined axis is considered. By doing this analysis, a semi-ideal approximation has been carried out in which the condensate and thermal fractions are assumed not to interact with each other. Furthermore, in this approximation, the condensate fraction is assumed to have contact self-

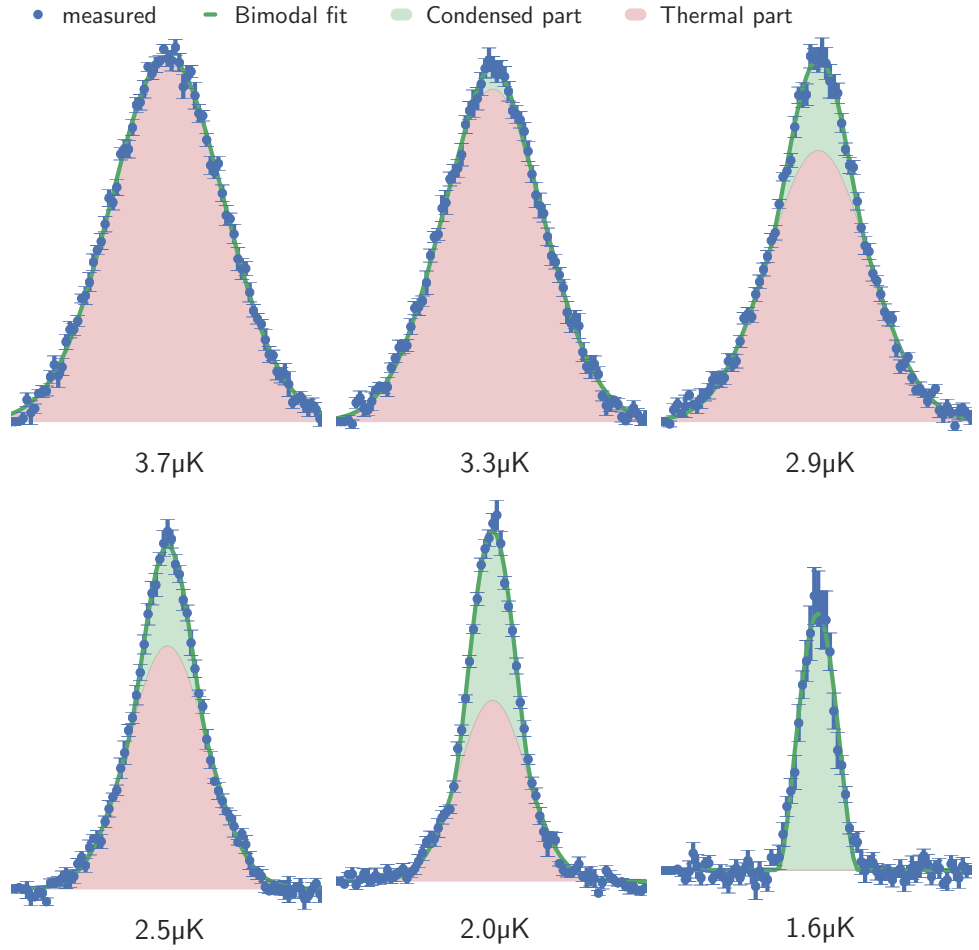


**Figure 5.24:** One-dimensional density profiles at various stages of evaporation. Condensate fraction increases as the depth of the dipole trap is decreased. Error bars on the data are statistical. A bimodal function comprised of a Gaussian and an inverted parabola is used to fit the data. The trap depth  $U_0/k_B$  at which each profile is measured is indicated under it.

interaction whilst the thermal part is non-interacting. In reality, this is not the case and there is interaction among all of the components. To accurately measure the temperature, interactions would need to be turned off suddenly, fast with respect to the trap frequencies, before releasing the atoms. Alternatively, using a Hartree-Fock model [99], interactions between the thermal and condensed fractions can be accounted for. With this tool, thermodynamical properties such as the temperature and chemical potential may be determined more accurately.

Estimated temperatures during the final stage of evaporation, corresponding to the profiles of Figure 5.24 are reported in Figure 5.25. Here, the temperature at each point is determined using two absorption images. One in-situ and a second

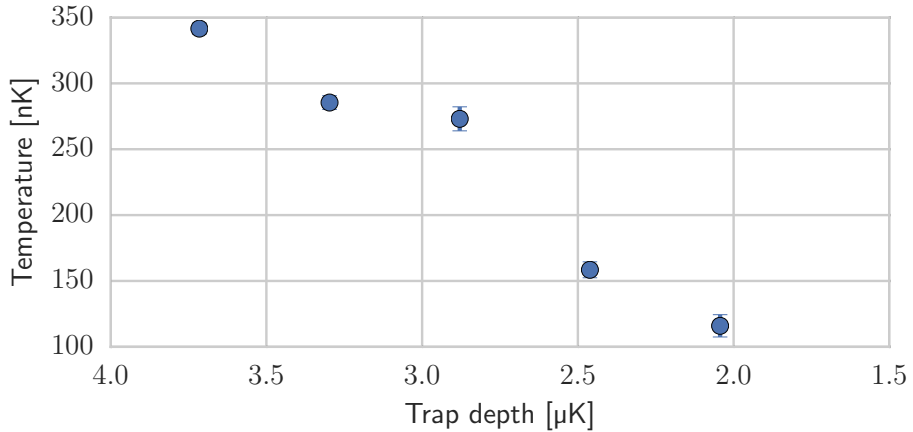


**Figure 5.25:** Temperature estimate during the final stages of evaporation.  
Error bars represent the standard deviation.

with a time-of-flight of 5 ms. The temperature is determined using the thermal width obtained from the bimodal fit and evaluated using Equation 5.4. Only where there is a sizeable thermal fraction it is possible to determine the temperature, which is why the pure condensate point has been excluded. Estimating the temperature assuming a free expansion of the cloud, whilst in reality there is a residual magnetic potential, results in an under-estimation of the temperature.

One of the parameters obtained from fitting the bimodal distribution is  $N_0$ : the number of condensed atoms. With this, the condensed fraction  $f_c$  can be readily calculated according to  $f_c = N_0/N_{\text{total}}$ , the result of which is shown in Figure 5.26. The total atom number  $N_{\text{total}}$  is the one presented in Figure 5.18 measured through absorption imaging.

With these measurements it is shown that an almost pure condensate with  $10^4$  molecules at a trap depth of 1.6  $\mu\text{K}$  was produced.

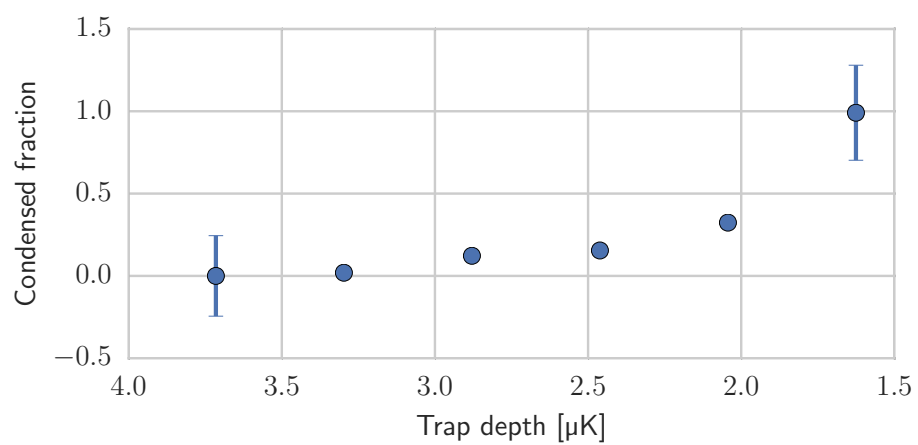


**Figure 5.26:** Condensed fraction at various stages of evaporation. Values are obtained from the bimodal fit of the data in Figure 5.24. Reported errors are derived from the fits and the statistical uncertainty associated to the total atom number. Each point has been measured 6 times.

## CHAPTER 6

# Conclusions and Outlook

A new versatile experimental apparatus capable of cooling both lithium-6 and caesium-133 has been established. With it, molecular Bose-Einstein condensates of lithium containing  $10^4$  molecules are now routinely produced and important steps towards producing quantum degenerate caesium gases have been made.

Several aspects involved in an experiment with ultracold atoms have been developed as part of the work for this thesis. The laser system, for example, is relevant at all stages of the experimental sequence as it is used for the Zeeman slower, as part of the magneto-optical trap (MOT), to produce the optical dipole trap and to perform absorption imaging of the atoms. Additionally, magnetic field generation is a requirement for implementing some of these techniques as well as for exploiting the wide tunability of the inter-atomic interactions present in a lithium-caesium system. Another aspect which was addressed in this work is the vacuum apparatus which, in spite of playing mostly a passive role, has implications on both the laser system, by limiting the optical access, and in the magnetic field generation, by imposing geometrical constraints. Furthermore, the influence of the stainless steel chamber on the magnetic fields was analysed. The orchestration of all the components in this experiment is carried out by a computer control system for which software to realise and execute experimental sequences was developed.

The experimental sequence begins by loading a MOT with atoms using a novel dual species Zeeman slower, the design of which was published [1]. Afterwards, the atoms are transferred to a far-of-resonance optical dipole trap in which the fundamental cooling limits encountered in the MOT can be overcome through evaporative cooling. This trap is produced by crossing two laser beams at the centre of the vacuum chamber. After this transfer, evaporative cooling was performed on lithium by decreasing the dipole trap's power and adjusting the

scattering length using magnetic Feshbach resonances. As evaporation progresses, the phase-space density increases and individual fermionic atoms bind to form bosonic Feshbach molecules which, when the phase-space density reaches a critical value, form a Bose-Einstein condensate (BEC). The resulting condensate has been analysed with respect to molecule number, condensate fraction, expansion dynamics and temperature.

A better characterisation of the produced molecular BEC is to be obtained in the near future by using a Hartree-Fock finite-temperature model. With this model, the temperature and chemical potential of the strongly interacting condensate may be determined with *in-situ* measurement of the density distribution [99].

Moreover, the constructed experimental system is also capable of cooling and trapping caesium. At present,  $2 \times 10^6$  atoms have been loaded into the dipole trap. An additional laser, which produces a trap that has a large volume, promises to increase this number and facilitate BEC formation for caesium in a dimple-trap configuration. After implementing evaporative cooling of caesium, an apparatus, capable of producing doubly degenerate gases, is within reach.

Whilst the techniques for lithium and caesium have been developed separately throughout this work, the system has been designed with the prospect of combining them in mind. Sequential loading of magneto-optical traps of each of them can already be carried out and it is a sensible technique to use for this mixture [69]. The equipment to control magnetic fields, necessary to combine both species in the dipole trap, is in place and the control system has the flexibility to readily add the required steps.

The molecular lithium BEC is a remarkable system. Changing the interaction strength between the atoms allows exploring the crossover between the Bose-Einstein condensate and degenerate Fermi gas regimes. A paradigmatic system in which to study this crossover is in a double well potential. In this, the scattering length is expected to have an effect on the tunnelling and self-trapping dynamics [100–103]. Effort to produce this double well potential and include it in the system is already under way.

Combining both species in the optical dipole trap will open the possibility to begin exploring impurity physics with a small admixture of caesium in a large ultracold lithium bath. The wide tunability of interactions between lithium and caesium allows uncovering a diverse set of phenomena. For instance, a gas with only inter-species (LiCs) interactions may be produced [28]. This is done by having a polarised sample of fermionic lithium-6 in which lithium-lithium s-wave

collisions are suppressed. Furthermore, lithium-caesium Feshbach resonances are close to a zero-crossing of the caesium-caesium scattering length so the intra-species interactions may be suppressed while the inter-species are enhanced. A system like this is well suited to realise and study the Fröhlich polaron Hamiltonian which describes the interactions between the electrons and ions in a solid [28].

Adding impurities to the double-well potential discussed before, the Dicke model can be realised [104, 105]. Within this framework, the wide tunability of interactions, would facilitate the exploration of a quantum phase transition present in this model [104].

Theoretical investigations of degenerate Bose-Fermi mixtures predict the disappearance of the Bose-Einstein condensate as the coupling between the bosons and fermions increases [106, 107]. However, in the intermediate coupling regime, boson-fermion interactions induce a boson-mediated fermion-fermion attraction which destroys the Fermi sea [106]. These phase transitions have not been observed yet and the tunability of the system presented in this thesis is an ideal candidate for their exploration.

# Bibliography

- [1] A. Paris-Mandoki, M. D. Jones, J. Nute, J. Wu, S. Warriar, and L. Hackermüller. “Versatile cold atom source for multi-species experiments.” *Rev. Sci. Instrum.* **85**, 113103, (2014).
- [2] V. Galitski and I. B. Spielman. “Spin-orbit coupling in quantum gases.” *Nature*. **494**, 49, (2013).
- [3] P. Gordon. “Numerical cognition without words: evidence from Amazonia.” *Science*. **306**, 496, (2004).
- [4] R. P. Feynman. “Simulating physics with computers”. *Int. J. Theor. Phys.* **21**, 467, (1982).
- [5] V. Boyer, R. Godun, G. Smirne, D. Cassettari, C. Chandrashekhar, A. Deb, Z. Laczik, and C. Foot. “Dynamic manipulation of Bose-Einstein condensates with a spatial light modulator”. *Phys. Rev. A*. **73**, 031402, (2006).
- [6] S. P. Rath, T. Yefsah, K. J. Günter, M. Cheneau, R. Desbuquois, M. Holzmann, W. Krauth, and J. Dalibard. “Equilibrium state of a trapped two-dimensional Bose gas”. *Phys. Rev. A*. **82**, 013609, (2010).
- [7] Y. Colombe, E. Knyazchyan, O. Morizot, B. Mercier, V. Lorent, and H. Perrin. “Ultracold atoms confined in rf-induced two-dimensional trapping potentials”. *Europhys. Lett.* **67**, 593, (2004).
- [8] R. Folman, P. Krüger, J. Schmiedmayer, J. Denschlag, and C. Henkel. “Microscopic atom optics: From wires to an atom chip”. *Adv. At. Mol. Opt. Phys.* **48**, 263, (2002).
- [9] S. Hofferberth, I. Lesanovsky, B. Fischer, J. Verdu, and J. Schmiedmayer. “Radiofrequency-dressed-state potentials for neutral atoms”. *Nature Physics*. **2**, 710, (2006).

- [10] U. Schneider, L. Hackermüller, J. P. Ronzheimer, S. Will, S. Braun, T. Best, I. Bloch, E. Demler, S. Mandt, D. Rasch, and A. Rosch. “Fermionic transport and out-of-equilibrium dynamics in a homogeneous Hubbard model with ultracold atoms”. *Nature Physics.* **8**, 213, (2012).
- [11] M. Greiner, O. Mandel, T. Esslinger, T. W. Hänsch, and I. Bloch. “Quantum phase transition from a superfluid to a Mott insulator in a gas of ultracold atoms.” *Nature.* **415**, 39, (2002).
- [12] Y.-J. Lin, R. L. Compton, K. Jiménez-García, J. V. Porto, and I. B. Spielman. “Synthetic magnetic fields for ultracold neutral atoms.” *Nature.* **462**, 628, (2009).
- [13] M. Aidelsburger, M. Atala, S. Nascimbène, S. Trotzky, Y.-A. Chen, and I. Bloch. “Experimental Realization of Strong Effective Magnetic Fields in an Optical Lattice”. *Phys. Rev. Lett.* **107**, 255301, (2011).
- [14] J. F. Sherson, C. Weitenberg, M. Endres, M. Cheneau, I. Bloch, and S. Kuhr. “Single-atom-resolved fluorescence imaging of an atomic Mott insulator.” *Nature.* **467**, 68, (2010).
- [15] W. S. Bakr, J. I. Gillen, A. Peng, S. Fölling, and M. Greiner. “A quantum gas microscope for detecting single atoms in a Hubbard-regime optical lattice.” *Nature.* **462**, 74, (2009).
- [16] M. H. Anderson, J. R. Ensher, M. R. Matthews, C. E. Wieman, and E. A. Cornell. “Observation of bose-einstein condensation in a dilute atomic vapor.” *Science.* **269**, 198, (1995).
- [17] K. Davis, M. Mewes, M. Andrews, N. van Druten, D. Durfee, D. Kurn, and W. Ketterle. “Bose-Einstein Condensation in a Gas of Sodium Atoms”. *Phys. Rev. Lett.* **75**, 3969, (1995).
- [18] B. DeMarco. “Onset of Fermi Degeneracy in a Trapped Atomic Gas”. *Science.* **285**, 1703, (1999).
- [19] M. Greiner, C. A. Regal, and D. S. Jin. “Emergence of a molecular Bose-Einstein condensate from a Fermi gas.” *Nature.* **426**, 537, (2003).
- [20] M. Zwierlein, C. Stan, C. Schunck, S. Raupach, S. Gupta, Z. Hadzibabic, and W. Ketterle. “Observation of Bose-Einstein Condensation of Molecules”. *Phys. Rev. Lett.* **91**, 250401, (2003).

- [21] S. Jochim, M. Bartenstein, A. Altmeyer, G. Hendl, S. Riedl, C. Chin, J. Hecker Denschlag, and R. Grimm. “Bose-Einstein condensation of molecules.” *Science*. **302**, 2101, (2003).
- [22] M. W. Zwierlein, J. R. Abo-Shaeer, A. Schirotzek, C. H. Schunck, and W. Ketterle. “Vortices and superfluidity in a strongly interacting Fermi gas.” *Nature*. **435**, 1047, (2005).
- [23] J. Struck, C. Ölschläger, R. Le Targat, P. Soltan-Panahi, A. Eckardt, M. Lewenstein, P. Windpassinger, and K. Sengstock. “Quantum simulation of frustrated classical magnetism in triangular optical lattices.” *Science*. **333**, 996, (2011).
- [24] J. Simon, W. S. Bakr, R. Ma, M. E. Tai, P. M. Preiss, and M. Greiner. “Quantum simulation of antiferromagnetic spin chains in an optical lattice.” *Nature*. **472**, 307, (2011).
- [25] Y.-J. Lin, K. Jiménez-García, and I. B. Spielman. “Spin-orbit-coupled Bose-Einstein condensates.” *Nature*. **471**, 83, (2011).
- [26] G. Zürn, T. Lompe, A. N. Wenz, S. Jochim, P. S. Julienne, and J. M. Hutson. “Precise characterization of Li<sub>6</sub> Feshbach resonances using trap-sideband-resolved RF spectroscopy of weakly bound molecules”. *Phys. Rev. Lett.* **110**, 135301, (2013).
- [27] M. Berninger, A. Zenesini, B. Huang, W. Harm, H.-C. Nägerl, F. Ferlaino, R. Grimm, P. Julienne, and J. Hutson. “Feshbach resonances, weakly bound molecular states, and coupled-channel potentials for cesium at high magnetic fields”. *Phys. Rev. A*. **87**, 032517, (2013).
- [28] M. Repp, R. Pires, J. Ulmanis, R. Heck, E. D. Kuhnle, M. Weidemüller, and E. Tiemann. “Observation of interspecies <sup>6</sup>Li-<sup>133</sup>Cs Feshbach resonances”. *Phys. Rev. A*. **87**, 010701, (2013).
- [29] S.-K. Tung, C. Parker, J. Johansen, C. Chin, Y. Wang, and P. S. Julienne. “Ultracold mixtures of atomic <sup>6</sup>Li and <sup>133</sup>Cs with tunable interactions”. *Phys. Rev. A*. **87**, 010702, (2013).
- [30] J. Deiglmayr, A. Grochola, M. Repp, O. Dulieu, R. Wester, and M. Weidemüller. “Permanent dipole moment of LiCs in the ground state”. *Phys. Rev. A*. **82**, 032503, (2010).

- [31] F. Grusdt, Y. E. Shchadilova, a. N. Rubtsov, and E. Demler. “Renormalization group approach to the Fröhlich polaron model: application to impurity-BEC problem”. [arXiv: 1410.2203](https://arxiv.org/abs/1410.2203).
- [32] V. Efimov. “Energy levels arising from resonant two-body forces in a three-body system”. *Phys. Lett. B.* 33, 563, (1970).
- [33] R. Pires, J. Ulmanis, S. Häfner, M. Repp, A. Arias, E. D. Kuhnle, and M. Weidemüller. “Observation of Efimov Resonances in a Mixture with Extreme Mass Imbalance”. *Phys. Rev. Lett.* 112, 250404, (2014).
- [34] S.-K. Tung, K. Jiménez-García, J. Johansen, C. V. Parker, and C. Chin. “Geometric Scaling of Efimov States in a Li<sub>6</sub>-Cs<sub>133</sub> Mixture”. *Phys. Rev. Lett.* 113, 240402, (2014).
- [35] D. DeMille. “Quantum Computation with Trapped Polar Molecules”. *Phys. Rev. Lett.* 88, 067901, (2002).
- [36] S. Warriar. “Towards an Ultracold Bose-Fermi Mixture of Cesium and Lithium Atoms”. PhD thesis. University of Nottingham, 2013.
- [37] M. D. Jones. “Preparation of Cold Samples of Caesium-133 and Lithium-6 in a Single Apparatus for Bose-Fermi Mixture Experiments”. PhD thesis. University of Nottingham, 2014.
- [38] D. Wineland, R. Drullinger, and F. Walls. “Radiation-Pressure Cooling of Bound Resonant Absorbers”. *Phys. Rev. Lett.* 40, 1639, (1978).
- [39] W. Phillips and H. Metcalf. “Laser Deceleration of an Atomic Beam”. *Phys. Rev. Lett.* 48, 596, (1982).
- [40] P. Lett, R. Watts, C. Westbrook, W. Phillips, P. Gould, and H. Metcalf. “Observation of Atoms Laser Cooled below the Doppler Limit”. *Phys. Rev. Lett.* 61, 169, (1988).
- [41] C. Cohen-Tannoudji, B. Diu, and F. Laloe. *Quantum Mechanics*. Quantum Mechanics Volumes 1 and 2. Paris: Wiley, 1992.
- [42] M. E. Gehm. *Properties of <sup>6</sup>Li*. URL: <http://www.physics.ncsu.edu/jet/techdocs/pdf/PropertiesOfLi.pdf>.
- [43] D. A. Steck. *Cesium D Line Data*. URL: <http://steck.us/alkalidata>.
- [44] D. A. Steck. *Quantum and Atom Optics*. URL: <http://steck.us/teaching>.

- [45] C. J. Foot. *Atomic Physics*. 1st. New York: Oxford University Press, 2005.
- [46] A. Paris-Mandoki. “Colisiones ultrafrías polarizadas”. Bachelor’s thesis. Universidad Nacional Autónoma de México, 2010.
- [47] A. Derevianko, J. Babb, and A. Dalgarno. “High-precision calculations of van der Waals coefficients for heteronuclear alkali-metal dimers”. *Phys. Rev. A.* **63**, 052704, (2001).
- [48] C. Chin. “A simple model of Feshbach molecules”. [arXiv: 0506313 \(cond-mat\)](https://arxiv.org/abs/0506313).
- [49] C. Chin, P. Julienne, and E. Tiesinga. “Feshbach resonances in ultracold gases”. *Rev. Mod. Phys.* **82**, 1225, (2010).
- [50] W. Ketterle and M. Zwierlein. “Making, probing and understanding ultracold Fermi gases”. *206*, (2008).
- [51] T. Walker, D. Sesko, and C. Wieman. “Collective behavior of optically trapped neutral atoms”. *Phys. Rev. Lett.* **64**, 408, (1990).
- [52] K. Davis, M.-O. Mewes, M. Joffe, M. Andrews, and W. Ketterle. “Evaporative Cooling of Sodium Atoms”. *Phys. Rev. Lett.* **74**, 5202, (1995).
- [53] W. Petrich, M. Anderson, J. Ensher, and E. Cornell. “Stable, Tightly Confining Magnetic Trap for Evaporative Cooling of Neutral Atoms”. *Phys. Rev. Lett.* **74**, 3352, (1995).
- [54] E. Raab, M. Prentiss, A. Cable, S. Chu, and D. Pritchard. “Trapping of Neutral Sodium Atoms with Radiation Pressure”. *Phys. Rev. Lett.* **59**, 2631, (1987).
- [55] H. J. Metcalf and P. V. der Straten. *Laser cooling and trapping*. New York: Springer, 1999.
- [56] J. Dalibard and C. Cohen-Tannoudji. “Laser cooling below the Doppler limit by polarization gradients: simple theoretical models”. *Journal of the Optical Society of America B.* **6**, 2023, (1989).
- [57] A. Piccardo-Selg. “Degenerate Quantum Gases: Towards Bose-Einstein Condensation of Sodium”. Diploma Thesis. University of Heidelberg, 2008.
- [58] C. Fort, A. Bambini, L. Cacciapuoti, F. Cataliotti, M. Prevedelli, G. Tino, and M. Inguscio. “Cooling mechanisms in potassium magneto-optical traps”. *Eur. Phys. J. D.* **3**, 113, (1998).

- [59] S. Stellmer, B. Pasquiou, R. Grimm, and F. Schreck. “Laser Cooling to Quantum Degeneracy”. *Phys. Rev. Lett.* **110**, 263003, (2013).
- [60] O. Luiten, M. Reynolds, and J. Walraven. “Kinetic theory of the evaporative cooling of a trapped gas”. *Phys. Rev. A.* **53**, 381, (1996).
- [61] S. Chaudhuri, S. Roy, and C. S. Unnikrishnan. “Evaporative Cooling of Atoms to Quantum Degeneracy in an Optical Dipole Trap”. *J. Phys. Conf. Ser.* **80**, 012036, (2007).
- [62] K. O’Hara, M. Gehm, S. Granade, and J. Thomas. “Scaling laws for evaporative cooling in time-dependent optical traps”. *Phys. Rev. A.* **64**, 051403, (2001).
- [63] L. Luo, B. Clancy, J. Joseph, J. Kinast, A. Turlapov, and J. E. Thomas. “Evaporative cooling of unitary Fermi gas mixtures in optical traps”. *New J. Phys.* **8**, 213, (2006).
- [64] W. Ketterle, D. S. Durfee, and D. M. Stamper-Kurn. “Making, probing and understanding Bose-Einstein condensates”. [arXiv: 9904034 \(cond-mat\)](https://arxiv.org/abs/9904034).
- [65] M. R. Andrews, M.-O. Mewes, N. J. van Druten, D. S. Durfee, D. M. Kurn, and W. Ketterle. “Direct, Nondestructive Observation of a Bose Condensate”. *Science*. **273**, 84, (1996).
- [66] H. Loh, Y.-J. Lin, I. Teper, M. Cetina, J. Simon, J. K. Thompson, and V. Vuletić. “Influence of grating parameters on the linewidths of external-cavity diode lasers”. *Appl. Opt.* **45**, 9191, (2006).
- [67] U. Schünemann, H. Engler, R. Grimm, M. Weidemüller, and M. Zielonkowski. “Simple scheme for tunable frequency offset locking of two lasers”. *Review of Scientific Instruments*. **70**, 242, (1999).
- [68] S. Bali, K. O’Hara, M. Gehm, S. Granade, and J. Thomas. “Quantum-diffractive background gas collisions in atom-trap heating and loss”. *Phys. Rev. A.* **60**, R29, (1999).
- [69] U. Schlöder, H. Engler, U. Schünemann, R. Grimm, and M. Weidemüller. “Cold inelastic collisions between lithium and cesium in a two-species magneto-optical trap”. *Eur. Phys. J. D.* **7**, 331, (1999).
- [70] P. della Porta, C. Emili, and S. J. Hellier. *Alkali Metal Generation and Gas Evolution from Alkali Metal Dispensers*. Tech. rep. 1968.

- [71] M. Safranova, B. Arora, and C. Clark. “Frequency-dependent polarizabilities of alkali-metal atoms from ultraviolet through infrared spectral regions”. *Phys. Rev. A.* **73**, 022505, (2006).
- [72] D. Stamper-Kurn, H.-J. Miesner, A. Chikkatur, S. Inouye, J. Stenger, and W. Ketterle. “Reversible Formation of a Bose-Einstein Condensate”. *Phys. Rev. Lett.* **81**, 2194, (1998).
- [73] R. Heck. “All-Optical Formation of an Ultracold Gas of Fermionic Lithium Close to Quantum Degeneracy”. PhD thesis. University of Heidelberg, 2012.
- [74] S. Hamann, D. Haycock, G. Klose, P. Pax, I. Deutsch, and P. Jessen. “Resolved-Sideband Raman Cooling to the Ground State of an Optical Lattice”. *Phys. Rev. Lett.* **80**, 4149, (1998).
- [75] M. Kasevich and S. Chu. “Laser cooling below a photon recoil with three-level atoms”. *Phys. Rev. Lett.* **69**, 1741, (1992).
- [76] A. Kerman, V. Vuletić, C. Chin, and S. Chu. “Beyond Optical Molasses: 3D Raman Sideband Cooling of Atomic Cesium to High Phase-Space Density”. *Phys. Rev. Lett.* **84**, 439, (2000).
- [77] V. Vuletić, C. Chin, A. Kerman, and S. Chu. “Degenerate Raman Sideband Cooling of Trapped Cesium Atoms at Very High Atomic Densities”. *Phys. Rev. Lett.* **81**, 5768, (1998).
- [78] P. M. Duarte, R. a. Hart, J. M. Hitchcock, T. a. Corcovilos, T.-L. Yang, A. Reed, and R. G. Hulet. “All-optical production of a lithium quantum gas using narrow-line laser cooling”. *Phys. Rev. A.* **84**, 061406, (2011).
- [79] A. Burchianti, G. Valtolina, J. a. Seman, E. Pace, M. De Pas, M. Inguscio, M. Zaccanti, and G. Roati. “Efficient all-optical production of large Li<sub>6</sub> quantum gases using D1 gray-molasses cooling”. *Phys. Rev. A.* **90**, 043408, (2014).
- [80] A. T. Grier, I. Ferrier-Barbut, B. S. Rem, M. Delehaye, L. Khaykovich, F. Chevy, and C. Salomon. “Λ-enhanced sub-Doppler cooling of lithium atoms in D<sub>1</sub> gray molasses”. *Phys. Rev. A.* **87**, 063411, (2013).
- [81] F. Sievers, S. Wu, N. Kretzschmar, D. R. Fernandes, D. Suchet, M. Rabinovic, C. V. Parker, L. Khaykovich, C. Salomon, and F. Chevy. “Simultaneous sub-Doppler laser cooling of fermionic <sup>6</sup>Li and <sup>40</sup>K on the D<sub>1</sub> line: Theory and Experiment”. [arXiv: 1410.8545](https://arxiv.org/abs/1410.8545).

- [82] R. Grimm, M. Weidemüller, and Y. B. Ovchinnikov. “Optical dipole traps for neutral atoms”. [arXiv: 9902072 \(physics\)](https://arxiv.org/abs/9902072).
- [83] G. L. Gattobigio, T. Pohl, G. Labeyrie, and R. Kaiser. “Scaling laws for large magneto-optical traps”. *Physica Scripta*. 81, 025301, (2010).
- [84] S. J. M. Kuppens, K. L. Corwin, K. W. Miller, T. E. Chupp, and C. E. Wieman. “Loading an optical dipole trap”. *Phys. Rev. A*. 62, 1, (2000).
- [85] J. Söding, D. Guéry-Odelin, P. Desbiolles, G. Ferrari, and J. Dalibard. “Giant Spin Relaxation of an Ultracold Cesium Gas”. *Phys. Rev. Lett.* 80, 1869, (1998).
- [86] D. Guéry-Odelin, J. Söding, P. Desbiolles, and J. Dalibard. “Is Bose-Einstein condensation of atomic cesium possible?” *Europhys. Lett.* 44, 25, (1998).
- [87] D. S. Petrov, C. Salomon, and G. V. Shlyapnikov. “Weakly Bound Dimers of Fermionic Atoms”. *Phys. Rev. Lett.* 93, 090404, (2004).
- [88] S. Jochim, M. Bartenstein, G. Hendl, J. H. Denschlag, R. Grimm, A. Mosk, and M. Weidemüller. “Magnetic field control of elastic scattering in a cold gas of fermionic lithium atoms”. *Phys. Rev. Lett.* 89, 273202, (2002).
- [89] T. Weber, J. Herbig, M. Mark, H.-C. Nägerl, and R. Grimm. “Three-Body Recombination at Large Scattering Lengths in an Ultracold Atomic Gas”. *Phys. Rev. Lett.* 91, 123201, (2003).
- [90] C.-L. Hung, X. Zhang, N. Gemelke, and C. Chin. “Accelerating evaporative cooling of atoms into Bose-Einstein condensation in optical traps”. *Phys. Rev. A*. 78, 1, (2008).
- [91] T. Köhler, K. Góral, and P. Julienne. “Production of cold molecules via magnetically tunable Feshbach resonances”. *Rev. Mod. Phys.* 78, 1311, (2006).
- [92] C. Chin and R. Grimm. “Thermal equilibrium and efficient evaporation of an ultracold atom-molecule mixture”. *Phys. Rev. A*. 69, 033612, (2004).
- [93] S. Jochim. “Bose-Einstein condensation of molecules.” PhD thesis. Leopold-Franzens-Universität Innsbruck, 2004.
- [94] L. Pitaevskii and S. Stringari. *Bose-Einstein Condensation*. International Series of Monographs on Physics. Oxford: Clarendon Press, 2003.

- [95] M. Abramowitz and I. A. Stegun. *Handbook of Mathematical Functions with Formulas, Graphs, and Mathematical Tables*. 9th. New York: Dover, 1964.
- [96] Y. Castin and R. Dum. “Bose-Einstein Condensates in Time Dependent Traps”. *Phys. Rev. Lett.* **77**, 5315, (1996).
- [97] Y. Kagan, E. Surkov, and G. Shlyapnikov. “Evolution of a Bose-condensed gas under variations of the confining potential”. *Phys. Rev. A.* **54**, R1753, (1996).
- [98] J. Stenger, S. Inouye, A. Chikkatur, D. Stamper-Kurn, D. Pritchard, and W. Ketterle. “Bragg Spectroscopy of a Bose-Einstein Condensate”. *Phys. Rev. Lett.* **82**, 4569, (1999).
- [99] N. Welch. “Non-Equilibrium Dynamics of Bose-Einstein Condensates”. PhD thesis. University of Nottingham, 2015.
- [100] P. Zou and F. Dalfovo. “Josephson oscillations and self-trapping of superfluid fermions in a double-well potential”. [arXiv: 1401.2007](https://arxiv.org/abs/1401.2007).
- [101] A. Spuntarelli, P. Pieri, and G. Strinati. “Josephson Effect throughout the BCS-BEC Crossover”. *Phys. Rev. Lett.* **99**, 040401, (2007).
- [102] L. Salasnich, N. Manini, and F. Toigo. “Macroscopic periodic tunneling of Fermi atoms in the BCS-BEC crossover”. *Phys. Rev. A.* **77**, 043609, (2008).
- [103] S. K. Adhikari, H. Lu, and H. Pu. “Self-trapping of a Fermi super-fluid in a double-well potential in the BEC-unitarity crossover”. [arXiv: 0911.0815](https://arxiv.org/abs/0911.0815).
- [104] J. Mumford, J. Larson, and D. H. J. O’Dell. “Impurity in a bosonic Josephson junction: Swallowtail loops, chaos, self-trapping, and Dicke model”. *Phys. Rev. A.* **89**, 023620, (2014).
- [105] J. Mumford and D. H. J. O’Dell. “Critical exponents for an impurity in a bosonic Josephson junction: Position measurement as a phase transition”. *Phys. Rev. A.* **90**, 063617, (2014).
- [106] E. N. Duchon. “Quantum Phase Transitions in the Bose Hubbard Model and in a Bose-Fermi Mixture”. PhD thesis. The Ohio State University, 2013.

- [107] E. Fratini and P. Pieri. “Pairing and condensation in a resonant Bose-Fermi mixture”. *Physical Review A - Atomic, Molecular, and Optical Physics.* 81, (2010).